9-20-2013 12:00 AM

Fabricating Cost-Effective Nanostructures for Biomedical Applications

Erden Ertorer
The University of Western Ontario

Supervisor
Silvia Mittler
The University of Western Ontario

Graduate Program in Biomedical Engineering
A thesis submitted in partial fulfillment of the requirements for the degree in Doctor of Philosophy
© Erden Ertorer 2013

Fabricating Cost-Effective Nanostructures for Biomedical Applications

(Thesis format: Integrated Article)

by

Erden <u>Ertorer</u>

Graduate Program in Biomedical Engineering

A thesis submitted in partial fulfillment
of the requirements for the degree of
Doctor of Philosophy

The School of Graduate and Postdoctoral Studies
The University of Western Ontario
London, Ontario, Canada

© Erden Ertorer 2013

Abstract

In this thesis we described inexpensive alternatives to fabricate nanostructures on planar substrates and provided example applications to discuss the efficiency of fabricated nanostructures.

The first method we described is forming large area systematically changing multi-shape nanoscale structures on a chip by laser interference lithography. We analyzed the fabricated structures at different substrate positions with respect to exposure time, exposure angle and associated light intensity profile. We presented experimental details related to the fabrication of symmetric and biaxial periodic nanostructures on photoresist, silicon surfaces, and ion-milled glass substrates. Behavior of osteoblasts and osteoclasts on the nanostructures was investigated. These results suggest that laser interference lithography is an easy and inexpensive method to fabricate systematically changing nanostructures for cell adhesion studies. We also used laser interference lithography to fabricate plasmonic structures. Fabrication details of gold nanodisk arrays were described. Experimental and simulation results show that those structures are suitable to develop highly sensitive plasmonic sensors.

As a second fabrication method we described the growth of surface immobilized gold nanoparticles with organometallic chemical vapor deposition (OMCVD) on amine terminated surfaces. Samples fabricated using different deposition times were characterized by UV-Vis spectroscopy and scanning electron microscopy. Particle stability on the samples was tested by washing and rinsing treatments with various organic solvents. The size, interparticle distance, and shape of the gold nanoparticles demonstrated that OMCVD is a simple, economical, and fast way to fabricate surface-bonded and stable gold nanoparticles. The plasmonic properties, the stability of the particles and the biotin-streptavidin test showed that these OMCVD-grown gold nanoparticles are suitable for reproducible, low noise and highly sensitive biosensing applications.

We further investigated the similar-to-real-life biosensing capabilities of the OMCVD-grown nanoparticles. Conventional antibody immobilization methods using biotin-streptavidin affinity, introduces additional chemistry and distance between the surface and the recognition

sites and decreases the sensitivity. With the new recognition chemistry, epidermal growth factor receptor (EGFR) antibody recognition sites were directly immobilized on AuNP surfaces to decrease the distance between the sensor surface and the recognition sites for detecting EGFR antigens. In comparison with the literature, we obtained increased signal response with further optimization possibilities.

Keywords

Nanotechnology, biosensors, biosensing, cell adhesion, surface topography, periodic nanostructures, laser interference lithography, adhesion and spreading of cells, osteoblasts, osteoclasts, gold nanoparticles, organometallic chemical vapor deposition, surface functionalization, CVD.

Co-Authorship Statement

This thesis contains materials from previously published manuscripts and manuscripts under preparation co-authored by Fartash Vasefi, Joel Keshwah, Mohamadreza Najiminaini, Christopher Halfpap, Uwe Langbein, Jeffrey J. L. Carson, Douglas W. Hamilton, Silvia Mittler, Jessica C. Avery, Laura C. Pavelka, Rasoul Soleimani, Benjamin Wheal, Stephen Sims, Shell Ip, Hao Jiang, and Gilbert Walker. Erden Ertorer conducted most of the experimental work, fabrication, characterization, simulation and data analysis.

In Chapter 2, Erden Ertorer performed fabrication, characterization and simulation of the structures. Fartash Vasefi and Mohamadreza Najiminaini assisted with fabrication and imaging processes of nanostructures made on glass and silicon. Christopher Halfpap performed the ion milling of the structures to the fused silica substrate. Joel Keshwah and Douglas W. Hamilton conducted osteoblast studies. Osteoclast studies were performed by Benjamin Wheal.

In Chapter 3, Erden Ertorer performed, fabrication, characterization, simulation of the structures and data analysis. Mohamadreza Najiminaini and Hao Jiang assisted with the numerical simulations and evaluation of the results.

In Chapter 4, Erden Ertorer performed, process optimization, fabrication, characterization and data analysis of OMCVD grown gold nanoparticles. The precursor for fabricating the gold nanoparticles with organometallic chemical vapor deposition was prepared by Jessica C. Avery and Laura C. Pavelka.

In Chapter 5, Erden Ertorer proposed the idea of plasmonic sensing with antibody fragments, fabricated the samples and conducted the biosensing experiments with Shell IP. Optimization of the process of antibody fragment synthesis was conducted by Shell Ip. Precursor for fabricating the gold nanoparticles was synthesized by Rasoul Soleimani.

Dedication

This work is dedicated to my parents, who have always supported my "projects" since childhood. It is also dedicated to Sabahattin Koca, who was my role model and contributed to my education in many ways; and to my son Arda Deniz Ertorer, whose existence makes the world a better place.

Acknowledgments

This thesis would not have been possible without the support of many people; I was very fortunate to have had each of them in my life. First of all, I would like to thank Silvia Mittler for her support, encouragement, mentorship, and guidance during my studies.

I want to thank the Biomedical Engineering program, especially Diana Timmermans. She has always stood by me, even before my admission, and she is one of the reasons I chose Biomedical Engineering. Dr. Hesham El Naggar always encouraged me to pursue my studies at the PhD level. His support and guidance were extremely valuable for me.

I would like to thank the Department of Physics and Astronomy for hosting me for years. Brian Dalrymple and Frank Van Sas in Machine Shop always came up with better designs than I could – better even than I could imagine. I also learned a lot from Doug Hie, and not only technical things. I entered into the "nano world" with the guidance of Rick Glew, Tim Goldhawk and Todd Simpson.

My advisory committee members, Lyudmila Goncharova, Mark S. Workentin and Douglas W. Hamilton, were always helpful and available to me despite their busy schedules. I greatly appreciate their support and guidance.

Our collaborators Uwe Langbein, Jeff Carson, and Stephen Sims provided me the opportunity to learn about different labs, techniques and approaches.

Jian Liu, Shailesh Nene, Santino Barbagiovanni, Arash Akbari and Sergei Dedyulin: I am thankful for your invaluable friendship.

and Ramazan Aras, for offering enormous moral support throughout my degree. Thanks to my good friends Irene Sperandio, Damiano Vendramini, and Anna Sedda for providing me intellectual and moral support whenever needed. I am lucky to have known all of you.

I am very fortunate to have a wonderful family who supports me in various stages of my studies. My father Sayim Ertorer, my mother Nazik Ertorer, my sister Aysen Ertorer Kir, her husband Erkan Kir and my niece Berfin Kir have always encouraged me to keep heading for the light at the end of the tunnel, even though that path took me far, far away from them. Thank you all for enduring this process with me. And finally, I could never have completed this dissertation without the continued, unconditional support of my wife Secil Erdogan. She has been my source of strength and motivation. She stood by my side with unlimited love, patience, and understanding.

Table of Contents

x

xi

List of Figures

xv

xvi

xvii

List of Appendices

List of Abbreviations

AuNP	Gold nanoparticle
CVD	Chemical vapor deposition
EBL	Electron beam lithography
EBL	Electron beam lithography
LIL	Laser interference lithography
EGFR	Epidermal growth factor receptor
Fab	Fragment antigen binding
Fc	Fragment crystallizable
FDTD	Finite difference time domain
FIB	Focused ion beam
HMDS	Hexamethyldisilazane
LSPR	Localized surface plasmon resonance
OMCVD	Organometallic Chemical Vapor Deposition
PBS	Phosphate buffered saline
RCO	Rat calvarial osteoblasts
RIU	Refractive index unit
SAM	Self assembled monolayer
SEM	Scanning electron microscope
SERS	Surface enhance Raman spectroscopy
SPR	Surface plasmon resonance
UV-Vis	Ultraviolet - Visible

Chapter 1

1.1   Introduction

With improvements in technology, we are at the age of manipulating matter at the molecular and atomic scales. As a result of these developments, a new branch of science emerged several decades ago called nanotechnology. Properties of matter differ from those of its bulk form at the nanoscale. Understanding, manipulating and using these properties requires an interdisciplinary research effort involving physics, chemistry, biology, surface science electronics and mechanical engineering.

The majority of the vital events of living organisms happen at the molecular level; therefore, nanotechnology provides us tools to interact with living systems. Biomedical research has been taking advantage of nanotechnology in many different subfields, such as drug delivery, tissue engineering, imaging, biomaterials, biosensors, etc. [1]–[8]

Interaction between nanostructures and living organisms are not only limited by molecular level chemical interactions, but it is also known that cells and tissues respond to the morphology of nanostructures. [4][5][9][10] In this field, there is a need for new fabrication methods to create nanostructures over larger areas. [11] Understanding cell and tissue nanoscale interactions increases our fundamental knowledge of cell biology, such as preferential adhesion, migration, and proliferation rate, and provides new opportunities for tissue engineering and implant technology. [3]–[5][9][12]–[14]

Partly inherited from microelectronics technology, there are numerous methods to fabricate nanostructures. [15] Most of them require sophisticated setups, their operating costs are high, and they require a long time to cover large areas. Although these drawbacks can be neglected for research and development and prototyping purposes, mass production using these methods is not feasible. Therefore, there is always a need for economical fabrication methods. [11]

Inexpensive fabrication methods have two main advantages: first, they allow low budget research groups to conduct their studies and increase their research outcome. Second, at the industrial and public levels, decreased production and research and development costs make the final products inexpensively available to a larger community.

In this thesis, we are proposing that inexpensive fabrication methods can be used for biomedical applications. Two low cost fabrication methods are studied; in two different size regimes, the first is laser interference lithography, used to create a large area systematically changing nanostructure at 600 nm - 1200 nm, and the second is organometallic chemical vapor deposition (OMCVD), used to fabricate surface immobilized gold nanoparticles at 10 nm -20 nm. Both of them are used in applications, and results, limitations and future improvements are discussed.

1.2 Overview of the thesis

The first chapter includes the rationale for the research, and it is intended to give a brief overview of the methods covered in this thesis.

In the second chapter, creating surface patterns over a large area with laser interference lithography is investigated; creating biaxial periodic structures and also systematically

changing structures on one substrate is demonstrated. The importance of having a biaxial and variety of structures on one substrate for cell studies and plasmonic applications is discussed. Results of two different studies with osteoblast and osteoclast cells were discussed to show how the cells respond to different surface topographies. Also discussed is how these studies are promising to provide some insights about fundamental mechanisms in cell biology.

In the third chapter, creating surface-immobilized gold nanodisks by laser interference lithography in combination with lift-off technique is introduced, and plasmonic properties of the gold nanodisks for using them as a planar localized surface plasmon-based sensor platform is discussed. Finite difference time domain method used for simulating the plasmonic response of the nanodisks and results were compared with experimental findings.

In the fourth chapter, optimization details of the OMCVD process to obtain reproducible and stable gold nanoparticles on planar substrates were discussed, and then the systematic increase in the deposition time of OMCVD versus particle shape and UV-Vis absorption spectra of the samples was analyzed. Bulk refractive index and biotin-streptavidin sensing studies were compared with the literature to show that OMCVD-grown gold nanoparticles are suitable for developing highly sensitive plasmonic sensors, and they have a limit of detection of similar sensor platforms with further optimization possibilities.

The fifth chapter includes a similar-to-real-life example of epidermal growth factor receptor sensing with OMCVD-grown gold nanoparticles, and shows that carrying the

recognition reaction at the sensor surface significantly increases the sensor signal, improving the sensitivity and limit of detection. Antibody fragments were employed to functionalize the sensor surface; this strategy increased the signal about four times in comparison with a similar sensor platform using another coupling chemistry. Further optimization techniques are also discussed briefly.

Finally, in the sixth chapter, the results are summarized and limitations and further improvements are discussed.

1.3 Experimental techniques

1.3.1 Interference lithography

Photolithography also termed optical lithography is a micro-fabrication method to print patterns on planar surfaces. Photolithography uses light to transfer a pattern from a mask to a light-sensitive material −so called photoresist- coated substrate surface. The feature size is limited by the wavelength of the light that is used, and the capability of the reduction lens system to capture enough diffraction orders from the mask.

Interference lithography is a mask free lithography method to create periodic structures over large areas. From diffraction gratings to nanodots, a wide range of applications benefits from its simplicity and low operating cost. [16]–[18]

The establishment of the wave theory of light, after Young's double slit experiment; Humprey Lloyd showed the interference pattern of light using a mirror in 1843. It took more than a century to use Lloyd's interferometer as a patterning tool. In the 1970s, several groups started to use Lloyd's interferometer for creating holograms and diffraction gratings. [19][20]

The principle of interference lithography is simple; two coherent beams create a standing wave pattern, which is used to expose a photoresist layer. Depending on the photoresist type (positive or negative) either dark or bright lines are left on the photoresist surface after development. [21]

Lloyd's interferometry is not the only setup to perform interference lithography; the beam can also be split in two by a beam splitter, which is called dual beam interferometer. [22][23] Lloyd's interferometer has intrinsic geometrical limitations; a dual-beam interferometer can cover a larger area at the cost of a more complicated optical setup and sensitivity to air flow, which can cause phase fluctuations between the beams. There are also some studies reported using prisms. [21]

Besides coherence, power stability is also crucial for the light source that is used for interference lithography. Exposure is correlated with time and power; therefore, instability in the source power decreases reproducibility. Lasers are the most common light sources; cyclotron radiation and electron beams are also reported sources. [24][25]

Theoretically, the feature size that interference lithography could reach by splitting the beam in two is half of the wavelength of the laser used. Extreme ultraviolet (124 nm down to 10 nm) is required to reach a feature size on the order of tens of nanometers. [24][25]

A highly stable laser and a vibration free table are the main costs of the laser interference lithography (LIL) setup, which are very inexpensive in comparison with other nano-patterning approaches, such as focused ion beam (FIB) and electron beam lithography (EBL). In addition, exposure time, which is on the order of seconds with LIL, can take

days to create similar structures with FIB or EBL. On the other hand, LIL is limited to periodic structures such as gratings, dots, holes and variations on them.

1.3.2   Self-assembly and self-assembled monolayers

Self-assembly is a process in which disorganized compounds in a system form well-ordered molecular blocks due to special interactions between the molecules. There are many examples in nature resulting in supramolecular hierarchical structures of interlocking components that form highly complex systems. [26] Self-assembled monolayers (SAM) are organic molecular assemblies on a surface that spontaneously form organized domains by adsorption. Although the first SAM were reported in 1946 by Zisman, [27][28] starting from the 1980s, [26][27] there has been tremendous growth in research on SAMs, mainly driven by improvements in fabrication and characterization methods used in nanotechnology.

The attraction between the head group of the molecule and the surface is the driving force to form SAMs. A combination of diffusion and convection carries the molecules to the surface and is followed by adsorption. Depending on the concentration, adsorption happens in minutes; however, it requires several hours for molecules to organize themselves in densely packed uniform blocks over the surface. [27]–[29]

Freedom of tailoring the head and tail groups of the molecules individually provides great flexibility for surface functionalization. For metal surfaces, alkanethiols, and for nonmetallic oxide surfaces (oxidized glass, silicone etc.) silanes are commonly used head groups for self-assembly processes. [27]–[29]

Self-assembly can be performed on a laboratory bench in liquid phase at room temperature by employing various solvents. While such conditions work for most applications, creating high quality SAM is still a challenge, since possible contamination and humidity greatly affect the process and lead to less uniform SAM with low reproducibility. [29] Therefore, gas phase with ultrahigh vacuum provides a cleaner controlled environment to improve SAM quality and reproducibility. [26]

Self-assembly can be used to functionalize the surface of substrates for many different applications, such as controlling wetting, providing selectivity for chemical vapor deposition, controlling friction and lubrication, creating a recognition layer on the surface for biosensing purposes, etc. [27]–[29]

1.3.3   Chemical vapor deposition

Chemical vapor deposition (CVD) is a method for deposition of a thin solid chemical material in the gas phase by a chemical reaction. [30] Providing uniform surface coverage over large areas and selective deposition are the main advantages of CVD over physical deposition methods such as physical vapor deposition, sputtering, etc. [31][32]

Some sources say [30] there are some prehistoric art forms that used incomplete burning of firewood to deposit pyrolytic carbon onto cave walls, which may be an example of CVD. In 1855, tungsten deposition was reported by the method of CVD. [30] In 1880, there was a patent issued for improving the carbon filaments of lamps by CVD. [30] More applications followed; however, starting with the development of microelectronics in the 1970s, CVD became a widely used tool for the industry. In the last several decades, it became an indispensible method for nanotechnology.

CVD is a complex process involving heat transport, fluid mechanics, diffusion, surface chemistry, gas phase chemistry and crystal growth. [30][33][34] In a typical CVD setup, the substrate is exposed to a volatile precursor in a reaction chamber; then it reacts with the surface of the substrate and forms the desired product. Numerous setups are used; most of them introduce the precursor by gas flow, and by-products are removed from the chamber. [30], [33]

In contrast to physical deposition techniques, the substrate is chemically selective, and therefore CVD yields less contaminated and higher purity films. Furthermore, it is possible to create growth and non-growth regions on the same substrate by controlling the surface functionalization locally. [35]

Depending on the attraction forces of the surface and the material onto which the substrate will be deposited, there are several different growth mechanisms observed. It all starts with nucleation, when an atom reacts with the surface. If the attraction between the surface and the atom is larger than the attraction between the atoms, layer-by-layer deposition is observed. This is called Frank–van der Merwe growth. Otherwise, island growth is observed, which is called Volmer–Weber growth. In the Stranski–Krastanow growth mode, deposition of one or two monolayers is followed by island growth. [36]–[38]

Metal deposition can be achieved by employing organometallic precursors. As the name suggests, organometallic compounds contain both organic and metallic parts. A volatile precursor is carried to the surface by the carrier gas, convection or diffusion or a combination of all, and a surface reaction happens. Figure 1.1 illustrates the mechanism of organometallic chemical deposition used in this thesis. [34] Evaporated precursor

molecules moves by convection and diffusion and reacts with the surface to create nucleation sites of gold and nucleation fallows growth. By-products move away from the surface. Chemical reaction may also occur in the gas phase or at the reactor surface depending on the conditions. Gas phase reaction can lead to nucleation of undesired components on the surface, which may lead to impurities. Chamber surface reactions are mostly a problem of hot wall reactors, which may cause deposition on the reactor surface and lead to wasting the precursor. Functionalizing the surface to create nongrowth areas avoids deposition on the surface. [39]
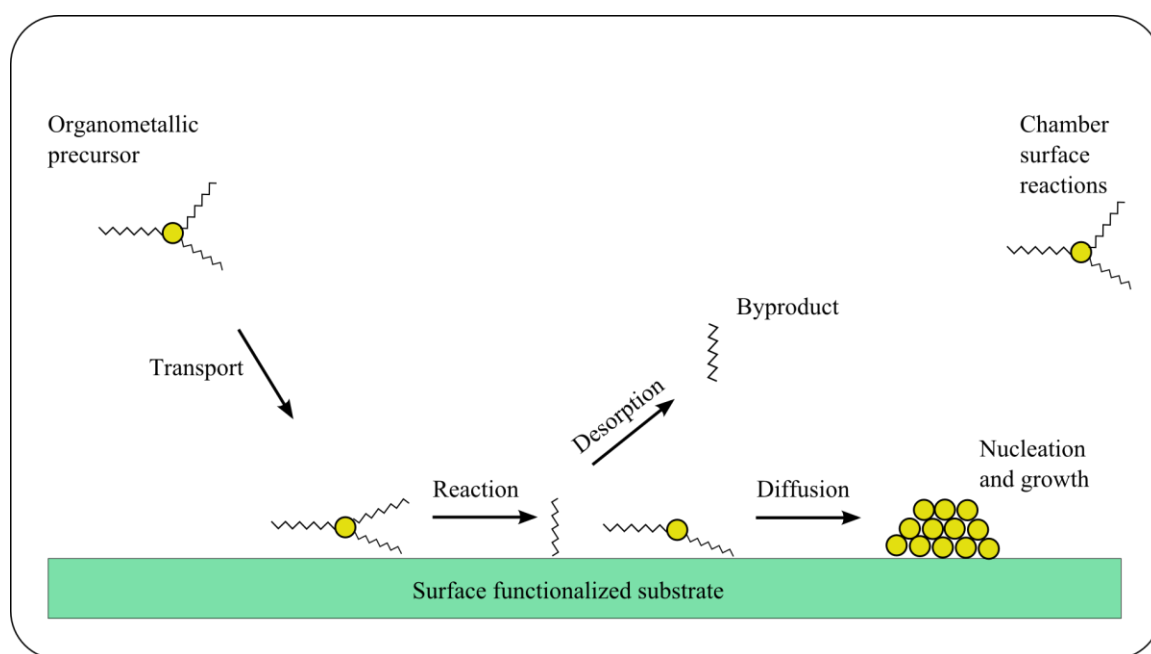
Figure 1.1. Illustration of OMCVD reaction mechanism [34]

1.3.4   Localized surface plasmon resonance based sensing

Biosensors are devices that convert the presence or the concentration of a specific biomolecule to a physically measurable signal. Their use is not limited to biomedical

applications; food control and environmental monitoring applications also require biosensors. There is always a demand for increased sensitivity and low cost sensing technologies. [40]

A surface plasmon is defined as collective oscillations of electron density at a metal dielectric interface. If the frequency of incoming light matches the oscillation frequency of the surface plasmons, a resonance condition occurs, and this is called surface plasmon resonance. For metallic nanoparticles, electrons are confined in a nanoscale volume (Figure 1.2) known as a localized surface plasmon resonance (LSPR). Plasmon resonance frequency is a function of the material, its shape and size, the dielectric medium and the distance between other metallic particles, if there are any. [41]–[46] In the resonance condition field enhancement happens around the particle this exponentially decaying electric field called evanescent field. Particle absorbs maximum energy at the resonance frequency therefore particle absorbs light at that frequency. Resonance frequency is a function of size, shape, composition of surrounding medium [50].
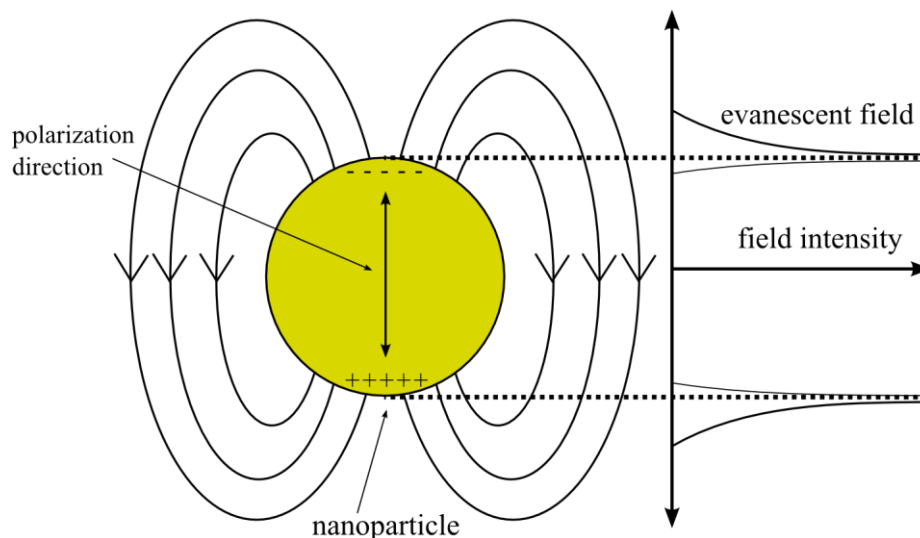
Figure 1.2. Illustration of localized surface plasmon resonance

Because of LSPR, metallic nanoparticles exhibit extraordinary spectroscopic properties, which make them ideal for designing highly sensitive biosensors. Gold has a special importance among metallic nanoparticles because of its stability and resistance to oxidation. Furthermore, the plasmon resonance frequency of gold is in the visible region, so therefore it is easy to analyze its absorption properties.

The majority of LSPR based sensors are based on resonance change due to changing the refractive index around the nanoparticle. The metallic surface is modified to catch only the target molecule. When the molecule is caught, the refractive index change around the nanoparticle causes a blue shift in the absorption spectrum, which can be detected by a spectrometer. Coupling chemistry between the metal and the target molecule not only determines the selectivity but also has an effect on the overall sensor quality. [47]

Developing a high quality sensor is challenging work. In order to avoid fabrication costs at the design stage, simulation methods are employed to predict the most effective sensor design. However, it is highly critical to ensure that the simulation is validated with experiments and simulated structures match with reality. Classical electrodynamics successfully explains the LSPR phenomenon. [48]–[50] However, due to the complex nature of the problem, only spherical nanostructures can be solved analytically. [51] On the other hand, there are several numerical approaches and related software is available; finite difference time domain (FDTD) method is used in Chapter 4 to simulate plasmonic response of gold nanodisks in parallel with the experimental results.

1.4 Characterization methods

1.4.1 Scanning electron microscope

Scanning electron microscope is an imaging method, which uses electrons instead of photons to image a substrate (Figure 1.3). Magnets serve as lenses to manipulate the electron beam. Accelerated electrons hit the substrate surface. Scan coils changes the direction of the electron beam to scan the substrate surface. Once the beam hits the sample, electrons and X-rays are ejected from the sample. Detectors collect X-rays, backscattered electrons, and secondary electrons to convert them into a signal. Collected signals are converted to the image with the help of a computer. Sample surface must be electrically conducting, otherwise the electron beam would charge up the surface. Nonconductive samples can be coated with a thin film of a conductive material such as gold, carbon or osmium.
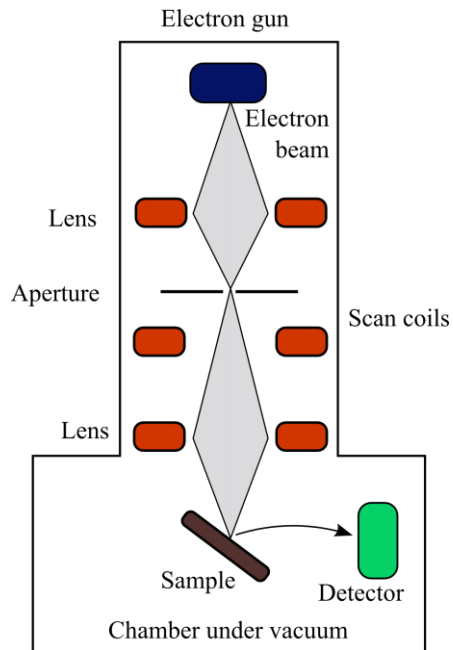
Figure 1.3. Illustration of scanning electron microscope

1.4.2   Absorption spectroscopy

Absorption spectroscopy is a spectroscopic technique that measures the absorption of light, as a function of frequency or wavelength, due to its interaction with a sample. The sample absorbs the photons, from the light source. The intensity of the absorption varies as a function of frequency, and this variation is the absorption spectrum.
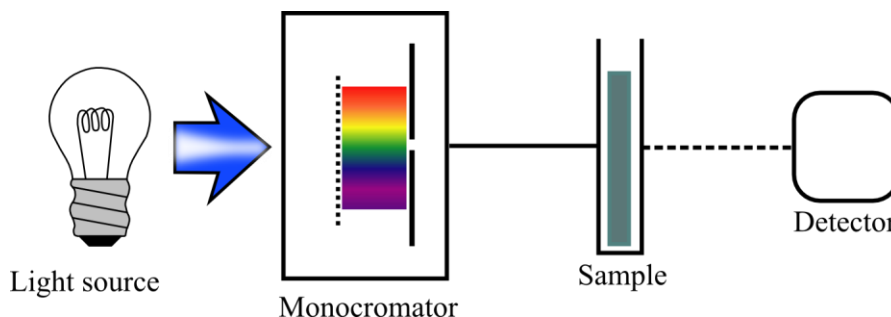
Figure 1.4. Schematic diagram of absorption spectrometer

Figure 1.4 shows a typical absorption spectrometer setup. Light from the source goes to a monocromator which consists of diffraction grating or prism and a slit. The output wavelength of the monochromator can be adjusted and desired range of the electromagnetic spectrum is scanned. Detector collects the light goes through the sample. Reference spectrum, that is the spectrum without sample should be collected to normalize, in order to obtain the absorption caused by the sample. There are various spectrometers to cover the different ranges of the electromagnetic spectrum such as; UV-Visible, visible-infrared. Some spectrometers contain several sets of light sources and the detectors to cover a wide range.

1.4.3 Finite difference time domain method

Surface plasmon resonance phenomenon can be explained by classical electromagnetic theory. Mie solutions describe the scattering of electromagnetic radiation by a sphere with analytically solving Maxwell's equations. However, for the complex geometries light matter interaction cannot be solved analytically. Finite difference time domain (FDTD) is a numerical technique for solving Maxwell's equations in arbitrary shaped metallic/dielectric structures. FDTD discretizes the simulation space into nodes and

substitute the curl equations and partial time differentials of Maxwell's equations with finite central differences in both spatial domain and time domain [52,53].

Using FDTD simulations, metallic nanoparticles of any arbitrary shape and compositions can be accurately simulated. Since FDTD is a time domain method meaning that from one simulation, the optical response over a broadband of frequencies could be acquired through discrete Fourier transforms. FDTD allows visualizing plasmonic modes, near and far field intensity distributions and absorption, transmission and reflection characteristics of the simulated structure.

In this thesis commercial FDTD package of Lumerical Inc. is used for simulating the plasmonic response of gold nanodisks.

References

[1] P.M. Tiwari, K. Vig, V. a. Dennis, S.R. Singh, *Nanomaterials* **2011**, *1*, 31.

[2] X. Huang, P.K. Jain, I.H. El-Sayed, M. a El-Sayed, *Nanomedicine (London, England)* **2007**, *2*, 681.

[3] J.Y. Lim, H.J. Donahue, *Tissue Engineering* **2007**, *13*, 1879.

[4] R.J. Miron, E. Hedbom, S. Ruggiero, D.D. Bosshardt, Y. Zhang, C. Mauth, A.C. Gemperli, T. Iizuka, D. Buser, A. Sculean, *PloS One* **2011**, *6*, e23375.

[5] T.P. Kunzler, C. Huwiler, T. Drobek, J. Vörös, N.D. Spencer, *Biomaterials* **2007**, *28*, 5000.

[6] C. Escobedo, Y. Chou, M. Rahman, X. Duan, *Analyst* **2013**.

[7] E.E. Bedford, J. Spadavecchia, C.-M. Pradier, F.X. Gu, *Macromolecular Bioscience* **2012**, *12*, 724.

[8] J.-J. Tsai, I.-J. Bau, H.-T. Chen, Y.-T. Lin, G.-J. Wang, *International Journal of Nanomedicine* **2011**, *6*, 1201.

[9] R.J. Miron, C.J. Oates, A. Molenberg, M. Dard, D.W. Hamilton, *Biomaterials* **2010**, *31*, 449.

[10] M.J.P. Biggs, R.G. Richards, N. Gadegaard, C.D.W. Wilkinson, R.O.C. Oreffo, M.J. Dalby, *Biomaterials* **2009**, *30*, 5094.

[11] S.G. Kumbar, M.D. Kofron, L.S. Nair, C.T. Laurencin, in *Biomedical Nanostructures*, John Wiley & Sons, Inc.**2007**, 261.

[12] T.P. Kunzler, T. Drobek, M. Schuler, N.D. Spencer, *Biomaterials* **2007**, *28*, 2175.

[13] M.J.P. Biggs, R.G. Richards, N. Gadegaard, C.D.W. Wilkinson, M.J. Dalby, *Journal of Materials Science. Materials in Medicine* **2007**, *18*, 399.

[14] D.W. Hamilton, D.M. Brunette, *Biomaterials* **2007**, *28*, 1806.

[15] J.W. Freeman, L.D. Wright, C.T. Laurencin, S. Bhattacharyya, in *Biomedical Nanostructures*, John Wiley & Sons, Inc.**2007**, 1.

[16] M. Zheng, M. Yu, Y. Liu, R. Skomski, S.H. Liou, D.J. Sellmyer, V.N. Petryakov, Y.K. Verevkin, N.I. Polushkin, N.N. Salashchenko, *Applied Physics Letters* **2001**, *79*, 2606.

[17] V. Berger, O. Gauthier-Lafaye, E. Costard, *Electronics Letters* **1997**, *33*, 425.

[18] K. Petter, T. Kipp, C. Heyn, D. Heitmann, C. Schüller, *Applied Physics Letters* **2002**, *81*, 592.

[19] W. Ng, C. Hong, *Electron Devices, IEEE* **1978**, *25*, 1193.

[20] S. Austin, F.T. Stone, *Applied Optics* **1976**, *15*, 1071.

[21] H. Wolferen, L. Abelmann, in *Science*, Nova Publishers**2011**, 133.

[22] J. Spallas, A. Hawryluk, D. Kania, *Journal of Vacuum Science & Technology B: Microelectronics and Nanometer Structures* **1995**, *13*, 1973.

[23] A. Fernandez, J. Decker, S. Herman, *Journal of Vacuum* **1997**, *15*, 2439.

[24] V. Auzelyte, C. Dais, P. Farquet, D. Grützmacher, L.J. Heyderman, F. Luo, S. Olliges, C. Padeste, P.K. Sahoo, T. Thomson, A. Turchanin, C. David, H.H. Solak, *Journal of Micro/Nanolithography, MEMS and MOEMS* **2009**, *8*, 021204.

[25] L. Wang, H.H. Solak, Y. Ekinci, *Nanotechnology* **2012**, *23*, 305303.

[26] A. Ulman, *Chemical Reviews* **1996**, *96*, 1533.

[27] F. Schreiber, *Progress in Surface Science* **2000**, *65*, 151.

[28] D. Schwartz, *Annual Review of Physical Chemistry* **2001**, 107.

[29]   J.C. Love, L. a Estroff, J.K. Kriebel, R.G. Nuzzo, G.M. Whitesides, *Self-assembled Monolayers of Thiolates on Metals as a Form of Nanotechnology.*, **2005**.

[30]   T. Kodas, *Advanced Materials* **1994**, *6*, 87.

[31]   C. Winter, U. Weckenmann, R.A. Fischer, * J. Käshammer, V. Scheumann, S. Mittler, *Chemical Vapor Deposition* **2000**, *6*, 199.

[32]   J. Käshammer, P. Wohlfart, J. Weiß, C. Winter, *Optical Materials* **1998**, *9*, 406.

[33]   J.H. Park, T.S. Sudarshan, *Chemical Vapor Deposition*, A S M International**2001**.

[34]   T. Kodas, M.J. Hampden-Smith, *The Chemistry of Metal CVD*, VCH**1994**.

[35]   A. Rezaee, K.K.H. Wong, T. Manifar, S. Mittler, *Surface and Interface Analysis* **2009**, *41*, 615.

[36]   N. Kaiser, *Applied Optics* **2002**, *41*, 3053.

[37]   M. Zinke-Allmang, *Thin Solid Films* **1999**, *346*, 1.

[38]   F. Ratto, G. Costantini, A. Rastelli, O.G. Schmidt, K. Kern, F. Rosei, *Journal of Experimental Nanoscience* **2006**, *1*, 279.

[39]   D. Trovo, E. Ertorer, R. Huang, T. Cheng, C. Rangan, S. Mittler, in *Modern Aspects of Electrochemistry*, **2013**, 104.

[40]   K. Gonsalves, C. Halberstadt, C.T. Laurencin, L. Nair, *Biomedical Nanostructures*, Wiley**2007**.

[41]   P.K. Jain, K.S. Lee, I.H. El-Sayed, M. a El-Sayed, *The Journal of Physical Chemistry. B* **2006**, *110*, 7238.

[42]   S.M.H. Rafsanjani, T. Cheng, S. Mittler, C. Rangan, *Journal of Applied Physics* **2010**, *107*, 094303.

[43] F. Toderas, M. Baia, L. Baia, S. Astilean, *Nanotechnology* **2007**, *18*, 255702.

[44] E. Hutter, J.H. Fendler, *Advanced Materials* **2004**, *16*, 1685.

[45] W. Rechberger, A. Hohenau, A. Leitner, J.R. Krenn, B. Lamprecht, F.R. Aussenegg, *Optics Communications* **2003**, *220*, 137.

[46] K.-H. Su, Q.-H. Wei, X. Zhang, J.J. Mock, D.R. Smith, S. Schultz, *Nano Letters* **2003**, *3*, 1087.

[47] R. Förch, H. Schönherr, A. Jenkins, *Surface Design: Applications in Bioscience and Nanotechnology*, Wiley**2009**.

[48] A. Unger, **2010**.

[49] G. Schatz, *Spring* **2005**, *7*, 2032.

[50] C. Noguez, *The Journal of Physical Chemistry C* **2007**, *111*, 3806.

[51] T. Jensen, L. Kelly, A. Lazarides, G.C. Schatz, *Journal of Cluster Science* **1999**, *10*, 295.

[52] K. Yee, "Numerical solution of initial boundary value problems involving Maxwell's equations in isotropic media," *Antennas and Propagation, IEEE Transactions on*, 1966.

[53] A. Tavlove and S. Hagness, *Computational electrodynamics: the finite-difference time-domain method*. 1995.

Chapter 2

Large Area Periodic, Systematically Changing, Multi-Shape Nanostructures by Laser Interference Lithography and Cell Response to these Topographies[1]

2.1   Introduction

Nano-scale periodic structures have gained research attention in the last decades as a result of improvements to nanofabrication and related characterization methods. Their applications include optical gratings [1], photonic crystals [2], bio-sensors [3]–[5], and fabrication of surface topographies for microbiological studies [6]–[10]. There are several ways to create nanoscale patterns, but most of them, e.g. electron beam lithography (EBL) and focused ion beam lithography (FIB) have low fabrication speed and typically require complex instrumentation. Laser interference lithography (LIL) is a simple and relatively inexpensive technique to create periodic structures over large areas [11][12]. The Lloyd's interferometer provides a flexible setup for laser interference lithography with the possibility to create nanoscale structures at different periodicities without additional optical alignment modifications [11][12].

---

[1] A version of this chapter has been published as follows; E. Ertorer, F. Vasefi, J. Keshwah, M. Najiminaini, C. Halfpap, U. Langbein, J.J.L. Carson, D.W. Hamilton, S. Mittler, Journal of Biomedical Optics **2013**, 18, 35002. (See appendix A for copyright permission.)

Most researchers using Lloyd's systems have focused on creating uniform patterns over large areas [13][14]. However, for some studies, especially those in the early device development stage, where systematic variation of parameters is necessary, fabrication of a variety of multiple or gradually changing structures on a single substrate is the desired goal. A typical example is the study of the influence of surface topographies in a systematic fashion in the field of cell biology, where the objective is to examine how cells respond to lines, broken lines and dots, or combinations of them on microscopic to nanoscopic scales [15]–[18]. Another example is the expanding field of plasmonics, where structures of different sizes and periodicities correspond to different resonance conditions [19]–[23]. Furthermore, structures with biaxial periodicities enable cases where it is critical to implement different periodicities on the *x*- and *y*-axes therefore enabling two measurements on one sample by simply considering the polarization direction of the probing light [24]. Exploiting biaxial periodicity by polarized light is especially applicable to surface enhanced Raman spectroscopy (SERS) whereby an active substrate with multi-wavelength or tunable excitation can be created [24]. Therefore, fabrication of structures with biaxial periodicity facilitates parallel experimentation, which reduces sample preparation time, decreases the number of independent experiments needed and enables rapid optimization of experimental conditions.

In this paper, we describe a LIL method to create large scale, periodic and biaxial periodic, systematically varying multi-shape structures on a single substrate. First, we computed the optimal parameters for a Lloyd's mirror interferometer implementing a Gaussian laser beam intensity distribution to achieve a large intensity variation along the substrate. Second, we fabricated various multi-shape periodic and biaxial periodic

structures by using different exposure times and exposure angles. The fabricated structures were analyzed with SEM. Finally, ion-milled glass substrates carrying patterns as surface topography were used for cell adhesion experiments.

2.2   Methods

2.2.1   Theory

Two coherent beams on a plane create an interference pattern. This pattern can be used to expose a photoresist layer to create permanent structures[12]. The Lloyd's mirror interferometer consists of a mirror placed perpendicular to the sample plane (see Fig. 2.1a). When a diverging laser beam from a spatial filter (lens and pinhole) illuminates a Lloyd's interferometer, the sample is exposed both to the direct beam and to the reflected beam. The addition of two laser beams creates a light intensity interference pattern on the substrate. The periodicity of the pattern (Λ) is given by Lloyd's interferometer equation [12].

$$\Lambda = \frac{\lambda}{2sin\theta} \qquad (2.1)$$

where, λ is the wavelength of the laser beam, and θ is the angle between the mirror and the axis of the direct laser beam (optical axis of the system).

A Gaussian beam intensity distribution on the substrate for Lloyd's interferometer created by the direct and reflected beams can be represented by equation (2) [25]:

$$I = 2I_0 Exp\left(\frac{-2x^2}{\omega_r^2 cos^2\theta} + \frac{-2y^2}{\omega_r^2}\right) \qquad (2.2)$$

where, I_0 is the peak intensity of the beam, x and y are the distances from the center of the beam, ω_r is the Gaussian beam radius at the distance of the substrate, which is defined as the distance for an intensity decrease to $1/e^2$ from its maximum value, and θ is the angle between the mirror and the optical axes of the experiment (central line of the direct laser beam).

For larger values of magnification and larger distances between the pinhole and sample, the intensity distribution becomes relatively flat along the surface of the mirror geometry yielding uniform structures. This large distance geometry is used by most researchers implementing the Lloyd's mirror interferometer. On the other hand, confining the Gaussian beam or bringing the Lloyd's mirror setup closer results in a higher variation of the intensity along the sample and mirror. A distinct intensity variation can create various photoresist structures on the substrate. Creating two-dimensional structures can be achieved by rotating the photoresist coated substrate by rotating 90° and then applying a second exposure. For instance, the intensity distributions for the first, the second, and the total exposures of an experiment with d = 23.5 cm, ω_0 =1.9 mm, and θ = 14º on a sample at a size of 4×4 cm^2 are illustrated in Figure 2.1b.
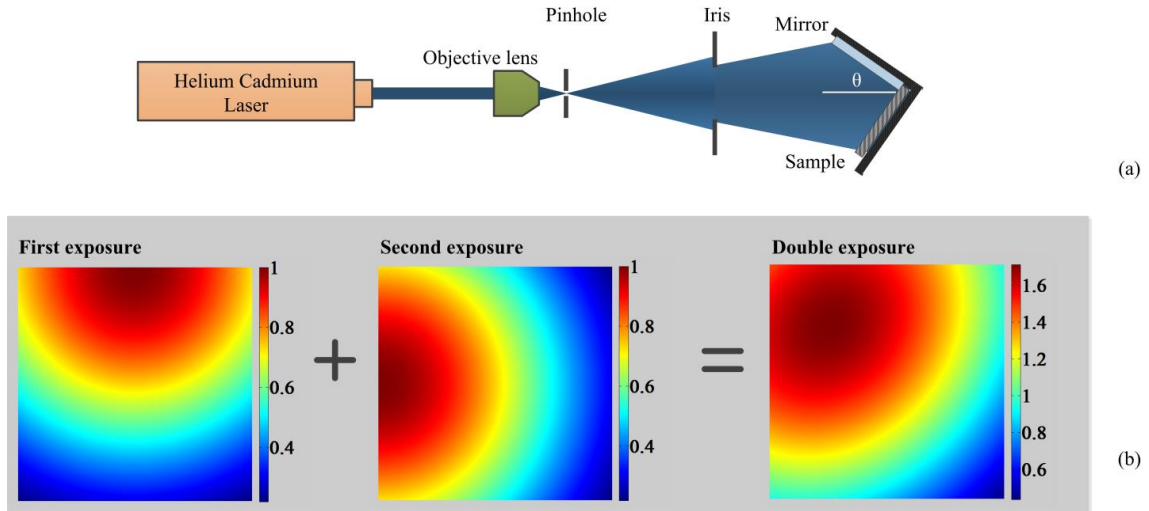
Figure 2.1. (a) Lloyd's interferometer setup. (b) Intensity distribution of two individual exposures and the sum due to the double exposure.

2.2.2   Experimental

A 442 nm wavelength HeCd Laser (Omnichrome Series 74, Model 4074-P-A03, CVI Melles Griot, NM, USA) with a coherence length L_c = 30 cm was operated at 80 mW. The 1.5 mm diameter laser beam passed through a lens-pinhole system built with a 20X objective lens (Zeiss LD Plan-Neofluar 20X/0.4 Corr Ph2), and a 5-µm pinhole mounted on a three axis stage (Newport Three-Axis Spatial Filter, Model M-900, Newport, CA, USA). A time-controlled shutter was situated between the laser and the objective lens to control the exposure time during each experiment. The pinhole was used to remove undesirable components of the laser beam such as donut mode contributions. An iris was used to prevent reflections of the expanded laser beam. The Lloyd's mirror/sample was placed on a two axis stage (*X* and *θ*) in such a way that the common corner of the sample and the mirror was located on the optical axis. The distance between the sample and the pinhole along the direction of the optical axis was 23.5 cm.

2.2.3   Fabrication of nanostructures

Experiments were performed with (2.5 x 2.5) cm^2 Fisher Brand microscope slides (soda lime glass) or (2.5 x 2.5) cm^2 fused silica slides (Valley Design Corp., USA) immersed in Nano-Strip (Cyantec Inc., CA, USA) at 60°C for 20 minutes to remove possible organic and inorganic contamination. In order to increase the adhesion of the photoresist, substrates were silanized with hexamethyldisilazane (HMDS) in an oven (YES-3TA HDMS Oven, Yield Engineering, CA, USA). Then substrates were spin-coated at 4000 rpm for 45 seconds with 1:4 Shipley S1805 photoresist (Shipley, MA, USA) diluted with Microposit Thinner Type P (Shipley, MA, USA). Samples were soft-baked for five minutes at 115°C on a hot plate. The resultant photoresist thickness was 320 ± 10 nm found by analysis of electron microscopy images of FIB cut samples. To achieve the photoresist structures which have the same periodicity on both axes, samples were fabricated with a mirror-laser beam axis angle $\theta \sim 15°$ yielding a periodicity Λ of ~ 800 nm. The sample was exposed first for 18 seconds, rotated by 90° and exposed a second time for 18 seconds. A second sample was exposed first for 18 seconds, then 12 seconds after the rotation.

For the biaxial periodic structures, which have different periodicities in x- and y- axes-, θ was set to $\sim 11°$ yielding a periodicity Λ of ~ 1200 nm. After the first exposure, (for various times) the sample was developed, then placed in the Lloyd's setup rotated 90° with respect to the first exposure and exposed a second time (for various times) at an angle θ of $\sim 15°$ to obtain a periodicity Λ of ~ 800 nm.

Substrates were developed in MF319 developer (Shipley, MA, USA). Symmetric structures were developed once after the two exposures. Biaxial structures were

developed twice, once after the first exposure and then again after the second exposure. The first development was 45 seconds; the second development was 20 seconds. After each development, substrates were rinsed with copious amounts of deionized water and dried under nitrogen. Finally, samples were hard-baked for ten minutes at 115°C on a hot plate. All the procedures were performed in a clean room facility at 21.5 ± 0.5ºC with relative humidity of $30 \pm 10\%$, and under yellow light.

The photoresist patterns were also used as etching masks for the fabrication of metallic or silicon nanofeatures. A 300 nm photoresist layer was spun on a p-type silicon substrate (500 µm thickness) with a 30 nm chromium layer deposited by an electron-beam evaporation system. The photoresist acted as an etching mask for the chromium layer resulting in a chromium pattern identical to the photoresist pattern. The patterned chromium nanostructures acted as a masking layer for silicon ion etching. Therefore, the pattern and objects fabricated lithographically in photoresist were transferred to the chromium layer by wet etching as well as the silicon wafer by deep reaction ion etching (DRIE; Alcatel 601E Deep Silicon Etch).

Fused silica samples carrying line and dot structures at a periodicity of 1200 nm in photoresist were ion milled (Vacu Tec Plasma Systems: control unit CPU 500, matching Plasmamatch; ENI: RF-generator ACG-3XL; Witney, Oxfordshire, UK) with SF_6 at a gas flow rate of 20 sccm, 200W plasma power and a pressure of ~8 Pa for 3 minutes. Under these conditions, surface topography with a profile depth of ~100 nm was achieved. The structures were analyzed with SEM after ion milling to acquire the profile depth. The fused silica nanotopographic samples were used in the cell studies.

2.2.4　Osteoblast culture

All studies involving rats were performed in compliance with the University Council on Animal Care at the University of Western Ontario under approved protocols. Rat calvarial osteoblasts (RCOs) were obtained from newborn rat calvariae and cultured as previously described [26].

2.2.5　Osteoclast isolation

Primary osteoclasts were isolated from the long bones of neonatal Wistar rats. All procedures were approved by Council on Animal Care of The University of Western Ontario and were in accordance with the guidelines of the Canadian Council on Animal Care. Briefly, long bones were dissected free of soft tissue and minced with a scalpel in M199 buffered with HEPES (25 mM) and HCO_3^- (26 mM) supplemented with 15% FBS and 1% antibiotic-antimycotic solution. The resulting cells were suspended by repeated passage through a glass pipette and plated on FBS coated nano-grooves made of S1805 photoresist (Shipley, MA, USA) with 1200 nm periodicity on coverslips. Following plating, osteoclasts were incubated at 37°C in 5% CO_2 for 1 hour, gently washed with phosphate buffered saline (PBS) to remove non-adherent cells and then incubated in fresh medium for 0.5-2 hours before use.

2.2.6　Immunocytochemistry

Osteoblasts were plated at a density of 39 cells/mm^2 and were fixed in 4% paraformaldehyde at 24 h post-seeding. Samples were then stained with rhodamine-conjugated phalloidin (Sigma-Aldrich, Canada), 4,6-diamidino-2-phenylindole dihydrochloride (DAPI) (Sigma-Aldrich, Canada), and vinculin (Sigma-Aldrich, Canada) as previously described [7][26]. Images were captured from each surface on an AxioScope

microscope (Zeiss, Germany) using an Axiocam digital camera and AxioImager software.

2.2.7   Time lapse microscopy of osteoclast cells

For time lapse video microscopy isolated rat osteoclasts were plated on FBS-coated nano-grooves made of S1805 photoresist (Shipley, MA, USA) on coverslips with 1200 nm periodicity. Following one hour incubation, the medium was then replaced with supplemented M199 buffered with HEPES (25 mM) and HCO_3^- (4 mM). Dishes were placed in a stage warmer (35 °C) mounted on a Nikon microscope (Nikon Eclipse TE2000-U, Tokyo, Japan). Osteoclasts were imaged using a Plan Fluor 20x/0.45 NA for phase contrast time-lapse microscopy. Images were acquired every 10 seconds with a Cascade Photometrics 650 cooled charge-coupled device (CCD) camera (653 x 492 pixels; Roper Scientific Inc., Tucson, Arizona) and ImageMaster 5 Software (PTI Inc.)

2.3   Results

2.3.1   2D Multi-shaped structures

To correlate nanostructure shape with corresponding exposure and light intensity conditions, nine regions on each device were chosen and characterized. Figure 2.2 shows the exposure intensity map as well as the selected regions where SEM images were taken. The first region $R_{(0,0)}$ was chosen at the origin of the *xy*-coordinate system and corresponded to the location with the highest exposure intensity. The remaining eight regions were distributed 10 and 15 mm, respectively away from the origin in both *x*- and *y*-directions. For instance, $R_{(10,15)}$ represented the region that was displaced 10 mm in the *x*-direction and 15 mm in the *y*-direction relative to the origin. As Figure 2.2 shows, the

nanostructure shape correlated directly with the exposure time and the beam intensity at each region.

In the case of the equivalent double exposure of sample 1, it was expected from the Equation 1 that the exposure intensity dropped by 6% and 14% at a distance of 10 and 15 mm away from the highest value at the origin, respectively. The diagonal in the *xy*-coordinate system was an axis of symmetry for the substrate. At the origin, ($R_{(0,0)}$ in Figure 2.2b), round pillars were observed. Moving from the origin to $R_{(10,10)}$ dot diameter gradually increased and some were connected. After passing $R_{(10,10)}$, connected dots formed holes and at $R_{(15,15)}$ the exposure was not high enough for developer to etch the photoresist through to the substrate.

For areas off the axis of symmetry, either the *x*- or the *y*- component was elongated with respect to the other: elongated meaning that when lines form, the lines were along the *x*-direction on the right hand side of the symmetry line and along the *y*-direction on the left hand side of the symmetry line. The directions of the long axes of ellipses were analogous. The result was that $R_{(10,0)}$ contained objects elongated in the *x*-direction and $R_{(0,10)}$ contained structures elongated in the *y*-direction.

The elongation trend continued into wavy lines in either of the directions. The off diagonal areas $R_{(10,15)}$ and $R_{(15,10)}$ contained broad wavy lines that were well-separated from one another. The ensemble of the wavy lines can be interpreted as the pre-structure for the hole array located on the axis of symmetry at $R_{(15,15)}$ obtained with an exposure of lower intensity.

Another observation from Figure 2.2 was the fact that in the high intensity areas, separated islands or nanodots were formed, and with decreasing illumination intensity, the structures became connected with sharp linear features. Further decreases in the intensity led to a shape inversion, i.e. the formation of nanoholes.

The use of different exposure times when the substrate was in the x- and y-orientations in sample 2 resulted in samples with unique nanostructures within each region. Figure 2.2d clearly shows that the overall structure was not symmetric with respect to the diagonal. For example, the nanostructures in $R_{(10,0)}$ had a linear shape, while the nanostructures in $R_{(0,10)}$ were nominally oval-shaped. Furthermore, the nanostructures formed at the $R_{(0,0)}$ in Figure 2.2d were slightly elongated in the x-direction, making them elliptical, while the nanostructures observed at $R_{(0,0)}$ in Figure 2.2b were nearly circular.
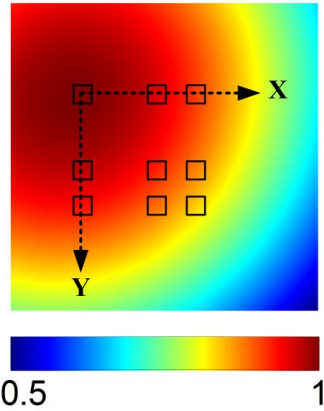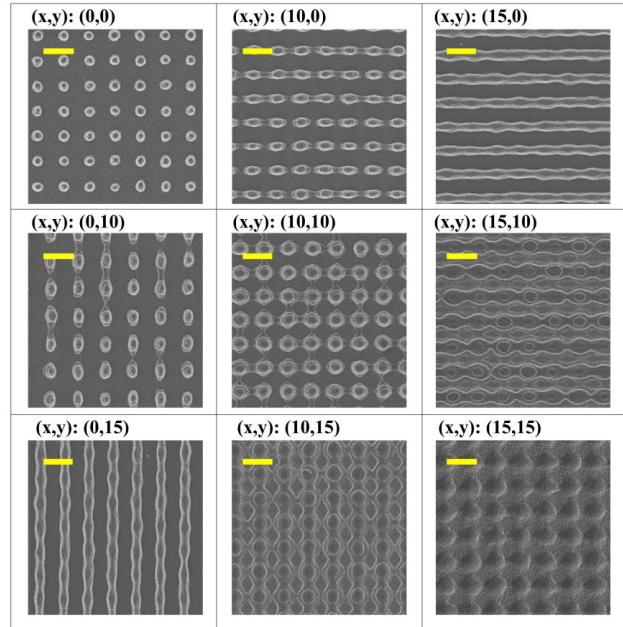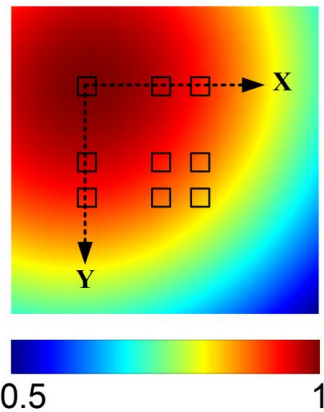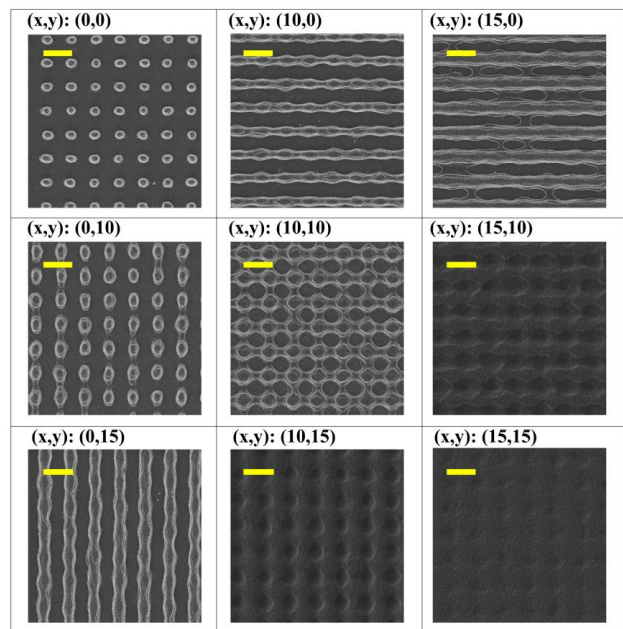
Figure 2.2. Illumination intensity maps and SEM images of photoresist patterns of samples fabricated with LIL. (a) Cumulative illumination intensity map for 18+18 seconds of exposure. (b) Cumulative illumination intensity map for 18+12 seconds exposure. (c and d) SEM images of nine selected regions from samples receiving illumination corresponding to (a) and (b), respectively. Location of each image corresponds to the location indicated in the accompanying illumination intensity map. Scale bars represent 1 μm.

2.3.2 Nanostructures with biaxial periodicity

The combination of different exposure time, different exposure angles for the *x*- and *y*-axes, and post processing resulted in a wide variety of structures with controllable biaxial periodicity and morphology, including dots, holes, ellipses, elliptical holes, lines, and wavy lines at $R_{(0,0)}$. For instance, Figure 2.3a shows elliptical nanodots in photoresist on a glass substrate with 1200 nm periodicity on the *x*-axis and 800-nm periodicity on the *y*-axis that resulted from exposure sets of 20+20 seconds. Figure 2.3b shows elliptical nanoholes in photoresist on a glass substrate with similar biaxial periodicity to the structure in Figure 2.3a that resulted from an exposure set of 22+18 seconds. Figure 2.3c and Figure 2.3d show silicon nanopillar and nanohole structures with a height equal to 300 nm. In order to achieve 800 nm spacing on the *x*-axis and 1200 nm on the *y*-axis, the exposures sets of 15+25 seconds and 11+22 seconds were used to form nanodots and nanoholes, respectively.
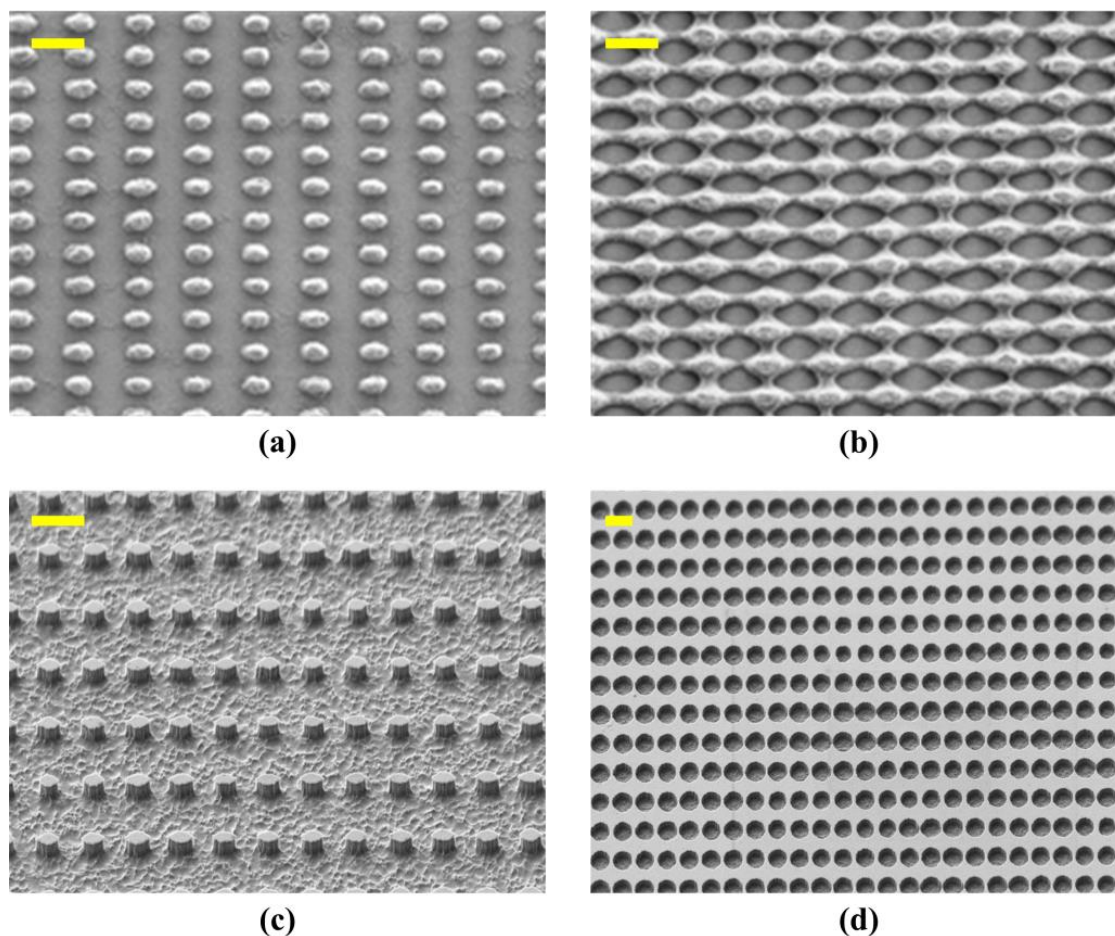
Figure 2.3. SEM images of nanostructures with biaxial periodicity (a) ellipses (in photoresist), (b) elliptical holes (in photoresist), (c) round pilars (in silicon), and (d) round holes (in silicon). Scale bars represent 1 µm.

2.3.3 Cell response to nanotopographies

We tested the influence of the nanotopographies, explicitly a dot pattern (Figure 2.4a) and a line pattern (Figure 2.4b), on the adhesion and spreading of primary rat calvarial osteoblasts (Figure 2.5). The vinculin stain (green) depicts the adhesions of the cell onto its substratum, whereas the f-action (red) depicts actin microfilaments and hence relays information on cell morphology. The cell nuclei were stained with DAPI (blue). In the

control experiments on smooth surfaces outside the structure of the substrates (Figure 2.5, top row), adhesion sites (vinculin) were randomly oriented, as was cell spreading (f-actin). On the dot patterns (Figure 2.5, middle row), adhesion sites were formed on the peaks of the topographies, which was evident from the dot patterning apparent in the vinculin-stained image. The cell morphology did not conform to the shape of the topography. On the 1200 nm spaced lines (Figure 2.5, bottom row), osteoblasts formed adhesions in parallel with the long axis of the topography (vinculin), and overall morphology (f-actin) was also aligned with the groove direction.

(a)   (b)
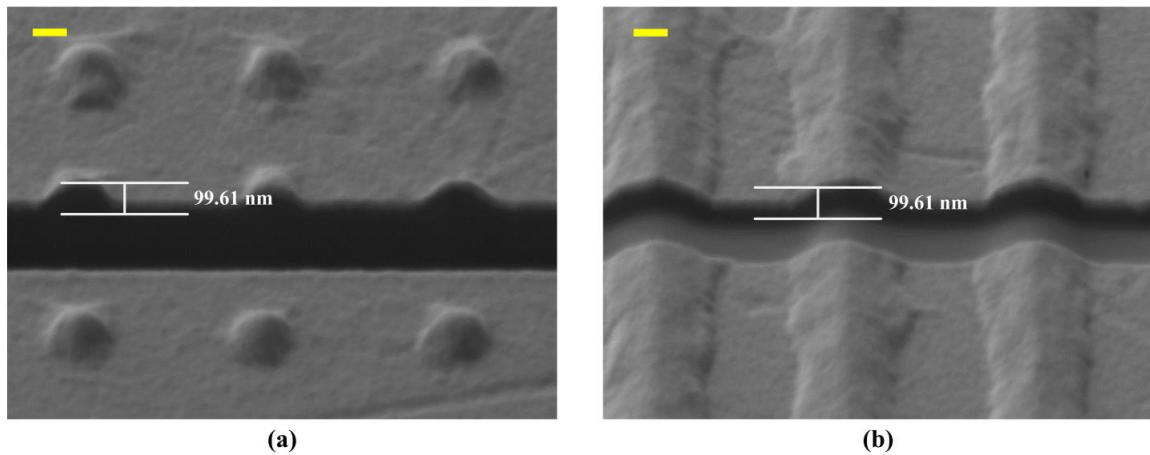
Figure 2.4. SEM images of dot (a) and line (b) patterns on ion-milled glass substrates coated with 30-nm thick gold for cell imaging experiments. These example samples were cut with focused ion beam to estimate the depth. Tilt corrected cursor height is ~100 nm excluding the gold coating. Scale bars represent 100 nm.
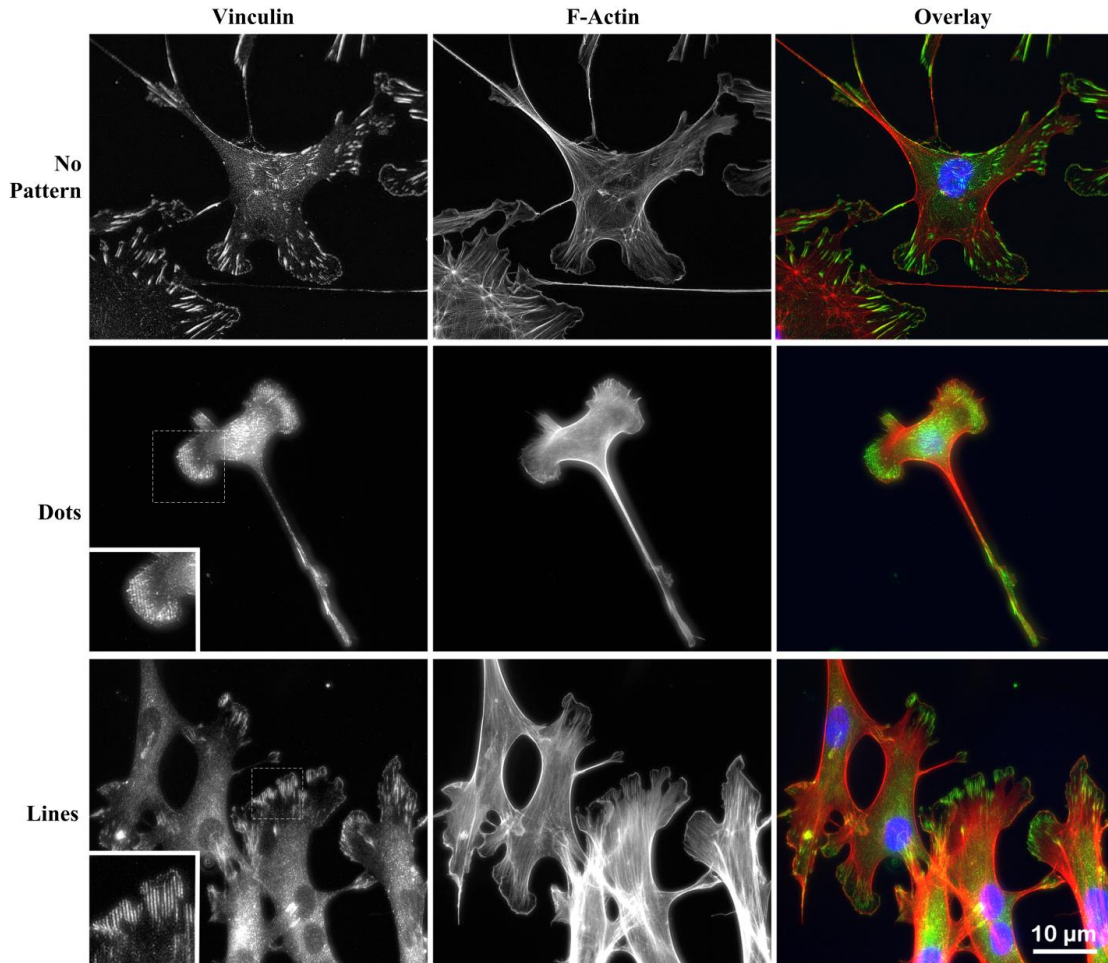
Figure 2.5. Rat calvarial osteoblasts cultured on smooth surfaces (top row), 1200 nm spaced nanodots (middle row) and 1200 nm spaced nanolines (bottom row). Adhesion sites were stained with vinculin (left column). Actin microfilaments were stained with f-actin (middle column). Overlay of the vinculin, f-actin and DAPI (nuclei) are depicted as green, red, and blue, respectively (right column). Insets show high resolution images of marked areas.

Without any extracellular cues (such as chemotaxis), osteoclasts in vitro will migrate at random in a non-directed manner. However, when placed on a substrate with a topographical pattern (such as the nanogrooves), the osteoclast migrates in a directed

manner following the orientation of the nanogrooves. Thus the osteoclast cells move along the groove direction. This has significant importance because osteoclasts are responsible for bone remodeling after injury such as fractures. Fractures create small fissures in the bone's topography (much like a nanogroove), so the nanogroove patterns and the manner in which osteoclasts migrate along them may provide insight into how osteoclasts move along fractures to help repair bone after injury.
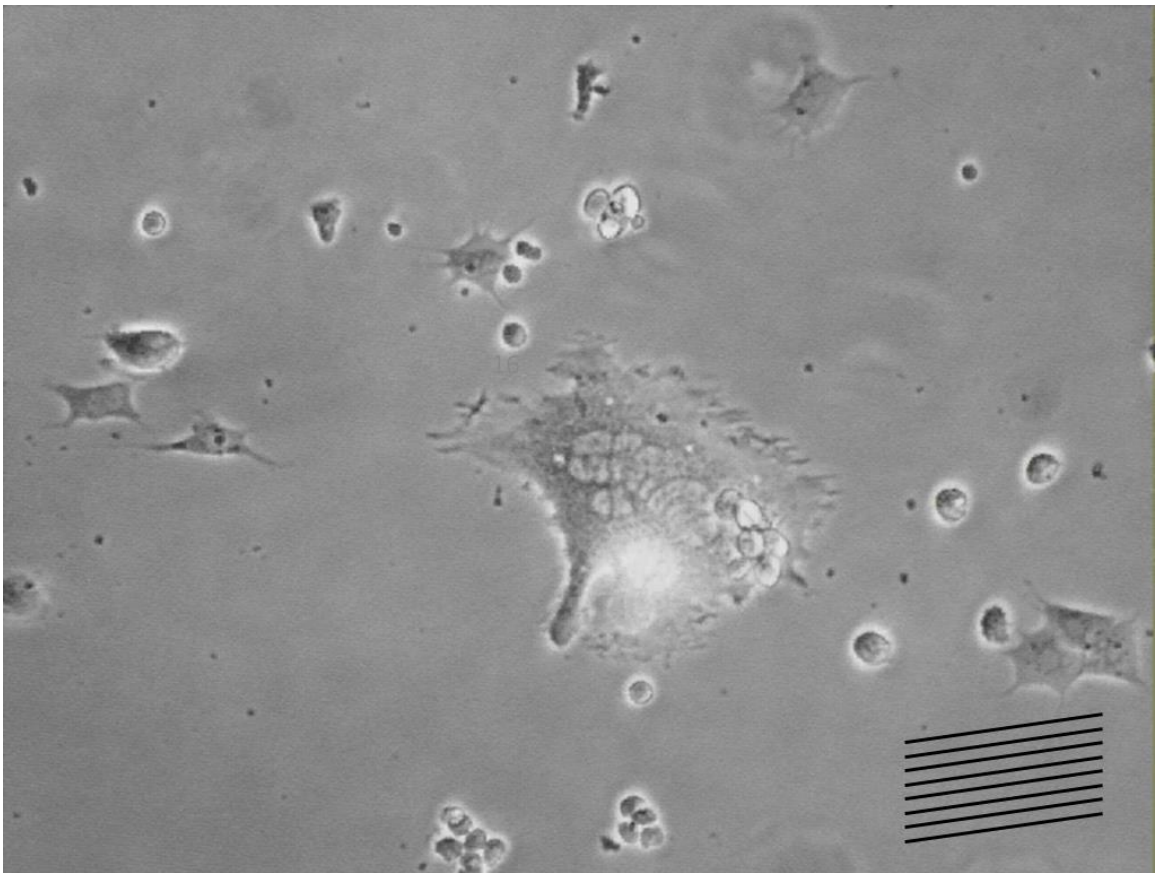
Figure 2.6. Primary rat calvarial osteoclasts cultured on nanogrooves with 1200 nm spaced nanolines (bottom row). Black lines show the nanogroove direction.

2.4   Discussion

Laser interference lithography is a straight-forward, flexible, and inexpensive method to create a variety of nanostructures. Utilizing Equation (2), experimental parameters can be selected to achieve a cumulative illumination pattern on the photoresist that leads to a wide range of patterns. We used a short distance between the pinhole and the substrate to create a high intensity gradient along the surface, which systematically yielded a variety of structures with morphologies, such as dots, holes, ellipses, lines, and transitions between morphologies. Changing the stage angle and the exposure time for two different exposure axes created structures with biaxial periodicities.

EBL and FIB provide a freedom to fabricate more arbitrary structures with finer features, however, they both require expensive setups and high operating costs; on the other hand creating large area structures, such as 15 mm x 15 mm as in our study, with EBL and FIB is also impractical in terms of the time required for the fabrication. Therefore LIL is a fast and inexpensive alternative to create systematically changing structures as well as periodic and biaxial structures.

Osteoblasts showed a differential response to 1200 nm spaced dots and lines, with qualitative changes in the arrangement and distribution of adhesions sites. In addition the cell morphology is strongly influenced by the form and orientation of the nanotopography. The relative importance on topographic regulation of focal adhesion size and stability in osteoblasts has received much attention. Biggs et al previously demonstrated that nanopits reduced the total cell area occupied by adhesion sites in osteoblasts [27] and that square and hexagonal nanopit arrays resulted in formation of

focal complexes [28]. Our results show that nanotopographies strongly influence the patterns of adhesion formation in osteoblasts.

All these structures can also be fabricated in thick and thin metal films placed on a planar substrate to obtain plasmonic structures [13][29][30]. The localized surface plasmon resonances (LSPR) of these metallic arrays are a function of material, size, shape, spacing and periodicity of the structures. The size and the spacing of the structures could be adjusted by fine tuning the exposure times and the exposure angle. Combined bimetallic nanostructure consisting of two different metal layers can provide additional tunability to the LSPR properties due to an interaction between two metallic layers [29]. Nanohole and nanodot arrays with biaxial periodicity provide intrinsically two different LSPR frequencies due to the possible choice of the probing polarization direction of the light. Meanwhile, there is a multitude of LSPR sensors and devices proposed, simulated and demonstrated implementing systematically or unsystematically above described parameters. A single chip carrying systematically changing nanostructures can help quickly to find the optimal nanostructure for the problem at hand to be solved with plasmonics. If an optical experiment is performed on elongated structures, the polarization of the probing light is exploited to detect the morphometric differences. The sharp linear features could act as an active substrate with hot spots in the case of a gold or silver nanostructure applied in SERS or fluorescence enhanced spectroscopy (FES).

Due to the geometrical limitations, the Lloyd's laser interferometer has limited surface coverage and for a wavelength of 442 nm the devices fabricated were limited to ~600 nm to ~1200 nm periodicity. One potential improvement is to make the angle between the mirror and the sample adjustable, which would add an extra degree of freedom and

extend the usable range of coverage and periodicity [14]. However, ultra-fine structures may require anti-reflective coatings to enhance optical performance [12]. In order to reach smaller periodicities, shorter wavelength lasers could be utilized. For example, extreme ultraviolet interference lithography (EUV-IL) has produced feature sizes to 10 nm [31].

We observed some non-uniformity within structures due to photoresist connections between adjacent features especially for sample 1 at locations $R_{(0,10)}$, $R_{(10,10)}$, and $R_{(10,0)}$. The non-uniformities could be treated with oxygen plasma after sample development, which would result in removal of the connections between adjacent nano-structures and individual features with a higher degree of uniformity.

Although structures created with LIL are limited to grooves, holes and dots, nanolithography employing micro-lens arrays has been shown capable of fabricating periodic arrays of arbitrary structures [32][33]. The technique utilizes an array of focal points from the laser beam that enables parallel patterning [33][34]. However, it requires micro-lens array fabrication prior to the fabrication of the intended nano-structures. Also, the periodicity of nanostructure array depends greatly on spacing between adjacent micro-lenses [33][34]. It is also shown that plasmonic nanolithography (PNL) can reach down to 12 nm feature size, by employing surface plasmons; however, that technique is also limited to periodic structures [35].

Surface topography features that systematically change in pattern have become an important tool to probe the limits of cell sensing, as well as to increase our understanding of how cells become activated [36]. Adhesion sites on cells are important for activation of downstream signaling cascades that are responsible for regulation of growth, survival,

migration, and differentiation [7][36]. By selecting the most appropriate topographies, it is conceivable that implants and tissue-engineered devices could be significantly improved. Moreover, from a basic science standpoint, devices fabricated with LIL may be particularly good to assess the response of primary cell cultures, where heterogeneity in growth and response to external stimuli, which is common place in human cells isolated from different patients, can complicate interpretation of results. Therefore, to be able to have one substrate with a variety of nanostructure pattern and their transitions allow comparison of cell responses to multiple cues at the same time.

2.5   Conclusion

Laser interference lithography is a powerful method to fabricate large area, periodic, biaxial periodic and systematically changing structures. In comparison with FIB and EBL, LIL is straightforward, quick and inexpensive. Cell culturing studies show that primary rat calvarial osteoblasts responding surface topographies that make us enable to control the cell behavior. It would be feasible to create plasmonic structures to have a different resonance conditions on a single substrate by the methods we discussed in this paper. The feature size is a function of the wavelength; therefore sources with smaller wavelength can be employed fabricate smaller periodicities. Some other techniques can be employed to overcome some of the limitations of LIL, such as limited coverage area, non-uniformities caused by residual photoresist. Having biaxial periodic and systematically changing structures on the same substrate allows studying various structures with a single substrate to decrease the sample size in order to find optimum topographies for certain cells to control their behavior. Using optimum nano structures on implant surfaces potentially improves the quality of the implants.

We assume that the periodicity and the depth of structures could provide different behaviors for cell adhesion to the substrate; therefore, as future work, the effect of the various structure depths and periodicities could be studied. Behavior of various cell types (e.g. stem cells) as well as their behavior on transitional nanostructures (in-between two structures, such as broken lines which is in-between lines and dots) should be investigated. Aside from topography, the surface chemistry can also be manipulated by various surface functionalization techniques, which opens up the possibility to study the combined effect of topography and the surface chemistry on cell adhesion. These directions of study should provide for a better understanding of implant surfaces with respect to growth and non-growth surfaces for particular cell types.

Acknowledgements

References

[1]   A. Akou, I. a. Gural'skiy, L. Salmon, C. Bartual-Murgui, C. Thibault, C. Vieu, G. Molnár, A. Bousseksou, *Journal of Materials Chemistry* **2012**, *22*, 3752.

[2]   A. Reinhard, T. Volz, M. Winger, *Nature ...* **2011**, *6*, 1.

[3]   C. Escobedo, A.G. Brolo, R. Gordon, D. Sinton, *Analytical Chemistry* **2010**, *82*, 10015.

[4]   S.M.H. Rafsanjani, T. Cheng, S. Mittler, C. Rangan, *Journal of Applied Physics* **2010**, *107*, 094303.

[5]   H. Jiang, T. Li, E. Ertorer, J. Yang, J. Sabarinathan, S. Mittler, *Sensors and Actuators A: Physical* **2013**, *189*, 474.

[6]   D.W. Hamilton, D.M. Brunette, *Experimental Cell Research* **2005**, *309*, 429.

[7]   D.W. Hamilton, D.M. Brunette, *Biomaterials* **2007**, *28*, 1806.

[8]   F. Kantawong, R. Burchmore, N. Gadegaard, R.O.C. Oreffo, M.J. Dalby, *Journal of the Royal Society, Interface / the Royal Society* **2009**, *6*, 1075.

[9]   E. Kokubu, D.W. Hamilton, T. Inoue, D.M. Brunette, *Journal of Biomedical Materials Research. Part A* **2009**, *91*, 663.

[10]   E. Lamers, J. Te Riet, M. Domanski, *Eur. Cell ...* **2012**, *23*, 182.

[11]   Q. Xie, M. Hong, H. Tan, G. Chen, L. Shi, T. Chong, *Journal of Alloys and Compounds* **2008**, *449*, 261.

[12]   H. Wolferen, L. Abelmann, in *Science*, Nova Publishers**2011**, 133.

[13]   J.W. Menezes, J. Ferreira, M.J.L. Santos, L. Cescato, A.G. Brolo, P. Photovoltaics, B.J.W. Menezes, *Advanced Functional Materials* **2010**, *20*, 3918.

[14]   I. Wathuthanthri, W. Mao, C.-H. Choi, *Optics Letters* **2011**, *36*, 1593.

[15]   T.P. Kunzler, C. Huwiler, T. Drobek, J. Vörös, N.D. Spencer, *Biomaterials* **2007**, *28*, 5000.

[16]   Y.L. Khung, G. Barritt, N.H. Voelcker, *Experimental Cell Research* **2008**, *314*, 789.

[17]   D. Hamilton, C. Oates, A. Hasanzadeh, S. Mittler, *PLoS One* **2010**, *5*, e15129.

[18]   T.P. Kunzler, T. Drobek, M. Schuler, N.D. Spencer, *Biomaterials* **2007**, *28*, 2175.

[19]   K.L. Kelly, E. Coronado, L.L.L. Zhao, G.C. Schatz, *The Journal of Physical Chemistry B* **2002**, *107*, 668.

[20]   Y. Xia, N.J. Halas, G. Editors, *MRS Bulletin* **2005**, *30*, 644.

[21]   P.K. Jain, K.S. Lee, I.H. El-Sayed, M. a El-Sayed, *The Journal of Physical Chemistry. B* **2006**, *110*, 7238.

[22]   P. Rooney, A. Rezaee, S. Xu, T. Manifar, A. Hassanzadeh, G. Podoprygorina, V. Böhmer, C. Rangan, S. Mittler, *Physical Review B* **2008**, *77*, 1.

[23]   Q. Min, Y. Pang, D.J. Collins, N. a Kuklev, K. Gottselig, D.W. Steuerman, R. Gordon, *Optics Express* **2011**, *19*, 1648.

[24] F. Eftekhari, R. Gordon, J. Ferreira, a. G. Brolo, D. Sinton, *Applied Physics Letters* **2008**, *92*, 253103.

[25] I. Byun, J. Kim, *Journal of Micromechanics and Microengineering* **2010**, *20*, 055024.

[26] R.J. Miron, C.J. Oates, A. Molenberg, M. Dard, D.W. Hamilton, *Biomaterials* **2010**, *31*, 449.

[27] M.J.P. Biggs, R.G. Richards, N. Gadegaard, C.D.W. Wilkinson, M.J. Dalby, *Journal of Materials Science. Materials in Medicine* **2007**, *18*, 399.

[28] M.J.P. Biggs, R.G. Richards, N. Gadegaard, C.D.W. Wilkinson, R.O.C. Oreffo, M.J. Dalby, *Biomaterials* **2009**, *30*, 5094.

[29] C.H. Liu, M.H. Hong, H.W. Cheung, F. Zhang, Z.Q. Huang, L.S. Tan, T.S. a Hor, *Optics Express* **2008**, *16*, 10701.

[30] D. Xia, *Nano Letters* **2004**, 1.

[31] V. Auzelyte, C. Dais, P. Farquet, D. Grützmacher, L.J. Heyderman, F. Luo, S. Olliges, C. Padeste, P.K. Sahoo, T. Thomson, A. Turchanin, C. David, H.H. Solak, *Journal of Micro/Nanolithography, MEMS and MOEMS* **2009**, *8*, 021204.

[32] J. Kato, N. Takeyasu, Y. Adachi, H.-B. Sun, S. Kawata, *Applied Physics Letters* **2005**, *86*, 044102.

[33] Y. Lin, M.H. Hong, T.C. Chong, C.S. Lim, G.X. Chen, L.S. Tan, Z.B. Wang, L.P. Shi, *Applied Physics Letters* **2006**, *89*, 041108.

[34] C.S. Lim, M.H. Hong, Y. Lin, Q. Xie, B.S. Luk'yanchuk, A. Senthil Kumar, M. Rahman, *Applied Physics Letters* **2006**, *89*, 191125.

[35] H. Liu, J. Teng, *Journal of Molecular and Engineering Materials* **2012**, *01*, 1250005.

[36] J.Y. Lim, H.J. Donahue, *Tissue Engineering* **2007**, *13*, 1879.

Chapter 3

Fabrication of Gold Nanodisk Arrays by Laser Interference

Lithography and Their Plasmonic Response[2]

3.1 Introduction

Metallic nanostructures have a variety of applications such as biosensing [1], [2], photovoltaics [3], [4], and chemical sensing [5], [6]. Localized surface plasmon resonance (LSPR) is a condition under which the resonance frequency of the electron charge density oscillation matches the frequency of the incoming field. This resonance condition for a metallic nanostructure is a function of the shape, size, interparticle distance, and composition of the material as well as the surrounding medium [7−12]. Numerous studies have reported taking advantage of these properties in different

---

[2] A version of this chapter is in preparation for publication. Erden Ertorer, Mohamadreza Najiminaini, Hao Jiang, Silvia Mittler, "Fabricating gold nanodisk arrays by laser interference lithography and their plasmonic response".

applications [13–16]. Transmission sensors [17] and surface enhanced Raman spectroscopy are the most common examples of LSPR based biosensing applications.

Focused ion beam (FIB) and electron beam lithography (EBL) are the most common fabrication methods for producing metallic nanostructures [18–20]. Despite their precision and ability to create arbitrary structures, their low speed and high operating costs make EBL and FIB unsuitable for mass production and along larger surfaces.

Low-cost fabrication methods are required for industrial, medical and clinical applications. Nanoimprint lithography, [21], [22] nanosphere lithography [23], [24], microlens array lithography [25], [26], and laser interference lithography (LIL) [27], [28] are examples of low-cost alternatives for fabricating periodic nanostructures over large surfaces.

LIL studies have mostly focused on creating quantum dots of semiconductor materials [29], [30] and nanowires [30], [31]; only a few have focused on metallic nanoparticles [8], [17], [21].

Gold nanoparticles show several advantages over other metallic nanoparticles: its biosensor coupling chemistries are well studied, its plasmon resonance frequency is easily detected by standard Vis-IR spectroscopy, and in contrast to silver, gold does not oxidize [17].

In this study, we investigated the feasibility of LIL for creating gold nanodisk arrays for plasmonic sensing applications. Fabrication details are provided, bulk sensitivity

measurements were performed, and the results were compared with finite difference time domain (FDTD) simulations.

3.2 Methods

3.2.1 Fabrication

We used LIL to fabricate a template for the gold nanodisk array structure. Details of the Lloyd interferometer for the LIL are described elsewhere [27]. In short, a HeCd laser at λ = 442 nm (Omnichrome Series 74, Model 4074-P-A03, CVI Melles Griot, Albuquerque, NM, USA) was operated at 80 mW. The laser beam passed through a lens-pinhole system built with a $20\times$ objective lens (Zeiss LD Plan-Neofluar $20\times$/0.4 Corr Ph2, Zeiss Inc, Thornwood, NY), and a 5-µm pinhole mounted on a three-axis stage (Newport Three-Axis Spatial Filter, Model M-900, Newport, CA, USA). The distance between the pinhole and the sample holder was adjusted to 40 cm in order to use the top of the Gaussian field distribution to obtain a relatively uniform exposure over the sample.

Figure 3.1 illustrates the fabrication procedure; 8 mm $\times$ 12 mm BK7 glass slides were rinsed with acetone, deionized water and isopropanol, then dried under a flow of nitrogen. For further drying, the samples were left on a hot plate at 115°C for 5 minutes. Samples were spin-coated with LOR5a lift-off resist (MicroChem, Newton, MA, USA), diluted 1:2 with Microposit Thinner Type P (Shipley Co., Marlborough, MA, USA) at 6000 rpm and baked at 185°C for ten minutes. Samples were left to cool for five minutes and then S1805 photoresist (MicroChem, Newton, MA, USA) was spin-coated on top at

6000 rpm, followed by soft baking at 115°C for five minutes to evaporate the solvent within the photoresist.

In order to create a gold nanodisk array with a lift-off procedure, a negative image of the disk array pattern; which is a nano-hole array, was created. LIL by Lloyd's interference setup was employed to create these structures. The samples were exposed for 18 seconds at a stage angle of 16°, which corresponds to ~900 nm periodicity, followed by another 18 second exposure after rotating the samples 90° to yield a grid pattern. Microposit MF319 developer (Shipley Co., Marlborough, MA, USA) was used for 43 seconds to develop the samples.

Samples were placed in a custom electron-beam deposition device (Hoser) at the University of Western Ontario Nanofabrication Facility to deposit 3 nm of titanium as an adhesive layer and then 30 nm of gold. For the lift-off process, samples were immersed in Remover PG (MicroChem) and agitated ultrasonically for ten seconds to remove the metallic layer, which is not directly attached to the glass surface.
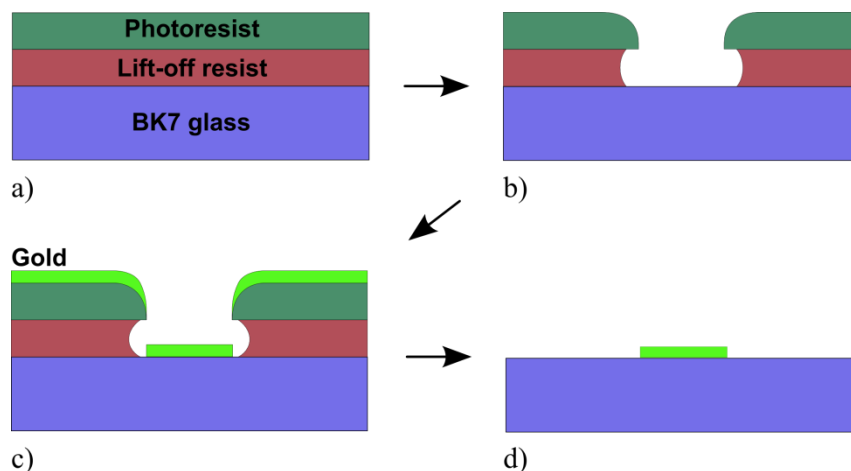
Figure 3.1. Illustration of the fabrication procedure; a) BK7 substrate coated with lift-off resist and photoresist layers, b) nanohole pattern with undercut profile after laser exposure and development, c) e-beam gold deposition, d) nanodisk remaining after lift-off.

3.2.2 Bulk refractive index studies

A Shimadzu UV-3600 UV-Vis-NIR Spectrophotometer (Shimadzu Corp., Kyoto, Japan) was used to measure absorption of the samples. In order to test bulk SPR sensitivity of each nanostructure, we immersed each sample in cuvettes filled with various solvents: ethanol, water, acetone and isopropanol. We used a Zeiss refractometer (Zeiss, Oberkochen, Germany) to validate the refractive index of these solvents. While measuring the absorption, another cuvette containing BK7 substrate as a blank, filled with the same solvent used for the sample, was placed in the reference beam

compartment of the spectrometer to correct for the absorption of the solvent, glass and cuvette.

3.2.3 Numerical modeling

In order to clarify the SPR modes of gold nanodisks, calculations were performed using the three-dimensional FDTD method [32], [33]. FDTD is a numerical approach for solving two- and three-dimensional Maxwell's equations in linear and nonlinear dispersive media. The FDTD method makes it possible to calculate numerical solutions for arbitrary geometric structures and various input excitation sources. Since absorption and permittivity for a metallic material are functions of the frequency of the source, the dispersion properties of the metal were considered. Palik's [34] dielectric constants were used for the metal layers in the particles.

We used a commercial FDTD package from Lumerical Inc. (Vancouver, Canada) to simulate the absorption properties of the nanodisk structures. We simulated a nanodisk array structure with 900 nm periodicity, a 550 nm diameter and a 30 nm thickness. A 4-nm sized non-uniform mesh was employed. A plane wave light source was used to illuminate the nanodisk array structure at normal incidence to the plane of the substrate. Three monitors were used for monitoring the field distribution and transmission properties. A far-field monitor was placed 650 nm above the disks. Another monitor for the near field was placed 6 nm above the disks. In order to obtain cross-sectional field distributions of the gold nanodisks, a third monitor was placed on the perpendicular to the disk (Figure 3.2).
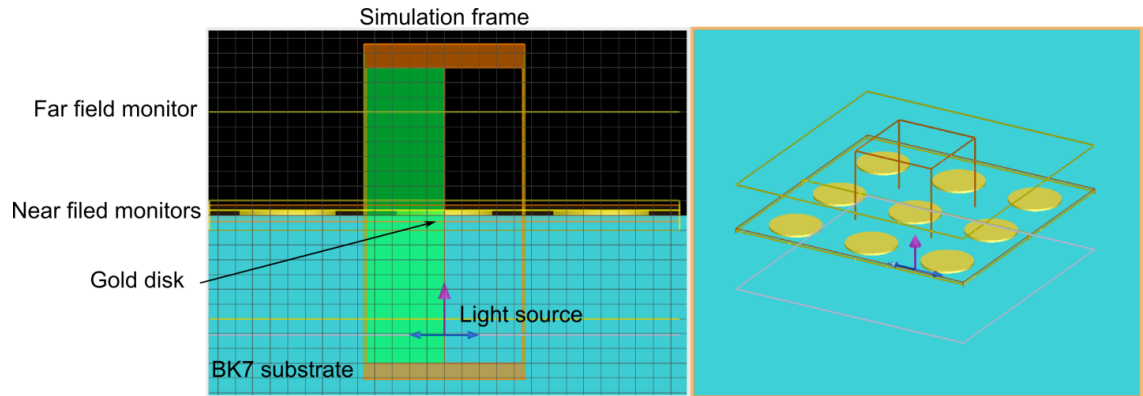
Figure 3.2. Model structure and placement of the monitors used in Lumerical software for calculating FDTD numerical solutions. Disk diameter is 550 nm, thickness is 30 nm and the periodicity is 900 nm.

3.3 Results

Figure 3.3 shows a scanning electron microscope (SEM) image of the mask structure used to fabricate gold nanodisk arrays. The overall structure was uniform throughout the substrate except for some local structural defects and edge effects due to the spin-coating process. Higher magnification images show the hole structures. Holes were not perfectly circular and their diameter showed some variance, which is reflected to the disc diameter and qualitatively analyzed from the SEM images of the disks.
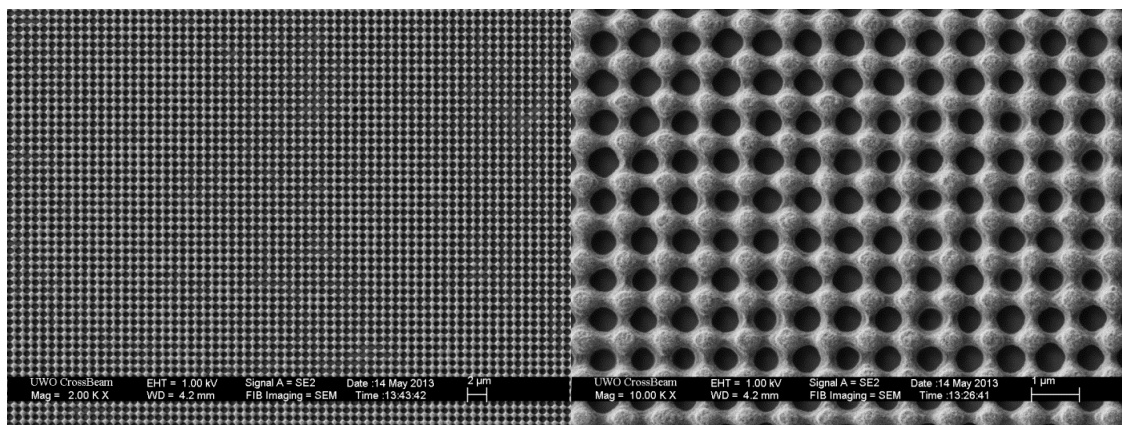
Figure 3.3. Nanohole array pattern on glass made of the photoresist after development, shown at two magnifications. Left image shows the uniformity at large scale, right image shows the details of the holes.

Figure 3.4 shows an image of a tilted nanohole structure. The etching rate of the LOR5a lift-off resist layer was adjusted by varying baking temperature and time. When the photoresist layer was etched through the lift-off resist, the lift-off resist etched at a higher rate than the photoresist, which created an undercut structure in the lift-off resist (Figure 3.4). The etching rate is crucial for creating an undercut structure, since at higher etching rates, the lift-off resist will completely dissolve, causing detachment of the photoresist from the substrate. On the other hand, if the etching rate is low, the lift-off resist will not dissolve down to the substrate and will block the nanoholes; evaporated gold will not adhere to the glass surface. The thickness of the lift-off resist was measured with a SEM to be around 120 nm.
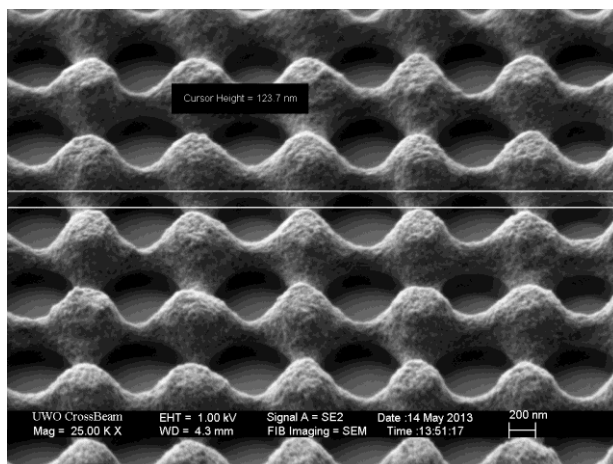
Figure 3.4. Tilted image of a nanohole array shows the undercut structure.

Sonicating the structure in Remover PG dissolved the lift-off resist and the photoresist layers; therefore, the gold film layer on the photoresist was removed, too. The gold on the glass remained, creating a two-dimensional nanodisk array structure, as seen in Figure 3.5. Structural defects and nonuniformities in the photoresist template caused some particles to merge. In addition to these nonuniformities, variation in disk size was observed. The average disk diameter, measured from SEM images, was 552 ± 51 nm and circularity was 0.976 ± 0.007
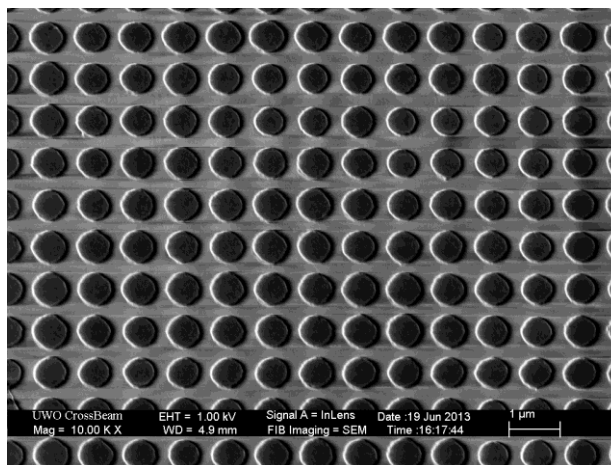
Figure 3.5. SEM image of gold nanodisk structures on a glass substrate.

Figure 3.6 shows the experimental and simulated absorption spectra of a representative nanodisk array sample. The largest absorption peak at ~1500 nm corresponds to the dipole mode of the gold nanodisk, as seen in Figure 3.7. Simulation result reflects mono-dispersed 550 nm diameter disk arrays. In terms of the peak position and the shape, simulation result was in good agreement with the experimental results. However, experimental data shows a larger bandwidth due to contributions from different sizes of nanodisks.
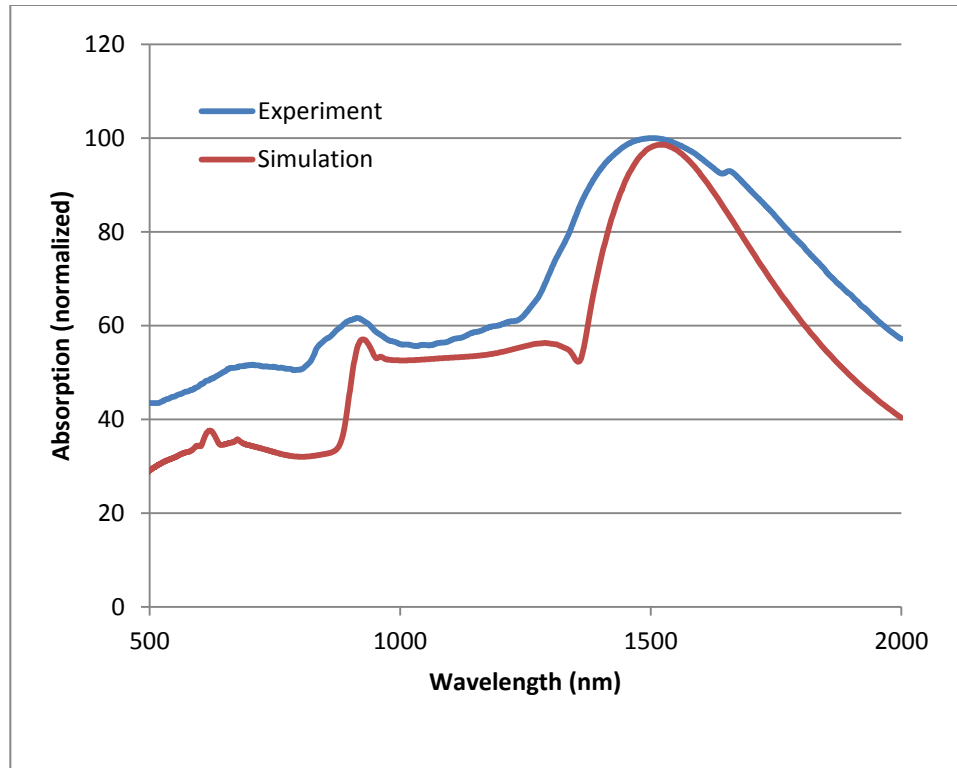
Figure 3.6. Simulated and experimental absorption data for a gold nanodisk array
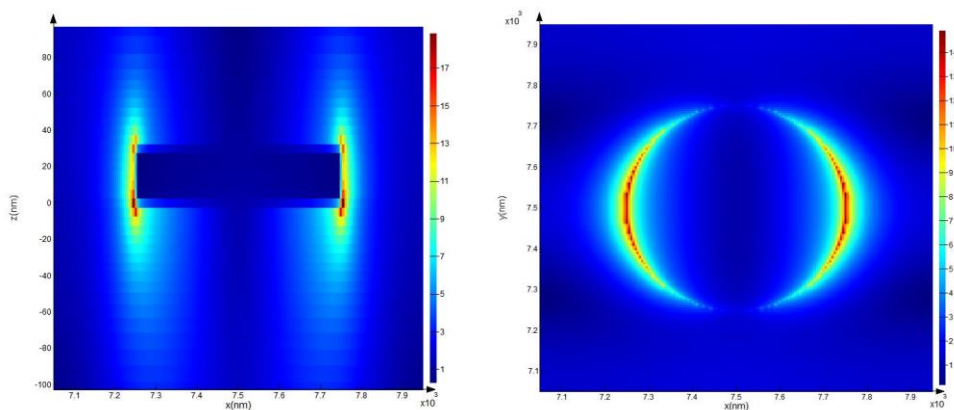
sample.

Figure 3.7. Dipole excitation mode of a 550 nm gold nanodisk; left image shows side view and right image shows top view.

For bulk sensing experiments, samples were immersed in various solvents. The maximum of the dipole peak in the absorption spectrum was red-shifted by the increased refractive index of the solvent. Figure 3.8 shows a linear relationship between the spectral position of the LSPR and the refractive index. Based on the experimental results, the figure of merit of the sensor was calculated as ~975 nm/RIU.
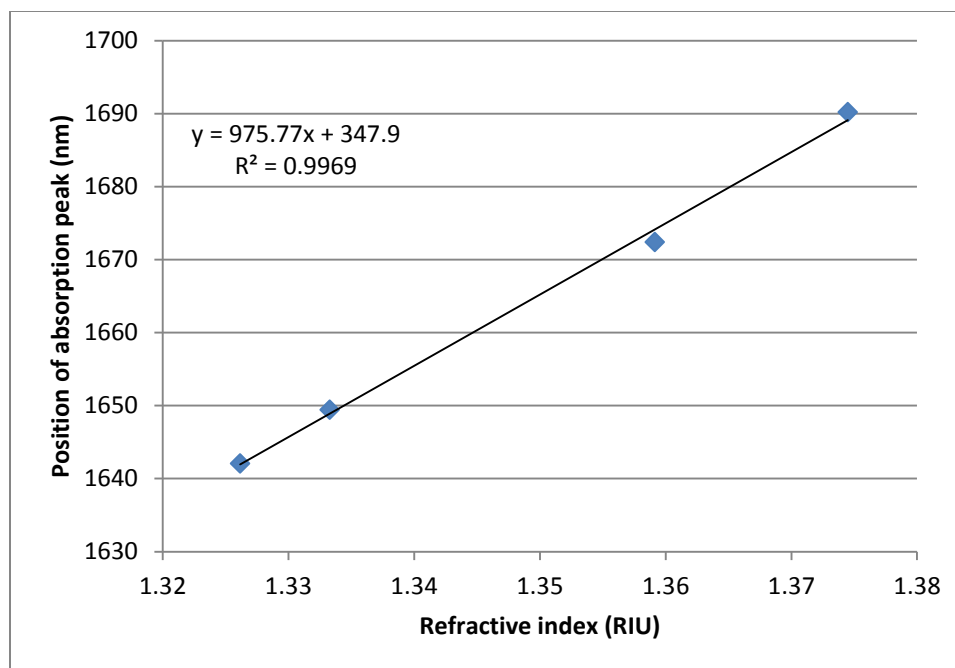
Figure 3.8. Bulk refractive index measurement of the gold nanodisk array sample.

3.4 Discussion

LIL in combination with the lift-off technique can be used to fabricate gold nanodisk arrays for applications where the uniformity of disk size is not crucial. Despite imperfections in shape and pattern of samples fabricated by LIL, it would be more feasible to use LIL, owing to its low cost and simplicity in comparison with other conventional methods, such as EBL and FIB. Periodicity and the size of the structure can be tuned by adjusting the stage angle of the Lloyd's mirror. However, feature size is not only a function of the wavelength; S1805 photoresist layers show some proximity effects at lower periodicities (below 700 nm), which causes some defects in the structure. A

combination of more precise photoresists and lower wavelength lasers can be used to eliminate these problems when fabricating smaller features.

Another alternative to the lift-off technique could be wet etching. LIL can be applied to gold-coated glass samples to create a nanodot array structure made of photoresist. Wet etching with aqua regia can selectively remove the gold to keep gold nanodisks under the nanodot structure. However, due to the polycrystalline structure and the high etching rate of gold, this fabrication process is difficult at the submicron regime. Gold etching with aqua regia happens very quickly and continues under the photoresist until it is rinsed away thoroughly. Etching tends to follow the polycrystalline grain structure of the surface, leaving domains with rough, granular edges. These factors should be considered when developing a wet-etching based protocol. However, different metals that have low etching rates, such as chromium, can be used with wet-etching technology.

Numerical simulation of the absorption spectrum of the disks shows a distinct peak that corresponds to the dipole mode. [35] The experimental results are in agreement with the simulation; possible defects in the structures such as merged particles and nonuniformity of the size distribution may be reasons for the wider bandwidth. The simulation was performed for an array of 550 nm diameter particles with a thickness of 30 nm and a periodicity of 900 nm. When necessary, an improved approach for the simulation would take into account the size variations and merged particles.

The bulk sensitivity of the gold nanodisk array was found to be ~975 nm/RIU, a high value in comparison to literature values from similar structures. Gold nanodisk arrays fabricated with nanoimprint lithography showed a sensitivity of 327 nm/RIU [21];

however, the particle diameter was around 100 nm. On the other hand, for biosensing applications, bulk sensitivity should be considered with the measurement errors in order to calculate the sensitivity and the limit of detection of the sensor for the specific linking chemistry [13], [36].

In order to create a uniform pattern across larger areas, the intensity of the "writing" light should be uniform along the surface. Intrinsically the laser has a Gaussian beam profile; however, with proper adjustment in the optical setup, selecting only the top of the Gaussian beam profile helps to decrease intensity variations over the substrate. On the other hand, adjustment of the pinhole is critical to obtain a uniform intensity distribution. A well-adjusted pinhole removes the undesired components of the laser beam, whereas alignment problems may modulate the intensity distribution. Figure 3.7 is an SEM image of a disk array fabricated with a poorly aligned pinhole, introducing grating ghosts.
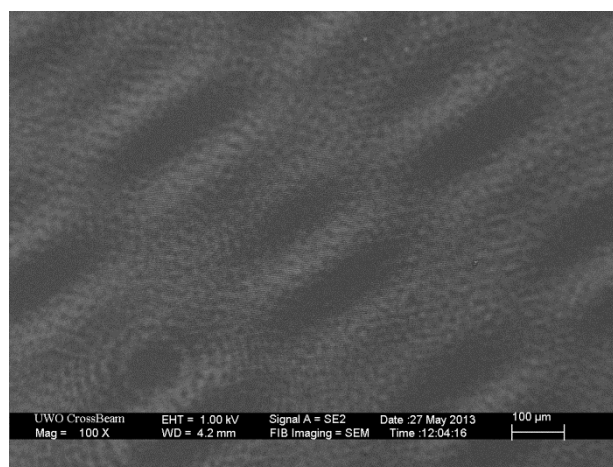
Figure 3.9. A modulation pattern known as grating ghosts in the nanodisk structure caused by a poorly adjusted pinhole.

The undercut profile in the lift-off resist is key for a successful lift-off process. Figure 3.10 shows a photoresist structure without a lift-off resist. As a result of the continuous sinusoidal shape of the pattern, the entire layer is connected and lift-off attempts fail (Figure 3.11).
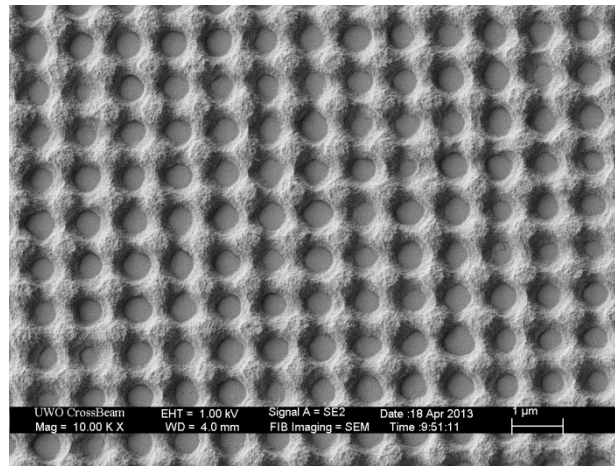
Figure 3.10. A 30 nm gold-coated photoresist structure in the absence of a lift-off resist layer.
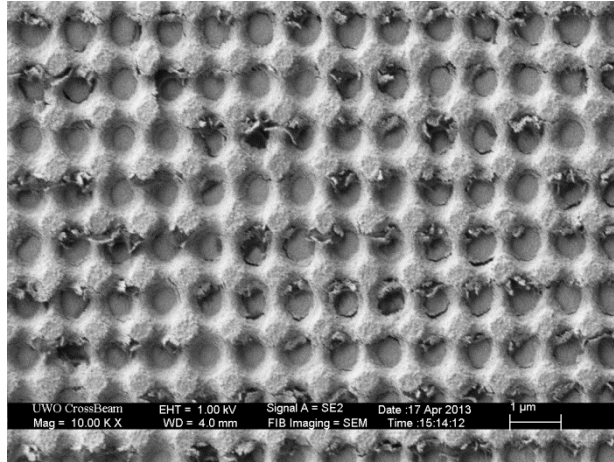
Figure 3.11. Failed sample; lift-off does not work without an undercut profile, and the gold cannot be removed because it is connected to the glass substrate.

When the etching rate of the lift-off resist is not adjusted properly, either the photoresist structure washes away during the development process, or it does not develop properly and covers the glass surface, after which lift-off removes the desired nanodisk array as well as the resist layer (Figure 3.12).
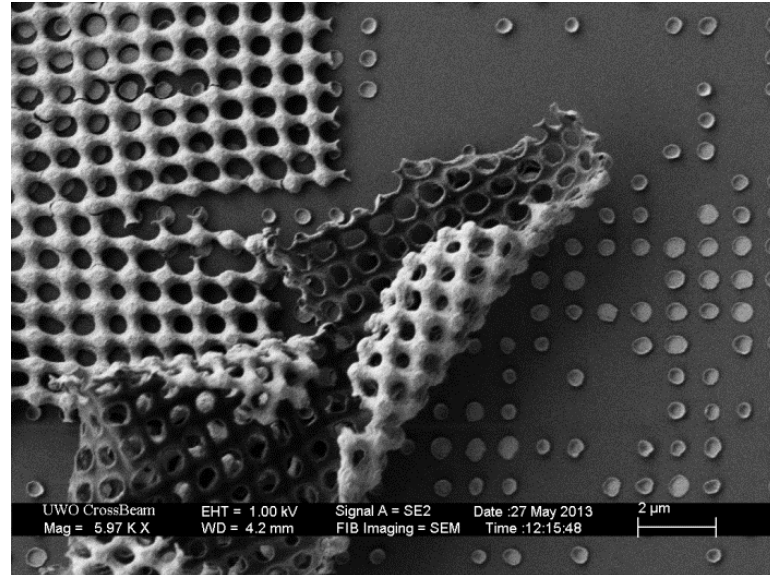
Figure 3.12. Failed structures; if the lift-off resist is not etched down to the glass, gold disks form on top of the lift-off resist, and the lift-off process removes the entire structure.

3.5 Conclusion

In this study, we presented a straightforward and inexpensive method to fabricate gold nanodisk arrays with LIL in combination with a lift-off technique. LIL is used to create a photoresist template for the disk structure. The undercut profile required for the lift-off process was created by a thin film of a lift-off resist. With metal deposition by e-beam evaporation and the successive lift-off processes, we created gold nanodisk arrays on BK7 substrates. Good overall homogeneity was achieved with minor size and shape non-uniformities. FDTD numerical simulation was employed to interpret the plasmonic properties of the structure. Numerical simulation results were in agreement with the experimental results. Bulk sensitivity was measured as ~975 nm/RIU, indicating that these LIL fabricated gold nanoparticle arrays are suitable for developing plasmonic

sensors. Protein sensing experiments should be performed to evaluate the biosensing properties of LIL fabricated gold nanodisk arrays.

Acknowledgements

References

[1] H. Jiang, T. Manifar, A. Bakhtazad, H. Hojjati, J. Sabarinathan, and S. Mittler, "Periodic arrays of gold nano-disks coupled with evanescent spectroscopy," *Journal of Applied Physics*, vol. 113, no. 22, p. 224306, 2013.

[2] C. Escobedo, Y. Chou, M. Rahman, and X. Duan, "Quantification of ovarian cancer markers with integrated microfluidic concentration gradient and imaging nanohole surface plasmon resonance," *Analyst*, 2013.

[3] J. W. Menezes, J. Ferreira, M. J. L. Santos, L. Cescato, A. G. Brolo, P. Photovoltaics, and B. J. W. Menezes, "Large-Area Fabrication of Periodic Arrays of Nanoholes in Metal Films and Their Application in Biosensing and Plasmonic-Enhanced Photovoltaics," *Advanced Functional Materials*, vol. 20, no. 22, pp. 3918–3924, Nov. 2010.

[4] J. H. Lee, J. H. Park, J. S. Kim, D. Y. Lee, and K. Cho, "High efficiency polymer solar cells with wet deposited plasmonic gold nanodots," *Organic Electronics*, vol. 10, no. 3, pp. 416–420, May 2009.

[5] N. Nagraj, J. M. Slocik, D. M. Phillips, N. Kelley-Loughnane, R. R. Naik, and R. a Potyrailo, "Selective sensing of vapors of similar dielectric constants using peptide-capped gold nanoparticles on individual multivariable transducers.," *The Analyst*, vol. 138, no. 15, pp. 4334–9, Aug. 2013.

[6] A. B. Dahlin, B. Dielacher, P. Rajendran, K. Sugihara, T. Sannomiya, M. Zenobi-Wong, and J. Vörös, "Electrochemical plasmonic sensors.," *Analytical and bioanalytical chemistry*, vol. 402, no. 5, pp. 1773–84, Feb. 2012.

[7] M. Najiminaini, F. Vasefi, B. Kaminska, and J. J. L. Carson, "A Three-Dimensional Plasmonic Nanostructure with Extraordinary Optical Transmission," *Plasmonics*, vol. 8, no. 2, pp. 217–224, Jul. 2012.

[8] C. H. Liu, M. H. Hong, H. W. Cheung, F. Zhang, Z. Q. Huang, L. S. Tan, and T. S. a Hor, "Bimetallic structure fabricated by laser interference lithography for tuning

surface plasmon resonance.," *Optics express*, vol. 16, no. 14, pp. 10701–9, Jul. 2008.

[9] K.-H. Su, Q.-H. Wei, X. Zhang, J. J. Mock, D. R. Smith, and S. Schultz, "Interparticle coupling effects on plasmon resonances of nanogold particles," *Nano Letters*, vol. 3, no. 8, pp. 1087–1090, Aug. 2003.

[10] S. M. H. Rafsanjani, T. Cheng, S. Mittler, and C. Rangan, "Theoretical proposal for a biosensing approach based on a linear array of immobilized gold nanoparticles," *Journal of Applied Physics*, vol. 107, no. 9, p. 094303, 2010.

[11] C. Noguez, "Surface plasmons on metal nanoparticles: the influence of shape and physical environment," *The Journal of Physical Chemistry C*, vol. 111, no. 10, pp. 3806–3819, Mar. 2007.

[12] a. Unger, M. Kreiter, and D. N. Chigrin, "Analyzing the Performance of Plasmonic Resonators for Dielectric Sensing," *AIP Conference Proceedings*, no. 2, pp. 160–162, 2009.

[13] H. Jiang, T. Li, E. Ertorer, J. Yang, J. Sabarinathan, and S. Mittler, "A biosensor based on periodic arrays of gold nanodisks under normal transmission," *Sensors and Actuators A: Physical*, vol. 189, no. 0, pp. 474–480, Jan. 2013.

[14] H. Jiang, S. Member, J. Sabarinathan, T. Manifar, and S. Mittler, "3-D FDTD Analysis of Gold-Nanoparticle-Based Photonic Crystal on Slab Waveguide," vol. 27, no. 13, pp. 2264–2270, 2009.

[15] M. Najiminaini, F. Vasefi, B. Kaminska, and J. J. L. Carson, "Optical resonance transmission properties of nano-hole arrays in a gold film: effect of adhesion layer.," *Optics express*, vol. 19, no. 27, pp. 26186–97, Dec. 2011.

[16] F. Vasefi, M. Najiminaini, B. Kaminska, and J. J. L. Carson, "Effect of surface plasmon cross-talk on optical properties of closely packed nano-hole arrays.," *Optics express*, vol. 19, no. 25, pp. 25773–9, Dec. 2011.

[17]   R. Gordon, A. G. Brolo, D. Sinton, and K. L. Kavanagh, "Resonant optical transmission through hole-arrays in metal films: physics and applications," *Laser & Photonics Reviews*, vol. 4, no. 2, pp. 311–335, May 2009.

[18]   M. Najiminaini, F. Vasefi, B. Kaminska, and J. J. L. Carson, "Experimental and numerical analysis on the optical resonance transmission properties of nano-hole arrays.," *Optics express*, vol. 18, no. 21, pp. 22255–70, Oct. 2010.

[19]   M. Najiminaini, F. Vasefi, B. Kaminska, and J. J. L. Carson, "Nano-hole array structure with improved surface plasmon energy matching characteristics," *Applied Physics Letters*, vol. 100, no. 4, p. 043105, 2012.

[20]   M. Fan, G. F. S. Andrade, and A. G. Brolo, "A review on the fabrication of substrates for surface enhanced Raman spectroscopy and their applications in analytical chemistry.," *Analytica chimica acta*, vol. 693, no. 1–2, pp. 7–25, May 2011.

[21]   S. Lee, K. Lee, J. Ahn, J. Lee, M. Kim, and Y. Shin, "Highly sensitive biosensing using arrays of plasmonic Au nanodisks realized by nanoimprint lithography," *ACS nano*, no. 2, pp. 897–904, 2011.

[22]   L. Wang, H. H. Solak, and Y. Ekinci, "Fabrication of high-resolution large-area patterns using EUV interference lithography in a scan-exposure mode.," *Nanotechnology*, vol. 23, no. 30, p. 305303, Aug. 2012.

[23]   Y. Wang, S. Han, A. L. Briseno, R. J. G. Sanedrin, and F. Zhou, "A modified nanosphere lithography for the fabrication of aminosilane/polystyrene nanoring arrays and the subsequent attachment of gold or DNA-capped gold nanoparticles," *Journal of Materials Chemistry*, vol. 14, no. 24, p. 3488, 2004.

[24]   S. Zhu and Y. Fu, "Fabrication and characterization of nanostructured metallic arrays with multi-shapes in monolayer and bilayer," *Journal of Nanoparticle Research*, vol. 12, no. 5, pp. 1829–1835, Aug. 2009.

[25]   C. S. Lim, M. H. Hong, Y. Lin, L. S. Tan, a. S. Kumar, and M. Rahman, "Large Area Parallel Surface Nanostructuring With Laser Irradiation Through Microlens Arrays," *Surface Review and Letters*, vol. 17, no. 03, pp. 383–387, Jun. 2010.

[26]   C. S. Lim, M. H. Hong, Y. Lin, Q. Xie, B. S. Luk'yanchuk, A. Senthil Kumar, and M. Rahman, "Microlens array fabrication by laser interference lithography for super-resolution surface nanopatterning," *Applied Physics Letters*, vol. 89, no. 19, p. 191125, 2006.

[27]   E. Ertorer, F. Vasefi, J. Keshwah, M. Najiminaini, C. Halfpap, U. Langbein, J. J. L. Carson, D. W. Hamilton, and S. Mittler, "Large area periodic, systematically changing, multishape nanostructures by laser interference lithography and cell response to these topographies.," *Journal of biomedical optics*, vol. 18, no. 3, p. 35002, Mar. 2013.

[28]   H. Wolferen and L. Abelmann, "Laser Interference Lithography," in *Science*, Nova Publishers, 2011, pp. 133–148.

[29]   K. Petter, T. Kipp, C. Heyn, D. Heitmann, and C. Schüller, "Fabrication of large periodic arrays of AlGaAs microdisks by laser-interference lithography and selective etching," *Applied Physics Letters*, vol. 81, no. 4, pp. 592–594, 2002.

[30]   W. K. Choi, T. H. Liew, M. K. Dawood, H. I. Smith, C. V Thompson, and M. H. Hong, "Synthesis of silicon nanowires and nanofin arrays using interference lithography and catalytic etching.," *Nano letters*, vol. 8, no. 11, pp. 3799–802, Nov. 2008.

[31]   D. S. Kim, R. Ji, H. J. Fan, F. Bertram, R. Scholz, A. Dadgar, K. Nielsch, A. Krost, J. Christen, U. Gösele, and M. Zacharias, "Laser-interference lithography tailored for highly symmetrically arranged ZnO nanowire arrays.," *Small (Weinheim an der Bergstrasse, Germany)*, vol. 3, no. 1, pp. 76–80, Jan. 2007.

[32] K. Yee, "Numerical solution of initial boundary value problems involving Maxwell's equations in isotropic media," *Antennas and Propagation, IEEE Transactions on*, 1966.

[33] A. Tavlove and S. Hagness, *Computational electrodynamics: the finite-difference time-domain method*. 1995.

[34] E. Palik, *Handbook of Optical Constants of Solids: Index*, no. 225. Academic Press Inc., 1998, pp. 525–533.

[35] J. Z. Zhang and C. Noguez, "Plasmonic Optical Properties and Applications of Metal Nanostructures," *Plasmonics*, vol. 3, no. 4, pp. 127–150, Sep. 2008.

[36] E. Ertorer, J. C. Avery, L. C. Pavelka, and S. Mittler, "Surface Immobilized Gold Nanoparticles by Organometallic Chemical Vapor Deposition on Amine Terminated Glass Surfaces," Accepted manuscript to *Chemical Vapor Deposition*, 2013.

Chapter 4

Surface Immobilized Gold Nanoparticles by Organometallic
Chemical Vapor Deposition on Amine Terminated Glass Surfaces[3]

4.1 Introduction

Gold nanoparticles (AuNPs) serve in a variety of scientific, medical and engineering
applications, for example acting as biosensors,[1]–[3] catalysts for nanowire or nanotube
growth,[4]–[7] and photovoltaics.[8]–[10] In addition to their plasmonic properties,[11]–[14] the
chemical properties of gold make them highly suitable for label free, extremely sensitive
biosensor applications.[15][16]

Although colloidal gold is easy to synthesize, it has many disadvantages over substrate
immobilized AuNPs. Besides the potential environmental and health impact of solution-

---

based "free" AuNPs, they require a stabilizing agent to prevent aggregation. Typically a citrate layer or a polymer coating is used to create a core-shell structure.[17] The introduction of this stabilization agent surface chemistry makes further functionalization for the application complicated. Substrate immobilized colloidal gold nanoparticle (AuNP) samples inherit the same problem. In addition, due to its liquid nature, colloidal gold requires additional handling considerations for lab-on-a-chip applications. Moreover, the 3D form of colloidal gold requires a higher volume of sample for sensing applications in comparison to "2D" surface immobilized particles.

Conventional substrate immobilized gold nanoparticle (AuNP) fabrication methods such as focused ion beam or electron beam lithography require costly setups and also suffer from low speed and small area of coverage. For prototype purposes, these drawbacks can be neglected. However, for industrial or clinical applications mass production is necessary; cost-effective, simple, and fast methods are required.

Chemical vapor deposition (CVD) is a well-studied method to produce thin films on substrate surfaces[18][19][20] mainly used in microelectronic technology.[21] In the last two decades nanotechnology started to take advantage of various forms of CVD in many different fabrication purposes. Although nanotubes[22][23] and nanowires[24][25] are the most known nanostructures produced by CVD, a variety of other structures has been reported, such as AuNPs,[26][27] AuNP/semiconductor and AuNP/titania composites,[28] AuNP/transition metal composites,[29] SiO_2 sandwitched AuNP arrays,[30] AuNP doped vanadium dioxide thin films,[31] and titanium dioxide/tin dioxide nanocomposites.[32]

Organometallic precursors form metallic thin films on substrate surfaces.[18][33][34] Under certain conditions, film growth follows an island formation scheme, which is also known as Volmer–Weber growth[36]. Interrupting the procedure before forming thin films yields metallic nanoparticles. [19][27][34][35] In terms of wetting conditions, the Volmer–Weber growth mechanism can be expressed mathematically by the Young-Dupre equation [36]:

$$\gamma_{SV} = \gamma_{CS} + \gamma_{CV}cos\theta \qquad [4.1]$$

In this equation γ_{SV} is substrate-vacuum surface tension, γ_{CS} the substrate-film interface tension and γ_{CV} the film-vacuum surface tension (Figure 4.1).
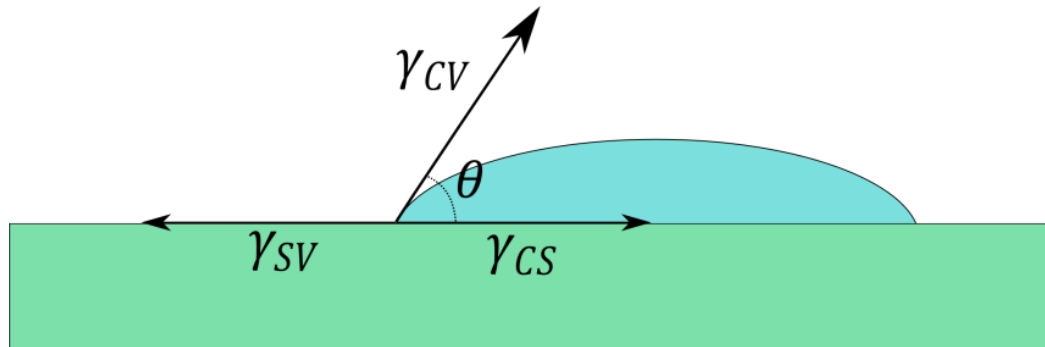
Figure 4.1. Wetting angle and surface tensions in Volmer-Weber growth

For values of θ higher than 0° attractive forces between the two deposited metal atoms are higher than the forces between the substrate and the deposited metal atom. Therefore a stable film structure is not favorable but island growth occurs.[36]

CVD is a surface chemistry selective process, meaning the substrate surface can be functionalized, creating areas with and without film growth.[33][34][37][38] The desired

surface functionalization to create nucleation sites can be achieved for example, by a self-assembly process; dithiols are used on metallic surfaces and silanes on oxidized surfaces to form self-assembled monolayers (SAMs).[39] The stability of the AuNPs grown by OMCVD strongly depends on the quality of the self-assembled monolayer (SAM). The localized surface plasmon resonance (LSPR) frequency of AuNPs lies in the visible part of the electromagnetic spectrum; therefore, the substrate should be transparent for transmission-based plasmonic sensors applications. Although glass substrates are high quality and widely used for similar purposes, our studies show that functionalization of the glass surface by employing wet silane chemistry is especially challenging.[40] The self-assembly process is very sensitive to experimental conditions, including temperature and humidity, which decreases batch-to-batch reproducibility and stability of the AuNPs on the surface.[41]–[44] When flushing is required for a biosensor application in a liquid handling system, the immobilization stability of the particles, the ability to not being moved by the liquid, is especially crucial. Poor quality of the SAM causes particles to be physisorbed on the surface, missing the chemical bonds to the substrate. These physisorbed particles can then be moved by the sensor solution, and cause undesired optical effects in the biosensor application. Typically, nanoparticle aggregation on the surface occurs, creating false signals or, due to detachment and loss of particles, a decrease in signal and/or in the signal-to-noise ratio emerges.[40]

In this study, we introduced the growth of stable AuNPs on amine functionalized BK7 glass surfaces via OMCVD using (trimethylphospine)methylgold ((CH_3)$_3$P]AuCH$_3$) precursor. Amine groups are known for their strong affinity to gold.[17][45] Several studies were reported immobilizing colloidal AuNPs on aminosilane functionalized

surfaces.[25][46]–[48] Hexamethyldisilazane (HMDS) silanization is a standard process in lithography to enhance photoresist adhesion.[49] In order to create nucleation sites for growth of AuNPs by OMCVD, surface functionalization of the substrate was achieved by vapor deposition of HMDS in a totally environmentally controlled vapor deposition oven, instead of wet chemistry in a glove box. We systematically varied the OMCVD time to investigate the time dependence of the size and interparticle distance properties of these randomly positioned AuNPs. The samples fabricated with different OMCVD times were characterized by UV-Vis absorption spectroscopy and scanning electron microscopy. Correlations between growth time, size, interparticle distance, and UV-Vis absorption maxima were established. Stability tests were performed by washing and rinsing cycles using various organic solvents to simulate liquid handling systems in sensor applications. The biosensing capabilities of the stable OMCVD-grown AuNP samples were tested by implementing the well-known biotin-streptavidin system.[50]

4.2 Results

Figure 4.2a shows absorption spectra of eight individual samples grown for 15 min in the OMCVD reactor. The maximum of the absorption spectrum corresponds to the localized surface plasmon resonance (LSPR) peak. The averaged absorption spectra for the eight samples in each batch for the various OMCVD times are depicted in Figure 4.2b. Figure 4.2c shows the position of the absorption peak maximum with increasing growth time. With increasing OMCVD time, the LSPR peak shifted to the red with increased standard deviation. Change in the LSPR peak can also be seen by naked eye (Figure 4.3).
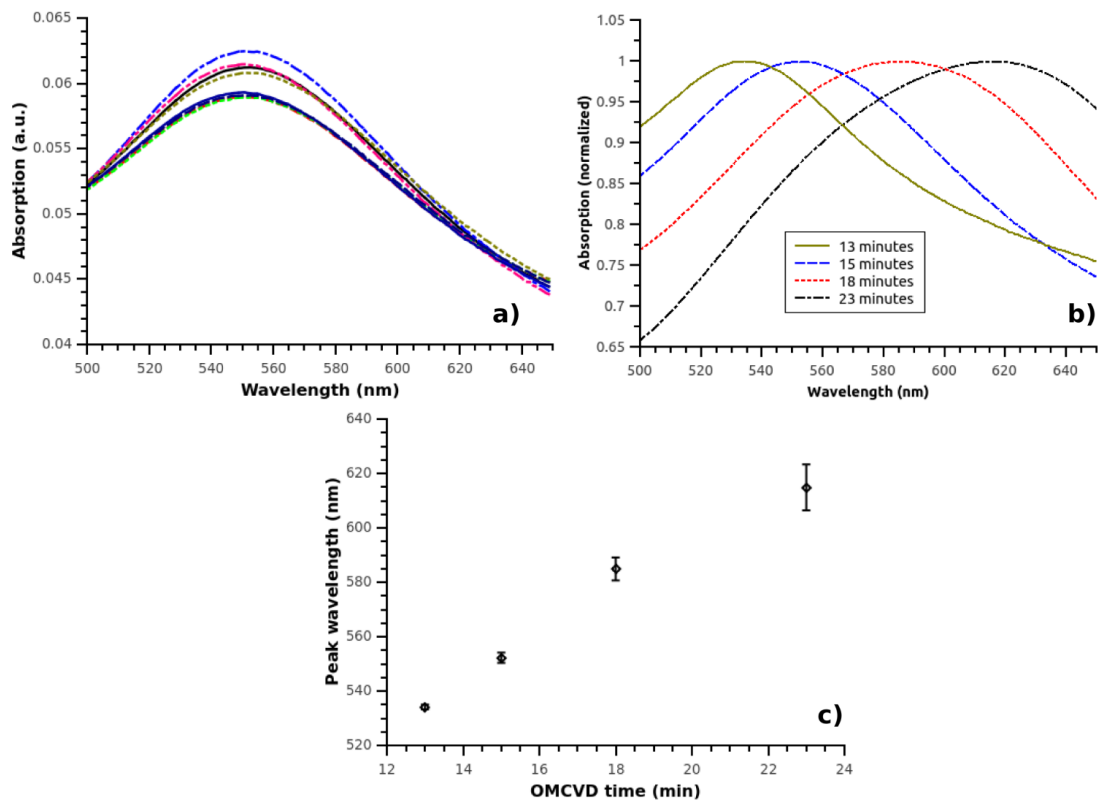
Figure 4.2. Spectral properties of AuNPs fabricated by OMCVD: a) absorption spectra of eight samples from a single batch with an OMCVD growth time of 15 min, b) averaged absorption spectra for different OMCVD times averaged over all samples in the batches, c) spectral LSPR position as a function of OMCVD time
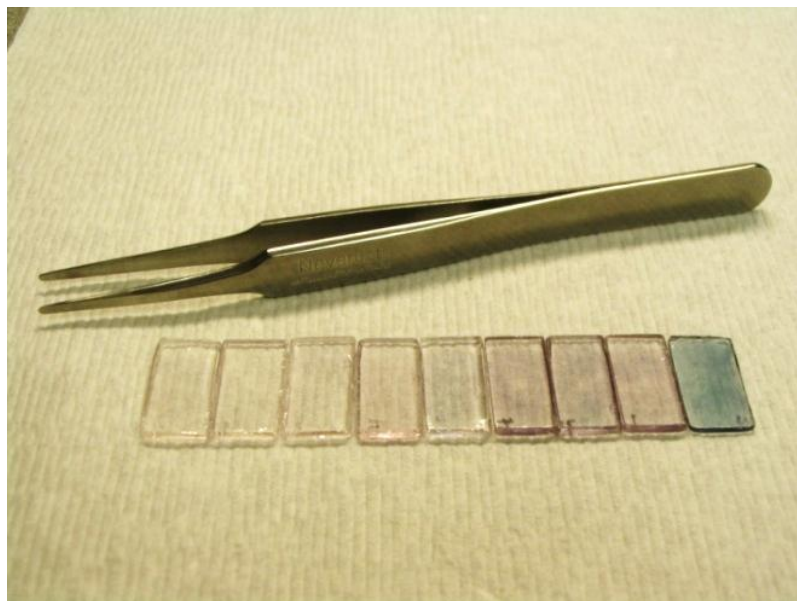
Figure 4.3. Samples fabricated with various OMCVD times, color of the sample as a function of the size shape and inter-particle distance, changes by increasing deposition time

Since differences between absorption spectra of samples within the same batch were negligible compared with differences between samples from different batches with increasing OMCVD times (Figure 4.2c), one sample from each batch was selected and electron microscopy images were taken of eight locations uniformly distributed on these samples (Figure 4.3a, inset). Figure 4.3a is an SEM image with 20,000 x magnification showing the uniformity at a wide area. A 100,000 x magnification allowed observation of the shapes of the individual nanoparticles (Figure 3b). For lower OMCVD times, AuNPs were round (Figure 4.3b, bottom). Increasing the OMCVD time yielded nanoparticles with corners, or even star shapes exhibiting clear crystalline facets (Figure 4.3b, top) which indicates the crystalline structure of OMCVD grown AuNPs on SH terminations as previously reported.[27]
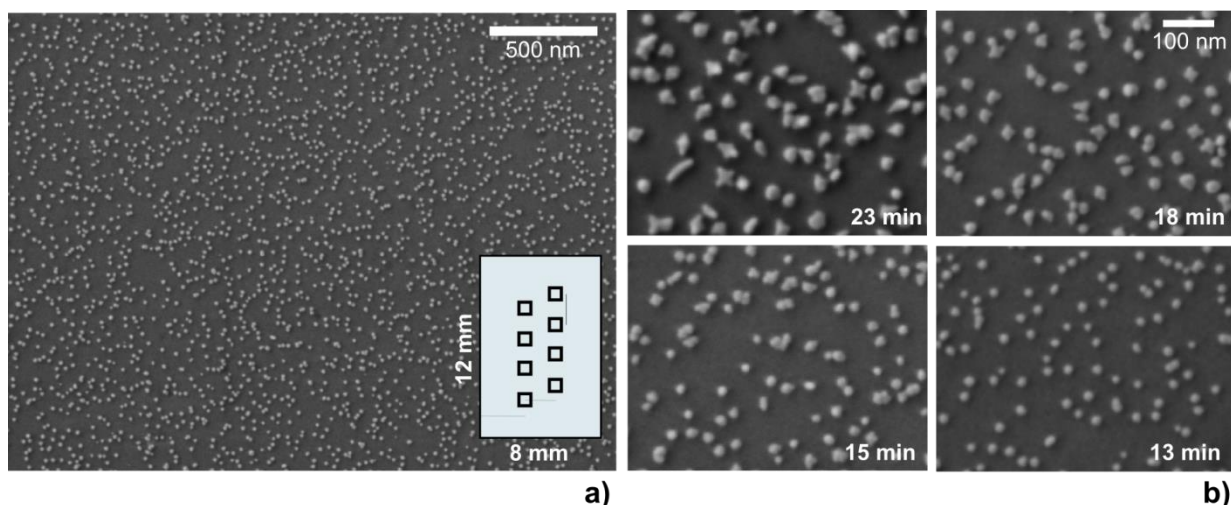
Figure 4.4. Scanning electron micrographs of AuNPs grown on –NH functionalities: a) view at large scale (tOMCVD= 15 min). The inset shows the sample geometry and the positions where the eight higher magnification images were taken. b) High magnification of samples fabricated with OMCVD times from 13-23 min.

The size and distance between individual AuNPs were analyzed in the scanning electron micrographs. Figure 4.5a is a representative example showing the area distribution of the 13 min OMCVD sample as measured and analyzed by SEM. Figure 4.5b shows the distribution of the center-to-center interparticle distance for the 15 min OMCVD sample. For the other batches with increased OMCVD time, the shape of the histograms remained the same, although the particle size shifted to higher values and larger variation in size was observed.
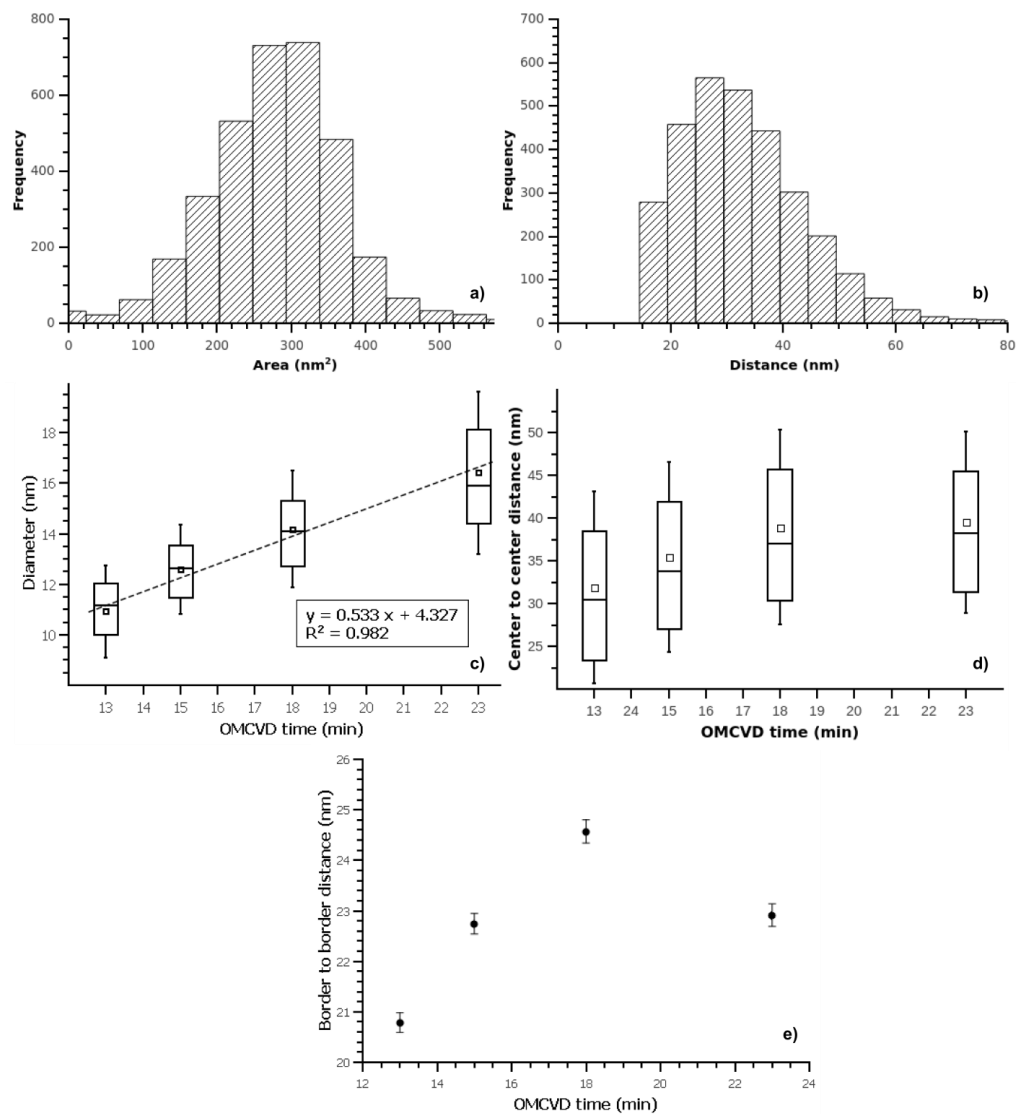
Figure 4.5. Size and distance distribution of AuNPs: a) area histogram of 13 min OMCVD sample, b) center-to-center distance histogram of 15 min OMCVD sample, c) box plot of calculated diameters of the samples with various OMCVD time (assuming round objects in all cases), d) box plot of center-to-center distance with OMCVD time, e) calculated border-to-border distance as a function of OMCVD time with standard error. For both diameter and distance measurements, the error bars show the standard deviation, the boxes show the 25% to 75% intervals of the data, and the small square dots show the mean values.

Low OMCVD times led to growth of small particles, increasing time yielded larger particles with less uniform size distributions. Figure 4.5c shows the diameter distribution of the particles based on a calculation of the diameter from the area. Although not all AuNPs obtained by growth for 18 min or 23 min were round, their areas were approximated as circles to give a clear sense of size when the data were converted to diameters. The calculated average diameter increased from ~11 nm to ~17 nm in a linear fashion by increasing the growth time from 13 to 23 min, implying a growth kinetic constant of roughly 0.5 nm/min.

The average center-to-center distance between the AuNPs increased with reaction time and reached a plateau (Figure 4.5d). As depicted in Figure 4.5e, the mean border-to-border distance, calculated from the diameter and interparticle distance distributions, increased up to 18 min and then decreased slightly.

It is critical to ensure the stability of the particles used in biosensor applications. The absorption spectra of our samples remained unchanged within the error range of the spectrometer after applying all rinsing cycles in the stability tests. Changes in the absorption maximum were less than 0.1 nm which is the measurement error of the experiment. AuNP formation is also observed for cleaned glass samples without HMDS functionalization. However, the LSPR vanished after the stability tests indicating that the AuNPs did not stay on the surface; they were washed off, indicating a poor attachment to the surface. AuNP formation and deposition can be completely avoided by functionalizing the surface with –CH$_3$.

Figure 4.5 shows the results of a bulk refractive index experiment. Immersing the sample in organic solvents with different refractive indices changes the LSPR frequency. An increasing refractive index causes a red shift in the maximum of the absorption curve (Figure 4.5a). Figure 4.5b shows the absorption peak change by the refractive index. Slope of the curve is defined as figure of merit (FOM) of the sensor. FOM for 15 minutes deposition time OMCVD grown particles is calculated as ~97 nm/RIU.
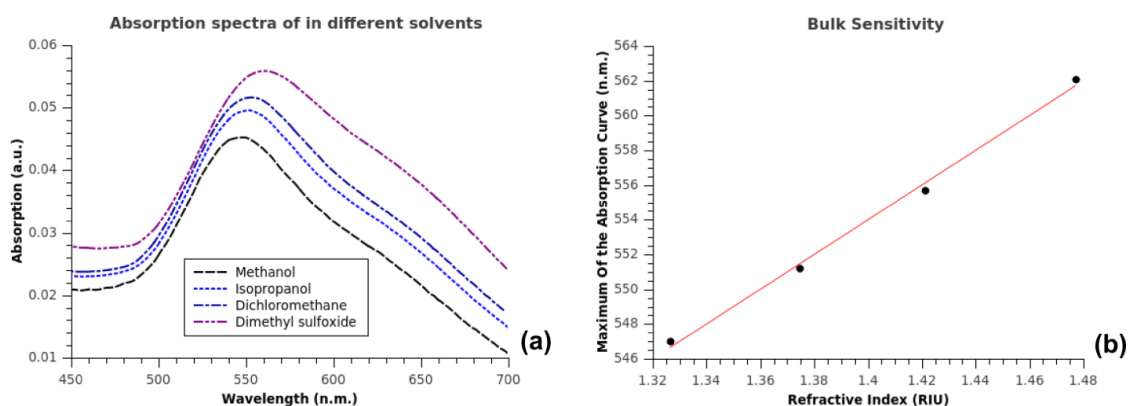
Figure 4.6. (a) Absorption spectra of a sample immersed in various solvents with sytematically increasing refractive index. (b) Wavelength of the maximum in the absorption curve versus the refractive index of the solvents.

Figure 4.6 shows the sensor response of the sample to high affinity system biotin-streptavidin. The biotin recognition site is immobilized on the AuNPs and the streptavidin is detected due to its binding to the biotin moieties.[50] The dipolar LSPR spectral position versus increasing streptavidin concentration was investigated on samples with a growth time of 15 minutes giving ~13 nm of mean particle diameter and 23 nm of average border-to-border distance. Between 10 ng/ml to 100 μg/ml

concentration range the limit of detection was calculated by the 3σ method [50] and was found to be better than 10 ng/ml (~200 pM).
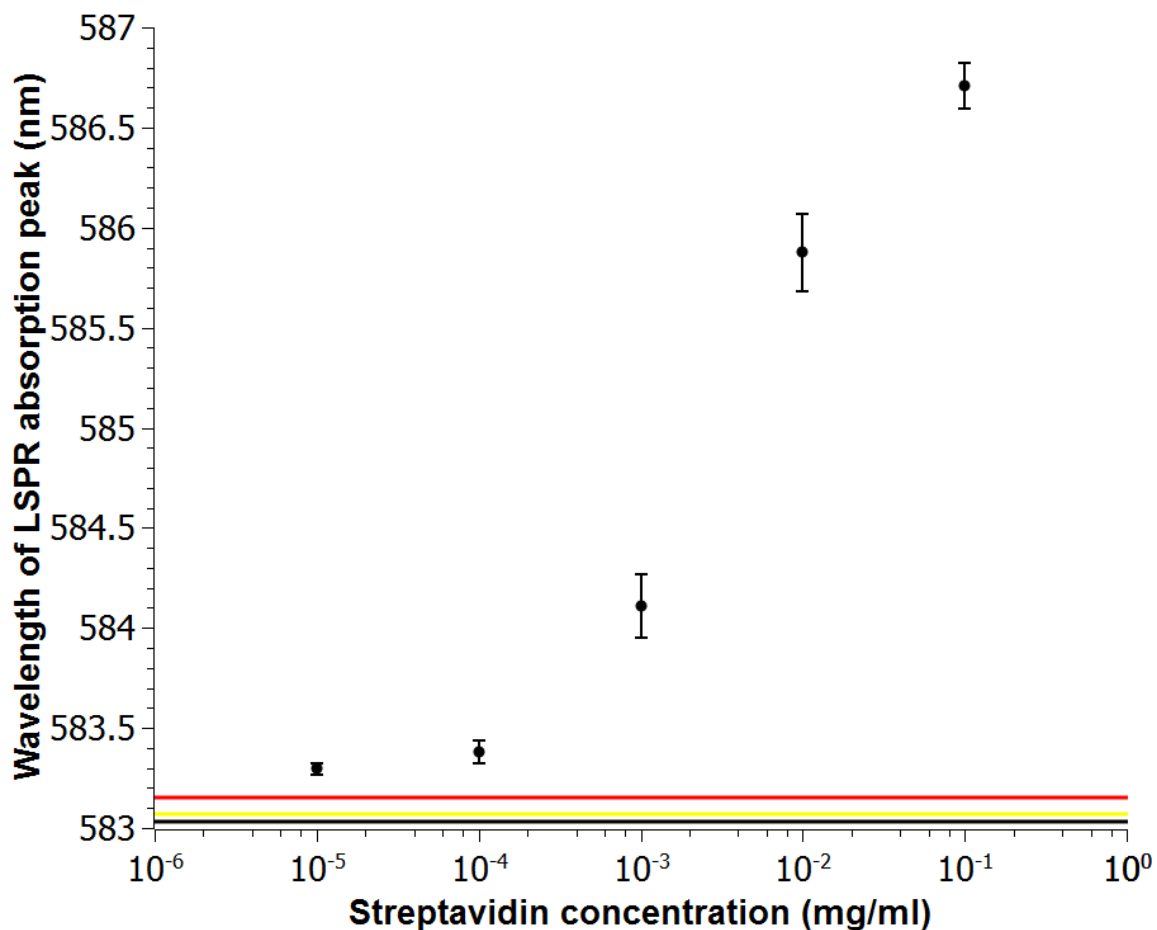
Figure 4.7. Streptavidin concentration response of OMCVD AuNP-based sensor. The black line represents the base line, the yellow line the detection uncertainty, and the red line the base line plus three times the detection uncertainty.

4.3 Discussion

The high affinity of gold to amine has been used in multiple cases for the immobilization of gold colloids, however the precise chemical mechanism has not been discussed.[17],[25],[45-48] The –NH terminated surface investigated here obviously serves as a growth surface for OMCVD of AuNPs; nucleation and growth happens. It is not within the scope of this work to determine the exact reaction mechanism of the Au-precursor to the available –NH groups, however we assume a favorable interaction between the lone electron pair of the nitrogen on the sample surface and the Au(I) in the precursor. Gold exists in various oxidation states. Au(I), for example as present in the implemented precursor, forms numerous complexes of which many are stable, but also easily undergo ligand exchange reactions.[51] The $(CH_3)_3P]AuCH_3$ precursor is a donor-acceptor complex,[52] potentially involving Lewis acid (LA)- Lewis base (LB) interaction. We propose for the first growth step a surface-ligand-exchange reaction, where the phosphorous group of the precursor, $-P-(CH_3)_3$ (the LB of the precursor) is displaced by the nitrogen group –NH (the new LB) on the surface. With this first step, the LB Au-CH_3 is immobilized at the surface via the Au(I) whereas the phosphorous group is released into the gas phase. The binding constants from Au(I) to the $-P-(CH_3)_3$ was found to be 242.42 kJ/mol experimental and 250.37 kJ/mol theoretical, respectively,[53] whereas the binding energy of Au^+-NH_3 was found to be 265.86 kJ/mol [53], larger in comparison to the phosphorous. The binding energy of Au(1)-NH may be even larger.

In a second step, due to the high gold-gold affinity, the Au of a second precursor molecule may bind to the immobilized gold species. When the oxidation state of the Au nucleus changes into a Au(0) state cannot be demined without additional experiments.

Due to the LSPR phenomenon, the size, interparticle distance and shape of the AuNPs determine their absorption spectrum.[11]–[14] Therefore, UV-Vis absorption spectroscopy provides an easy and economical way to characterize such samples. The LSPR peak shifted to the red with increasing OMCVD time, indicating that the particle size increased, the interparticle distance decreased, and/or the particle shape changed from a round to a more angular shape.[11][12] The increase in the observed standard deviation indicated that increasing the growth time increased the inhomogeneity of the samples.

For all samples and all batches, the relative standard deviation in the particle number observed in the images for the eight locations was less than 10%, which indicated homogeneity of the particle distribution along the surface. Figure 4.4a is an SEM image with 20,000 x magnification showing the uniformity at a wide area. A 100,000 x magnification allowed observation of the shapes of the individual nanoparticles (Figure 3b). For shorter OMCVD times, AuNPs were round (Figure 4.4b, bottom). Increasing the OMCVD time yielded nanoparticles with corners, or even star shapes (Figure 4.4b, top). Round particles are useful for transmission-based plasmonic sensor applications and nanowire growth.[7][54] Particles with corners are suitable for surface enhanced Raman spectroscopy (SERS) applications, due to hot spot formation around the edges.[55]–[59]

The size and distance between the AuNPs are important parameters for plasmonic sensors, and the LSPR properties of the particles strongly depend on them. Narrow particle size distribution is usually desired for biosensor applications. If the LSPR band increases in width, errors in determining the absorption peak spectral position increase which decreases the limit of detection.[60] Although OMCVD is a statistical process, the box plot in Figure 4c shows a narrow size distribution comparable with colloidal gold

produced by the citrate reduction method.[61] On the other hand, limit of detection calculations with the biotin-streptavidin platform showed that size distribution allows biosensor applications.

Increase in the average center-to-center distance between the AuNPs with reaction time (Figure 4.5d) showed that for the shorter times, AuNPs were individually well separated. With increasing time, close particles merged, forming a single larger particle. This merging increased the average interparticle distance until most particles were large and again well separated. The shape of the border-to-border distance curve is a result of close-particle-merging and increase in the particle size by time. After 18 min, most of the close particles had merged (Figure 4.5d), and therefore, the center-to-center distance did not increase anymore. However, the diameter of the nanoparticles kept increasing, which decreased the border-to-border distance after 18 min (Figure 4.5e), creating hot spots for surface enhanced Raman spectroscopy [55][56] and enabling optical cross-talk as a sensing mechanism for transmission-based sensors. [3][26][37] Such a close spacing of ~20 nm between the particles has not been achieved by conventional fabrication methods such as electron beam lithography or focused ion beam lithography.

Fabrication of AuNPs with a precise size is possible by adjusting the OMCVD time. However, it should be noted that increasing OMCVD time will yield less uniformity in shape, size, and interparticle distance. Higher reaction times will lead to connected AuNPs, creating islands and eventually yielding a thin film of gold.[19]

For a quick and economic characterization process, it would be valuable to learn about the size distribution of the AuNPs by UV-Vis absorption spectra. Figure 4.8 shows the

relationship between the spectral peak position of the LSPR and the diameter of the AuNPs. The spectral position of the LSPR showed a linear relationship to the average diameter.
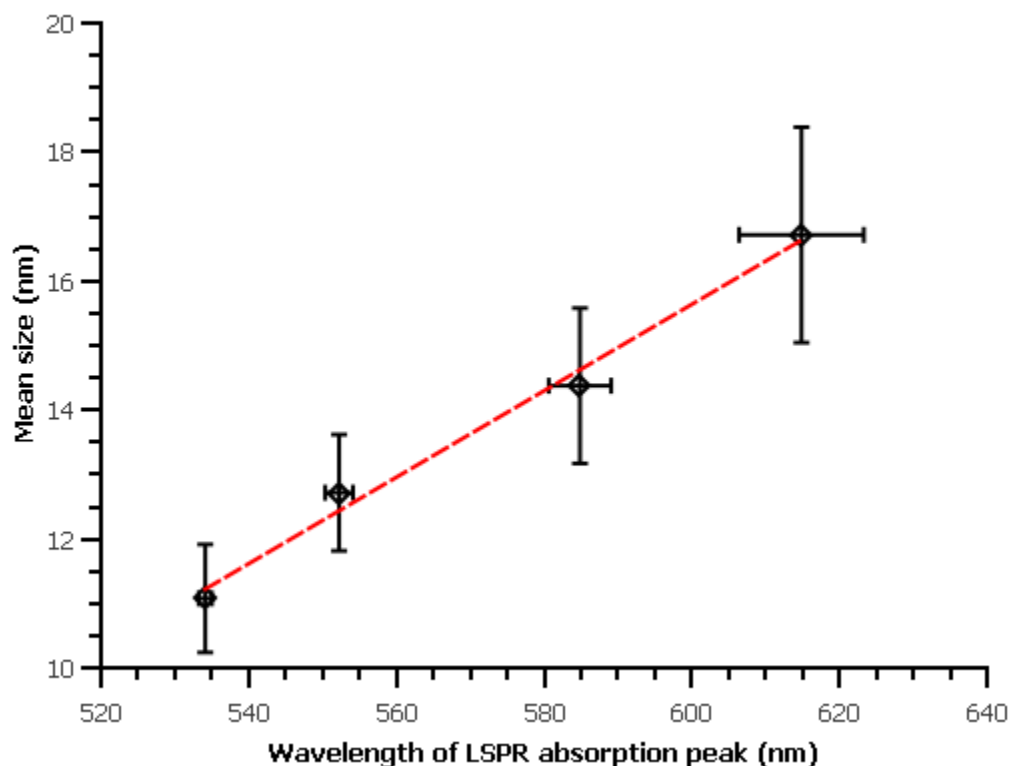
Figure 4.8. Relationship between wavelength of the LSPR absorption maximum and the average particle diameter of the AuNPs.

Amine functionalized samples with AuNPs were stable against washing/rinsing experiments simulating liquid handling conditions. This showed that the particles are chemically bonded to the surface. Absence or poor quality of the HMDS SAM on the substrate caused loosely attached AuNPs; the particles "float", aggregate, or move away from the surface.[40] Loss of particles decreases the strength of the LSPR of the sample

and decreases the signal-to-noise ratio in the absorption spectrum. Aggregation of the particles causes cross-talk, which appears as a shoulder in the absorption spectrum or widens the LSPR peak, leading to larger errors and higher noise if the dipolar LSPR peak is used to determine the sensor signal.

Bulk sensitivity measurement shows that sensor has a linear response to the refractive index of the vicinity between the ranges of 1.32 RIU to 1.47 RIU. Slope of the graph was calculated as ~97 nm/RIU, which is called figure of merit of the sensor. It should be noted that higher figure of merit is not an indicator of a high surface sensitivity. Protein sensing experiments should be evaluated with error of the system to determine the sensitivity and limit of detection.

LSPR of AuNPs is highly sensitive to changes in the refractive index of the surrounding environment, which is the phenomenon behind the plasmonic sensors. Biotinilated-thiol is the linker molecule between the AuNPs and streptavidin. [50] As the concentration of the protein streptavidin increases, the surface coverage of streptavidin on the biotin labels on the nanoparticles increases appearing as a red shift in the LSPR absorption maximum. The limit of detection is 10 ng/ml (~200 pM) being in the same order of magnitude than other nanoparticle surface plasmon resonance sensors reported.[2][63][64] This proof of principle experiment can easily be modified by using appropriate linker chemistry to detect any important biomolecule. The dependence on the linker chemistry, especially the dependency on the particular binding constant, and the AuNP size must be optimized for each individual sensor to achieve the highest possible sensitivity. To employ the optical cross-talk in a sensor scheme additionally the AuNP interparticle distance must be optimized.[62]

4.4 Conclusion

We have introduced a new, simple and inexpensive approach for fabricating highly stable AuNPs via OMCVD on amine functionalized glass surfaces. Increasing the OMCVD time yielded larger particle sizes and closer border-to-border spacing. Round particles were transformed to angular particles and their size became less uniform with increased deposition times. Increasing size, decreasing spacing and a change into angular shapes caused a red shift in the LSPR of the AuNPs. Therefore, we were able to establish a relationship between the AuNP attributes and their absorption spectrum. Vapor phase deposition of HMDS in an oven provided reproducible and high quality amine functionalization. Washing and rinsing cycles with various solvents to simulate the liquid handling conditions of biosensor applications did not cause a change in the absorption spectra of the samples, indicating that the AuNPs were stably held in position on the substrate. Biotin-streptavidin recognition experiments showed the biomolecule sensing capabilities of the samples. AuNPs fabricated by OMCVD could be used for biosensor applications; however, the effect of size, shape and interparticle distance on fundamental sensor parameters such as limit of detection and sensitivity must be investigated and fine-tuned for each individual linker-chemistry applied.

The effect of various temperatures and pressures used in the OMCVD process in terms of the size, shape and interparticle distance of the resulting particles needs further investigation. It is expected that a decrease in reaction temperature will slow the growth rate, so that fine tuning, especially for smaller particles, will become feasible. Control of interparticle spacing and improved uniformity may also be achievable. The interparticle distance could be adjusted independently using various techniques for sensor tunability,

such as manipulating the binding sites with FIB[65][64] or using binary mixtures of HMDS and OTS.[66][67]

These stable OMCVD AuNPs can also be used where substrate immobilized bare AuNPs are required, e.g. for the growth of nanowires and fabricating photovoltaic devices. Depending on the application, different substrates can be used as long as amine functions can be bonded to the surface. This process itself does not involve any wet chemistry nor ion beam technology; it is therefore advantageous for 3D samples with a complicated surface geometry, and can direly be applied in lab-on-a-chip technology.

4.5   Experimental

4.5.1 Optimization of the OMCVD process

Oven to water bath and flat bottom chamber

We started with a home build hot wall reactor heated by oven. Using an oven as a heat source for the reactor yields high evaporation speed of the precursor. However, this method causes high inhomogeneities; the sample to sample differences are large and the AuNP distribution along an individual sample is inhomogeneous. This non-uniformity can be seen qualitatively by the naked eye due to the color the AuNPs produce, but can also be detected quantitatively by UV-Vis absorption spectroscopy (Figure 4.10a). Since there is no external gas flow into the chamber mass transport is provided by internal convection. Heating the entire chamber does not create a uniform convection. Placing the chamber partially in a water bath provides a uniform temperature gradient increasing the homogeneity along the sample surface as well as between the samples and increases reproducibility significantly.
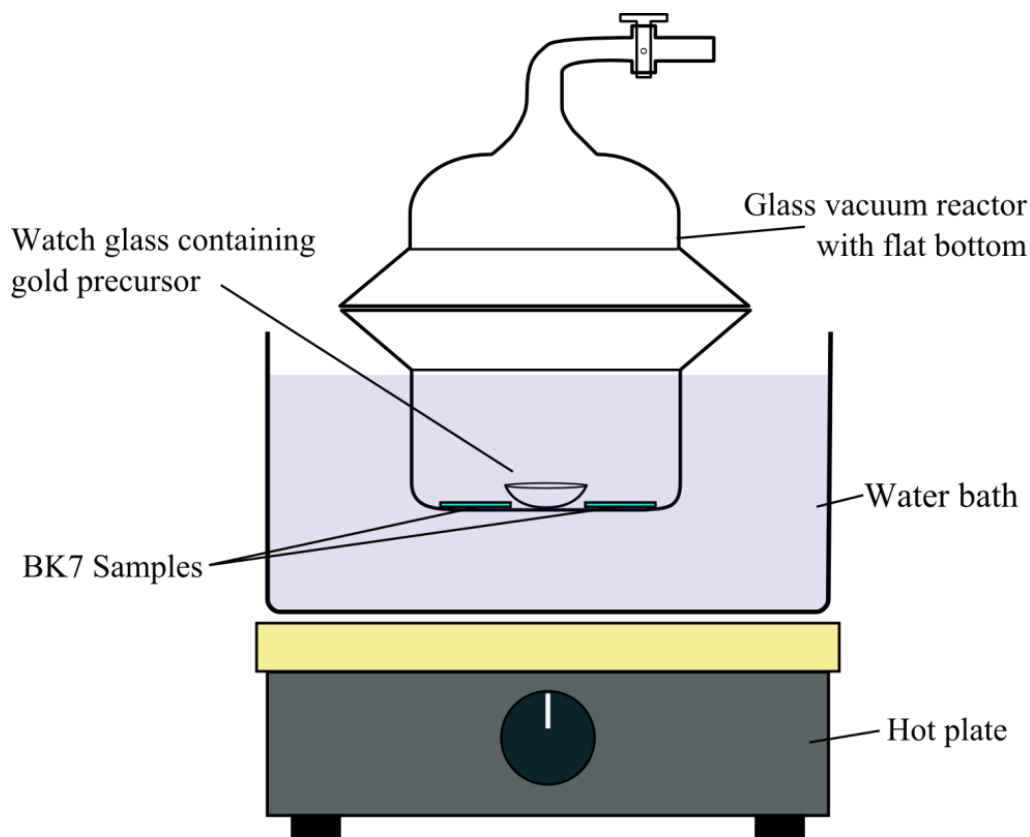
Figure 4.9. Illustration of the OMCVD setup

On the other hand, surface temperature of the samples affects the reactivity, therefore reactor surface roughness adversely affect the quality of the samples and the batch. Flat bottom reactors, allowing the flat samples to have an optimum heat contact to the reactor wall, deliver the best sample homogeneity. Figure 4.10 shows UV-Vis absorption spectra of two different batches; one was oven heated in a rough bottom chamber (Figure 4.10a) and the other one was fabricated in a flat bottom chamber in the water bath (Figure 4.10b). OMCVD parameters were 65 ℃ reaction temperature and 0.050 mbar initial reactor pressure, 20 mg precursor, 17 minutes reaction time.
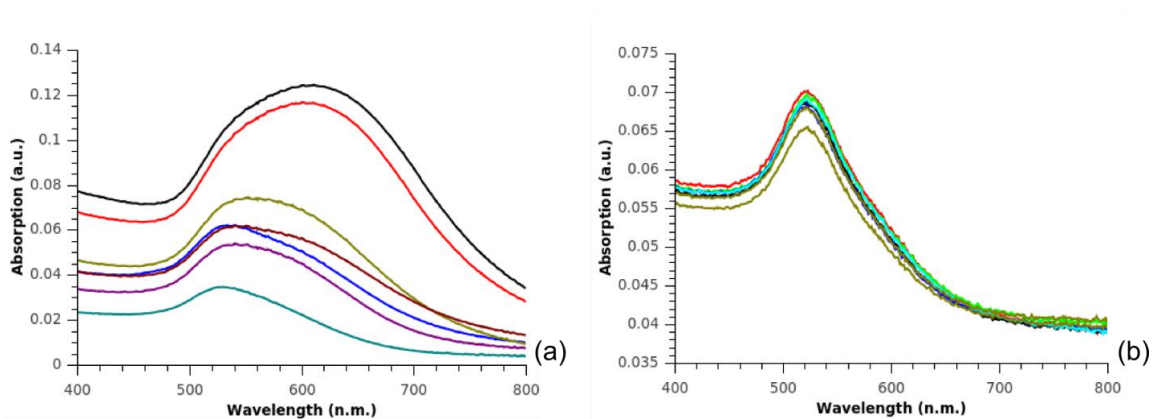
Figure 4.10. Absorption spectra of two different OMCVD batches; AuNP growth performed (a) in an uneven bottom reactor and an oven as the heating source, and (b) flat-bottom reactor in a water bath

Surface functionalization of the substrate for OMCVD

The success of all individual steps of the sample preparation procedure allows the formation of the chemical bonds between the substrate and the AuNPs. If the quality of the self-assembly layer is poor, the number of physisorbed AuNP is high. Since they are not strongly attached to the substrate surface they can aggregate or detach from the surface while using the sample in a solution. Figure 4.11a and Figure 4.11b shows a sample with many physisorbed AuNPs before and after immersion in ethanol and subsequent drying.
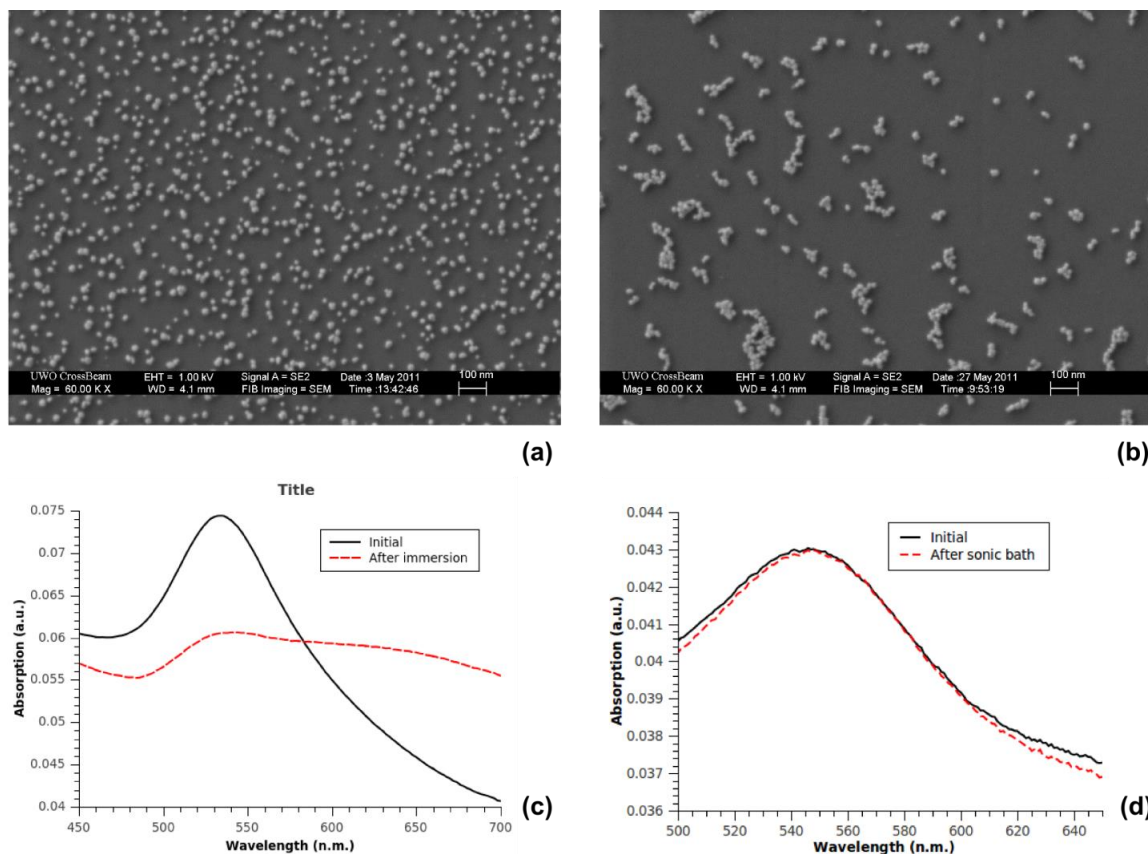
Figure 4.11. SEM images of a sample with physisorbed AuNPs; (a) before processing, (b) after immersing in ethanol and subsequent drying. (c) UV-Vis spectrum of the same sample before and after processing. (d) UV-Vis spectra of a sample with chemically bonded AuNPs

Aggregation is clearly observed in those SEM images as well as a decrease in the amount of AuNPs. This can be observed in the UV-Vis spectra of the samples (Figure 4.11c). Lost particles cause a decrease in the absorption signal and due to the aggregation a cross-talk shoulder appears. Therefore, the LSPR peak gets significantly wider diminishing the high sensitivity of the method.

In order to establish a strong bond between the substrate, quality of the functional surface is crucial. Wet silane chemistry with thiol groups yielded poor reproducibility with physisorbed particles indicating problems in the self-assembly process. Using a totally environmentally controlled vapor deposition oven with amine functionalization provided chemisorbed particles with high reproducibility. Figure 4.11d shows absorption spectra of a sample before and after sonicating indicating that AuNPs are chemically bonded to the substrate surface.

Functionalization of the chamber surface

The inner surface of a glass reactor (Figure 4.9) was functionalized wet chemically with octadecyltrichlorosilane (OTS) (Figure 7c), which forms a non-growth surface. This SAM avoids gold deposition on the inner walls of the reactor.[38] This procedure increases the reproducibility as well as the efficiency of AuNP growth process by avoiding unnecessary precursor consumption. Figure 4.12 shows absorption spectra comparison of two batches; prepared in bare reactor and OTS functionalized surface in the same experimental conditions. OTS functionalized surface yields larger and denser AuNP formations with increased reproducibility.
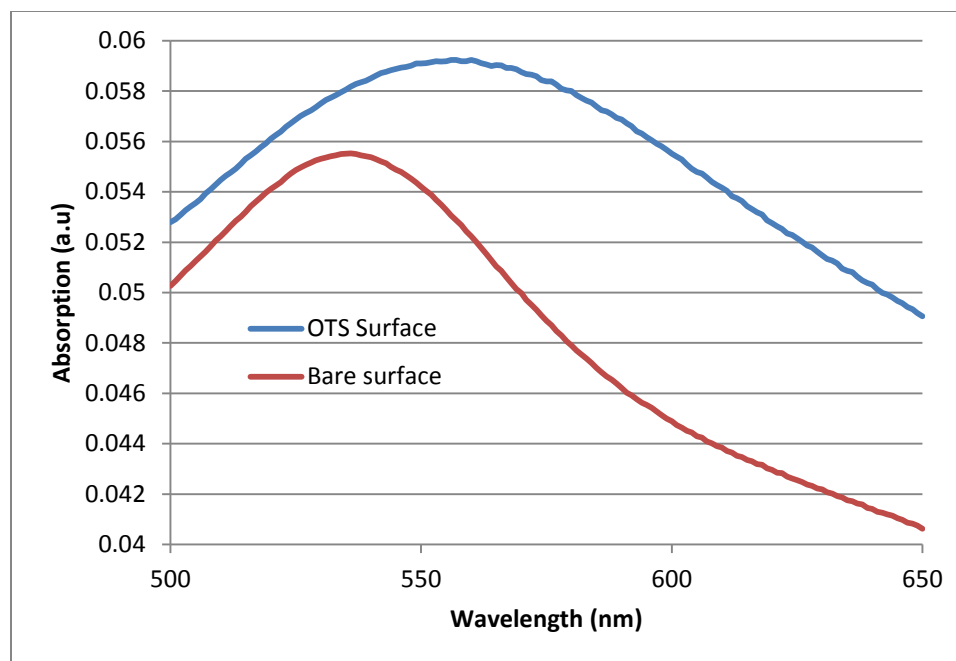
Figure 4.12. Absorption spectra of two batches; bare and OTS functionalized chamber

4.5.1 Substrate selection

There are two main aspects in substrate selection: chemical and optical properties. Chemical composition and surface chemistry have a huge impact on the quality of the final product: particle size distribution, homogeneity, and stability of the particles. Silicon wafers are a good candidate material; however, transmission based LSPR sensors require transparency at the range of the LSPR wavelength. This wavelength depends on the size of the AuNPs and corresponds typically in the visible to near infrared region of the spectrum. On the other hand, if the sensor is based on an optical waveguide in an optical lab-on-a-chip, the substrate should be suitable for waveguide fabrication procedures, e.g., ion exchange. BK7 (Schott, Germany) is a high quality glass, exhibiting more than 90%

transmission between 350 nm and 2,500 nm [37]. Ion exchange and surface functionalization properties are well studied [4][40][42].

4.5.2 Fabrication of AuNP samples

All chemicals were used without further purification. BK7 (Hellma, Germany) glass slides (8 x 12 mm) were immersed in Nano-Strip solution (Cyantek Inc., CA, USA) at 60°C for 20 min to remove possible contaminants. Substrates were then rinsed with abundant amounts of Milli-Q water (MilliPore, MA, USA), dried with nitrogen, and placed in an STS Reactive Ion Etch system (STS Surface Technology Systems, Newport, UK) in an oxygen plasma at 80 W for 20 min to oxidize the substrate surface, creating – OH functionalities (Figure 4.14a). The hydrophilic nature of the samples was confirmed by contact angle measurements ($\theta < 2°$) (Reme-Hart Model 200 Ganiometer, Reme-Hart Co. NJ, USA). For surface functionalization with –NH groups, silanization of the substrates with 100% HMDS (Figure. 4.13a) (Transene Inc., MA, USA) in a YES-3TA HMDS vacuum oven (Yield Engineering, CA, USA) was carried out. The contact angle θ, measured as $68.9° \pm 0.6°$, confirmed the surface modification.
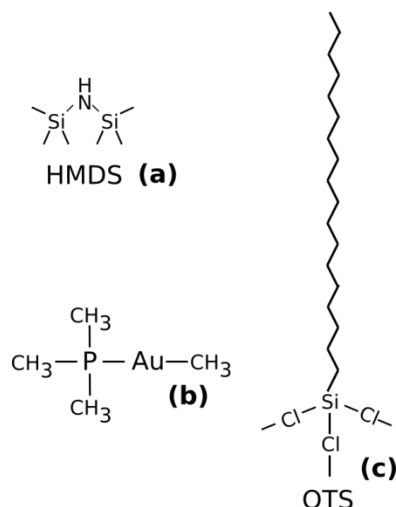
Figure 4.13. Structure formula of compounds implemented in AuNP sample fabrication and to yield an inert glass reactor: a) hexamethyldisilazane (HMDS), b) the organometallic gold precursor trimethylphosphinegoldmethyl ($[(CH_3)3P]AuCH_3$), and c) octadecyltrichlorosilane (OTS)

First, the OMCVD glass reactor was filled with freshly prepared piranha solution (1:3 v:v H_2O_2:H_2SO_4). It was given two hours to oxidize the inner surface (creating –OH functionalities). The reactor was then rinsed with copious amounts of Milli-Q water, dried with nitrogen, and placed in a vacuum oven at 95°C for 20 min to remove any moisture from its surface. A 1:500 v:v mixture of OTS (97%, Sigma, Ontario, Canada) in toluene (Caledon Lab. Inc, Georgetown, ON, Canada) was freshly prepared. The OMCVD reactor was filled with the OTS (Figure 4.13c) solution overnight under an argon environment in a glove box. After SAM formation the reactor was rinsed with toluene and placed in a vacuum oven at 95°C for 20 min to form silane bonds and expel toluene from the reactor surface.

Amine functionalized substrates were placed on the reactor's flat glass bottom as well as a small watch glass containing 20 mg of the organometallic gold precursor trimethylphosphinegoldmethyl ($[(CH_3)_3P]AuCH_3$) (Figure 4.13b). The synthesis of the precursor is described elsewhere.[68] Uniform thermal contact between the reactor bottom and the samples is guaranteed by the flat-bottom reactor. Even temperature distribution along the surface of the substrate yields a uniform nucleation site density, which provides homogenous growth over the surface. The reactor was pumped down to >5 Pa and filled with argon for three cycles to ensure an inert atmosphere inside the reactor. During the last cycle, the internal pressure was set to 5 Pa. The reactor was placed in a water bath preheated to 65°C for 13, 15, 18 and 23 min. After the deposition period, the reactor was immediately vented and the samples with the grown AuNPs were removed. The bottoms of the samples (the sides that are in direct contact with the reactor wall) show less homogeneity and more physisorbed particles. This side is gently wiped with a tissue (Kimwipe, Kimberly-Clark Inc, Canada) to remove the undesired AuNPs.
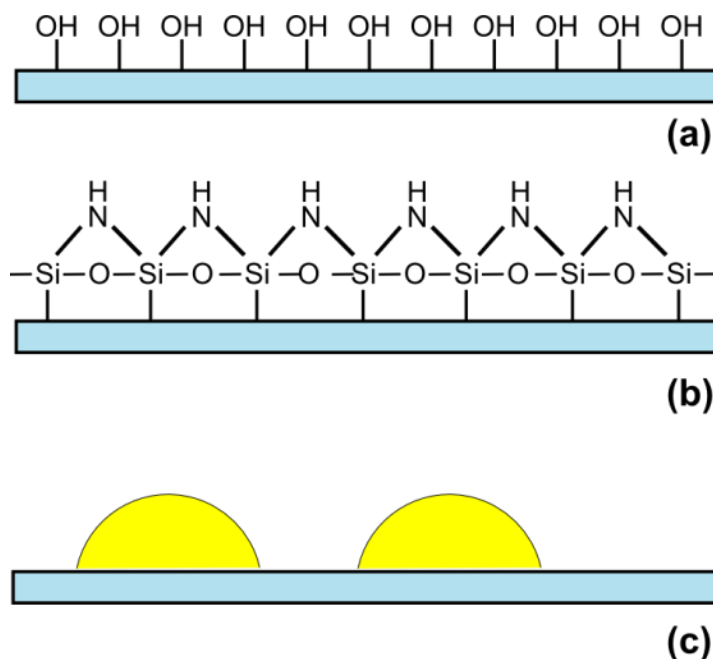
Figure 4.14. Surface modification scheme: a) substrate with oxidized surface after piranha treatment; b) silane network after HMDS functionalization; c) AuNPs on the substrate without chemistry details of the HMDS layer (not to scale)

4.5.3 Characterization

UV-Vis absorption spectra were obtained using a LAMBDA 850 UV-Vis recording spectrophotometer (PerkinElmer, Ca, USA). The absorption spectrum of a blank BK7 glass was used as a reference.

Scanning electron micrographs were acquired by a Leo 1530 scanning electron microscope (LEO Electron Microscope, Zeiss, Germany). Prior to imaging, samples were coated with 1 nm of osmium to make them conductive. ImageJ[69] software was used for processing the images. The area and two-dimensional center of mass data were extracted from the images to calculate the distribution of the center-to-center interparticle distance using a nearest neighbour algorithm.
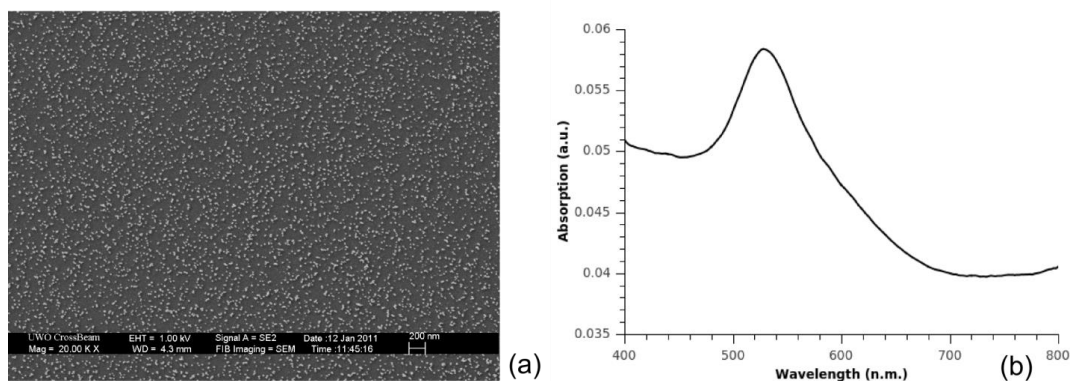
Figure 4.15. (a) SEM image and (b) UV-Vis absorption spectrum of a sample with AuNPs.

4.5.3 Stability tests

Two samples from each batch corresponding to different OMCVD growth times were rinsed with anhydrous ethanol several times to remove physisorbed particles, and then dried. After acquiring a UV-Vis absorption spectrum, the samples were immersed and rinsed repeatedly with methanol, isopropanol, and dichloromethane and then immersed in Phosphate Buffered Saline (PBS) buffer and rinsed with Milli-Q water and isopropanol.

4.5.4 Bulk sensing

Samples were immersed in a cuvette which was filled with methanol, isopropanol, dichloromethane and dimethylsulfoxide. Same solvents were used in a reference cuvette with a blank BK7 glass. Reference cuvette was placed in the reference beam in the spectrometer. Absorption spectra of the samples were measured by a Lambda 850 UV-Vis Spectrometer (Perkin Elmer Inc., Massachusetts, USA)

4.5.5 Biosensing

Samples were immersed in 0.45 mM 11-mercaptoundecanol (Sigma-Aldrich, Ontario, Canada), and 0.05 mM biotinylated thiol (NanoScience Chemicals, Phoenix, AZ, USA) in anhydrous ethanol solution for two hours to form a SAM with biotin moieties. Repeated washing with ethanol was followed by drying the sample with nitrogen. The samples were immersed first in PBS buffer and then in increasing concentrations of streptavidin in PBS buffer. Figure 4.16 show the illustration of the protein sensing experiment.
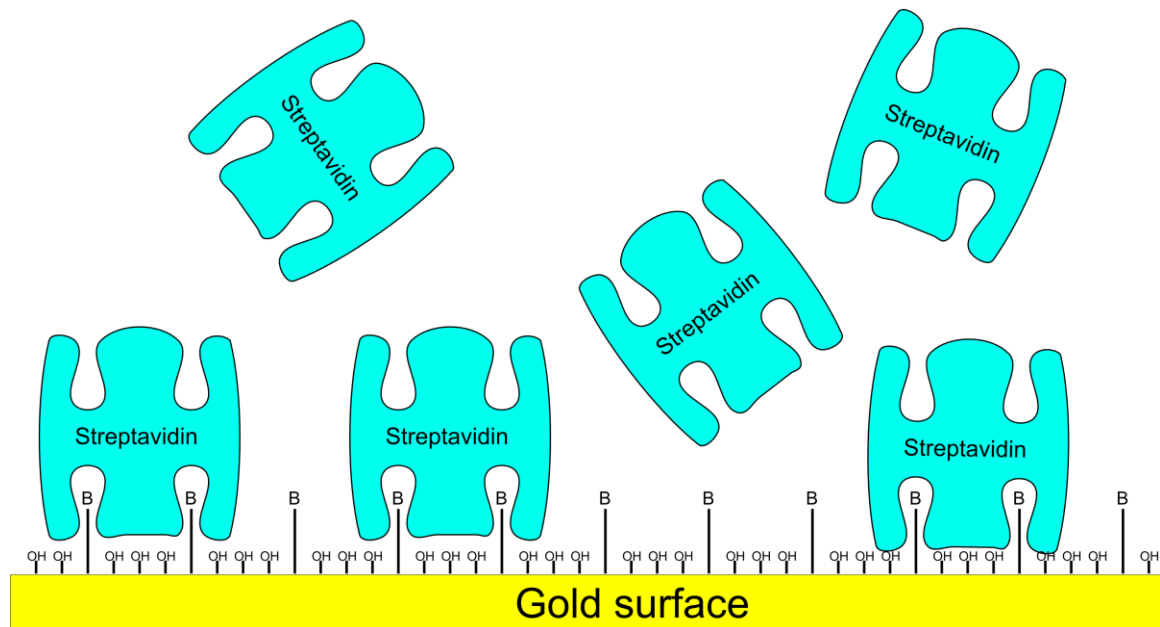
Figure 4.16. Illustration of Streptividin binding to biotinylated thiol and OH-termited thiol modified gold surface

Acknowledgements

References

[1]   E. Larsson, J. Alegret, M. Käll, D. Sutherland, *Nano Letters* **2007**, *7*, 1256.

[2]   S.M. Marinakos, S. Chen, A. Chilkoti, *Analytical Chemistry* **2007**, *79*, 5278.

[3]   S.M.H. Rafsanjani, T. Cheng, S. Mittler, C. Rangan, *Journal of Applied Physics* **2010**, *107*, 094303.

[4]   S. Lee, M. Yamada, M. Miyake, *Carbon* **2005**, *43*, 2654.

[5]   S. Bhaviripudi, E. Mile, S. a Steiner, A.T. Zare, M.S. Dresselhaus, A.M. Belcher, J. Kong, *Journal of the American Chemical Society* **2007**, *129*, 1516.

[6]   V. Idakiev, Z.-Y. Yuan, T. Tabakova, B.-L. Su, *Applied Catalysis A: General* **2005**, *281*, 149.

[7]   J. Hu, T.W. Odom, C.M. Lieber, *Accounts of Chemical Research* **1999**, *32*, 435.

[8]   N. Chandrasekharan, P.V.P. Kamat, *The Journal of Physical ...* **2000**, *104*, 10851.

[9]   J.H. Lee, J.H. Park, J.S. Kim, D.Y. Lee, K. Cho, *Organic Electronics* **2009**, *10*, 416.

[10]   N. Sakai, Y. Fujiwara, Y. Takahashi, T. Tatsuma, *Chemphyschem : a European Journal of Chemical Physics and Physical Chemistry* **2009**, *10*, 766.

[11]   T. Jensen, L. Kelly, A. Lazarides, G.C. Schatz, *Journal of Cluster Science* **1999**, *10*, 295.

[12]   K.L. Kelly, E. Coronado, L.L.L. Zhao, G.C. Schatz, *The Journal of Physical Chemistry B* **2002**, *107*, 668.

[13]   G. Schatz, *Spring* **2005**, *7*, 2032.

[14]   P.K. Jain, K.S. Lee, I.H. El-Sayed, M. a El-Sayed, *The Journal of Physical Chemistry. B* **2006**, *110*, 7238.

[15] X. Huang, P.K. Jain, I.H. El-Sayed, M. a El-Sayed, *Nanomedicine (London, England)* **2007**, *2*, 681.

[16] A.B. Dahlin, B. Dielacher, P. Rajendran, K. Sugihara, T. Sannomiya, M. Zenobi-Wong, J. Vörös, *Analytical and Bioanalytical Chemistry* **2012**, *402*, 1773.

[17] M.-C. Daniel, D. Astruc, *Chemical Reviews* **2004**, *104*, 293.

[18] M.J. Hampden-Smith, T.T. Kodas, *Chemical Vapor Deposition* **1995**, *1*, 8.

[19] N. Kaiser, *Applied Optics* **2002**, *41*, 3053.

[20] K. Choy, *Progress in Materials Science* **2003**, *48*, 57.

[21] T. Kodas, M.J. Hampden-Smith, *The Chemistry of Metal CVD*, VCH**1994**.

[22] M. Endo, K. Takeuchi, S. Igarashi, *Journal of Physics and ...* **1993**, *54*, 1841.

[23] H. Dai, A. Rinzler, P. Nikolaev, *Chemical Physics ...* **1996**, *4*.

[24] F.N. Ishikawa, M. Curreli, C.A. Olson, H.-I. Liao, R. Sun, R.W. Roberts, R.J. Cote, M.E. Thompson, C. Zhou, *ACS Nano* **2010**, *4*, 6914.

[25] Z. Zhang, L. Zhang, S. Senz, M. Knez, *Chemical Vapor Deposition* **2011**, *17*, 149.

[26] R. Palgrave, I. Parkin, *Gold Bulletin* **2008**, 0.

[27] A.K.A. Aliganga, F. Xu, W. Knoll, S. Mittler, in *Proceedings of SPIE*, SPIE**2005**, 59690H.

[28] R.G. Palgrave, I.P. Parkin, *Journal of the American Chemical Society* **2006**, *128*, 1587.

[29] R.G. Palgrave, I.P. Parkin, *Chemistry of Materials* **2007**, *19*, 4639.

[30] D. Barreca, A. Gasparotto, C. Maccato, E. Tondello, *Nanotechnology* **2008**, *19*, 255602.

[31] R. Binions, C. Piccirillo, R.G. Palgrave, I.P. Parkin, *Chemical Vapor Deposition* **2008**, *14*, 33.

[32] M.E. a. Warwick, C.W. Dunnill, R. Binions, *Chemical Vapor Deposition* **2010**, *16*, 220.

[33] J. Käshammer, P. Wohlfart, J. Weiß, C. Winter, *Optical Materials* **1998**, *9*, 406.

[34] P. Wohlfart, J. Weiβ, C. Winter, *Thin Solid Films* **1999**, *340*, 274.

[35] R. Fischer, U. Weckenmann, *Journal de Physique. IV* **2001**, *11*, 1183.

[36] M. Zinke-Allmang, *Thin Solid Films* **1999**, *346*, 1.

[37] C. Winter, U. Weckenmann, R.A. Fischer, * J. Käshammer, V. Scheumann, S. Mittler, *Chemical Vapor Deposition* **2000**, *6*, 199.

[38] A. Rezaee, K.K.H. Wong, T. Manifar, S. Mittler, *Surface and Interface Analysis* **2009**, *41*, 615.

[39] A.K.A. Aliganga, I. Lieberwirth, G. Glasser, A.-S. Duwez, Y. Sun, S. Mittler, *Organic Electronics* **2007**, *8*, 161.

[40] D. Trovo, E. Ertorer, R. Huang, T. Cheng, C. Rangan, S. Mittler, in *Modern Aspects of Electrochemistry*, **2013**, 104.

[41] A. Ulman, *Chemical Reviews* **1996**, *96*, 1533.

[42] F. Schreiber, *Progress in Surface Science* **2000**, *65*, 151.

[43] D. Schwartz, *Annual Review of Physical Chemistry* **2001**, 107.

[44] J.C. Love, L. a Estroff, J.K. Kriebel, R.G. Nuzzo, G.M. Whitesides, *Self-assembled Monolayers of Thiolates on Metals as a Form of Nanotechnology.*, **2005**.

[45] P.M. Tiwari, K. Vig, V. a. Dennis, S.R. Singh, *Nanomaterials* **2011**, *1*, 31.

[46] H. Li, J. Zhang, X. Zhou, G. Lu, Z. Yin, G. Li, T. Wu, F. Boey, S.S. Venkatraman, H. Zhang, *Langmuir : the ACS Journal of Surfaces and Colloids* **2010**, *26*, 5603.

[47] C.-S. Chiu, H.-M. Lee, C.-T. Kuo, S. Gwo, *Applied Physics Letters* **2008**, *93*, 163106.

[48] J. Yang, T. Ichii, K. Murase, H. Sugimura, *Langmuir : the ACS Journal of Surfaces and Colloids* **2012**, *28*, 7579.

[49] M.J. Madou, *Fundamentals of Microfabrication: The Science of Miniaturization*, CRC Press**2002**.

[50] J. Dostálek, C.J. Huang, W. Knoll, in *Surface Design: Applications in Bioscience and Nanotechnology*, Wiley-VCH Verlag GmbH & Co. KGaA**2009**, 29.

[51] C. Corti, R. Holliday, *Gold: Science and Applications*, Taylor & Francis**2010**.

[52] C. Gatti, P. Macchi, *Modern Charge-Density Analysis*, Springer**2012**.

[53] A.O. Borissova, A.A. Korlyukov, M.Y. Antipin, K.A. Lyssenko, *The Journal of Physical Chemistry A* **2008**, *112*, 11519.

[54] M. Gudiksen, *JOURNAL-AMERICAN* **2000**, 8801.

[55] S. Zou, G. Schatz, in *Surface-Enhanced Raman Scattering* (Eds: K. Kneipp, M. Moskovits, H. Kneipp), Springer Berlin / Heidelberg**2006**, 67.

[56] F. Toderas, M. Baia, L. Baia, S. Astilean, *Nanotechnology* **2007**, *18*, 255702.

[57] M. Fan, G.F.S. Andrade, A.G. Brolo, *Analytica Chimica Acta* **2011**, *693*, 7.

[58] N. Strekal, S. Maskevich, *Reviews in Plasmonics 2010* **2012**, *2010*, 283.

[59] G. Moula, R. Rodriguez-Oliveros, P. Albella, J. a. Sanchez-Gil, R.F. Aroca, *Annalen Der Physik* **2012**, *524*, 697.

[60] H. Jiang, T. Li, E. Ertorer, J. Yang, J. Sabarinathan, S. Mittler, *Sensors and Actuators A: Physical* **2013**, *189*, 474.

[61] L. Zhao, D. Jiang, Y. Cai, X. Ji, R. Xie, W. Yang, *Nanoscale* **2012**, *4*, 5071.

[62] P. Rooney, A. Rezaee, S. Xu, T. Manifar, A. Hassanzadeh, G. Podoprygorina, V. Böhmer, C. Rangan, S. Mittler, *Physical Review B* **2008**, *77*, 1.

[63] G.J. Nusz, S.M. Marinakos, A.C. Curry, A. Dahlin, F. Höök, A. Wax, A. Chilkoti, *Analytical Chemistry* **2008**, *80*, 984.

[64] M. Fan, M. Thompson, M. Andrade, *Analytical Chemistry* **2010**, *82*, 6350.

[65] A. Rezaee, A. Aliganga, *The Journal of Physical* **2009**, *113*, 15824.

[66] A. Rezaee, L.C. Pavelka, S. Mittler, *Nanoscale Research Letters* **2009**, *4*, 1319.

[67] A. Rezaee, A.K. a Aliganga, L.C. Pavelka, S. Mittler, *Physical Chemistry Chemical Physics : PCCP* **2010**, *12*, 4104.

[68] H. Schmidbaur, A. Shiotani, *Chemische Berichte* **1971**, *104*, 2821.

[69] RASBAND W. S., *Http://rsbweb.nih.gov/ij/* **2008**.

Chapter 5

Antibody Fragment Functionalized Gold Nanoparticles for Epidermal Growth Factor Receptor Detection[4]

5.1   Introduction

Gold nanoparticles (AuNPs) exhibit extraordinary spectroscopic properties, which make them ideal for designing highly sensitive AuNP based biosensors.[1] Localized surface plasmon resonance (LSPR) is the main phenomenon behind the spectroscopic properties of AuNPs. An increase in the refractive index around the vicinity of the surface of AuNPs yields a color change.[2], [3] For biosensor applications, the surface of the AuNPs is modified to recognize only a specific biomolecule. When the biomolecule is bound to the recognition site, the color change is precisely detected by a UV-Vis absorption spectrometer. [4], [5]

---

[4] A version of this chapter is in preparation for publication. Erden Ertorer, Shell Ip, Rasoul Soleimani, Hao Jiang, Gilbert Walker, Silvia Mittler., "Antibody Fragment Functionalized Gold Nanoparticles for Epidermal Growth Factor Receptor Detection".

In order to detect a certain protein, antibodies to this protein are immobilized on the gold surface. [6]–[9] One way to do this is using the well-known affinity of streptavidin to biotin. Biotin is a well-studied small molecule that can easily be attached to any protein by a reaction known as biotinylation. Streptavidin is a large protein with four high-affinity binding sites to biotin. [5], [10]–[12] Once biotin is immobilized on a gold surface, streptavidin attaches to the biotin, and the remaining binding sites of the streptavidin are used for binding biotinylated antibodies. When the matching antigen is introduced, it selectively binds to its antibody and changes the plasmon resonance frequency, which can be observed as a red shift in the absorption curve maximum of the sample. [1], [13], [14] The amount of the shift is correlated with the concentration of the target analyte.

Above mentioned the layer-by-layer approach has a disadvantage; since the evanescent field around the plasmonic nanoparticles decreases exponentially, the signal of the LSPR sensor also diminishes with increasing distance of the recognition reaction from the surface. [14], [15] Therefore, each additional component between the surface and the recognition site adversely affects the sensitivity.

An antibody is a large Y-shaped protein (Figure 5.1a). The base of the Y, called Fc (fragment crystallizable), is responsible for modulating immune cell activity. The arms of the Y, the so-called F(ab')2 (fragment antigen binding), have two binding sites to the specific antigen. Dithiol bonds at the hinge region keep those two arms together. For sensing applications, since recognition happens at the F(ab')2 region, removing the bulky chemistry between the surface and recognition reaction is possible by cutting the F(ab')2 region of the antibody, reducing it to F(ab'), and directly immobilizing only the binding

sites to the surface. This approach can potentially increase sensitivity. There are some studies that report using F(ab') fragments for sensing purposes in electrochemical or localized plasmon resonance based setups. [7], [9], [16]–[19]

We recently developed an easy and inexpensive method to fabricate highly stable AuNPs via organometallic chemical vapor deposition (OMCVD) onto planar substrates and demonstrated their protein sensing capabilities. [20]

The epidermal growth factor receptor (EGFR) is a cancer surface marker protein; its overexpression is relevant to lung and colorectal cancer. [21] In this study, we are investigating the LSPR sensing feasibility of OMCVD-grown gold nanoparticles for EGFR detection with anti-EGFR Fab fragments by directly immobilizing them on the gold surface and comparing the LSPR shift with layer-by-layer immobilization in a similar sensing setup. [14]

5.2 Experimental

5.2.1 Fabricating gold samples

The process of fabricating immobilized AuNPs has been described in one of our recent studies. [20] In short; BK7 glass slides (8 x 12 mm) were cleaned with Nano-Strip solution (Cyantek Inc., CA, USA) to remove possible organic contamination. After rinsing with deionized water and drying, the slides were placed in an STS Reactive Ion Etch system (STS Surface Technology Systems, Newport, UK) to oxidize the surfaces, then silanization followed with HMDS in a YES-3TA HDMS vacuum oven (Yield Engineering, CA, USA). Substrates were placed in an OMCVD reactor for 18 minutes at 65°C and a vacuum of 0.05 mbar with a small watch glass containing 20 mg of the

organometallic gold precursor trimethylphosphinegoldmethyl ([(CH$_3$)$_3$P]AuCH$_3$). Then substrates were rinsed with pure ethanol to remove physisorbed AuNPs.

5.2.2 Preparing antibody fragments for self-assembly

EGFR antigen, antibody and control antibody fragments were purchased from Abcam (Abcam Inc., Toronto, Canada). EGFR F(ab')2 fragments were generated using Genovis FabRICATOR protease (Genevis, Lund, Sweden) in two steps, first cutting the antibodies at the hinge region and then purifying the F(ab')2 by removing the Fc fragments from the solution.

To functionalize the gold surface with active F(ab'), the disulfide bonds within the hinge region of the antibody, which holds the two F(ab') fragments together, must be partially reduced to expose the free -SH groups that will bond with gold. This is achieved by reducing the F(ab')2 molecules using mild reducing agents. Under mild conditions, the disulfide bonds at the base of the F(ab')2 are reduced while the disulfide bonds holding the heavy and light chains of the F(ab') are still intact. [16], [22] Overreduction will separate the heavy and light chains and render the antibody fragments useless. The optimal conditions were determined by systematic variation of the 2-mercaptoethylamine concentration and monitoring F(ab') formation via sodium dodecyl sulfate polyacrylamide gel electrophoresis. Reduction with 10 mM 2-mercaptoethylamine for 30 min at 37°C was found to be optimal.
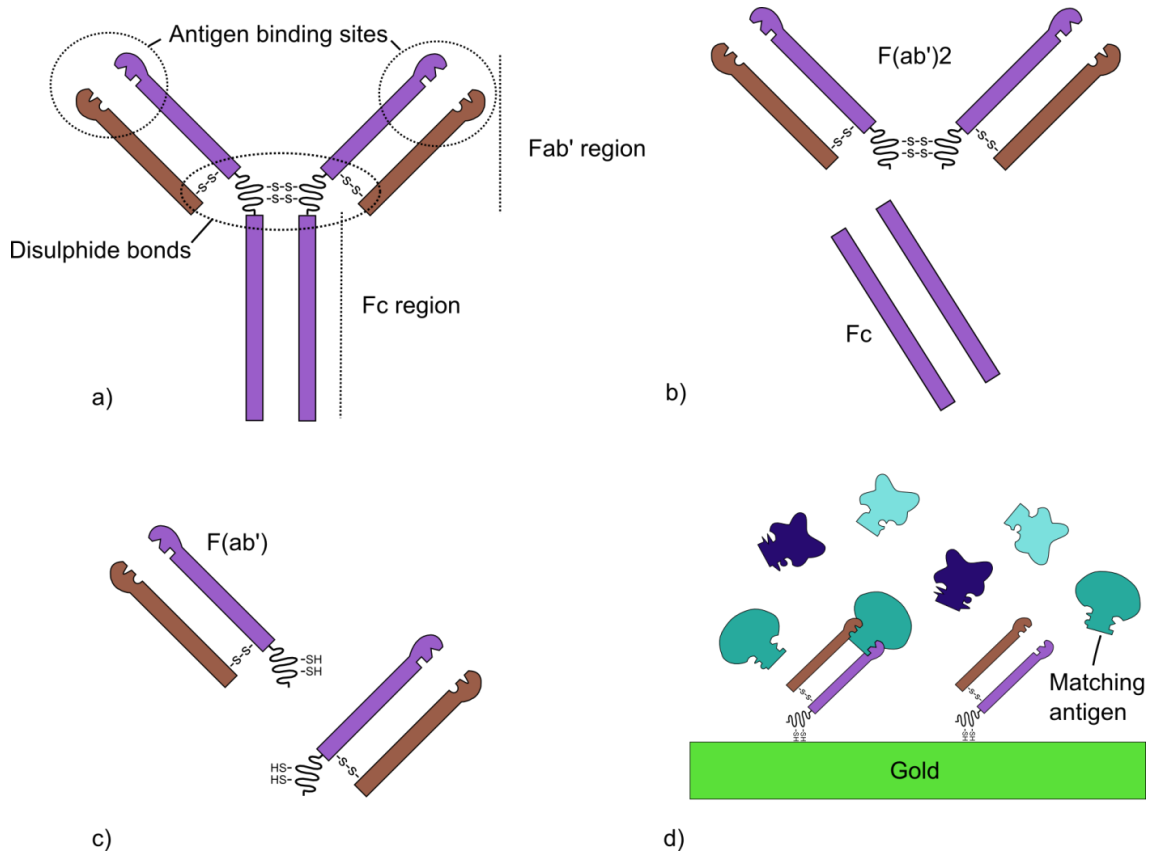
Figure 5.1. Illustration of antibody fragment preparation and selective recognition on gold surface. a) structure of an antibody, b) digestion to remove the Fc region from the F(ab')2 fragment, c) F(ab') is obtained by reducing F(ab')2

5.2.3 Sensing

Absorption spectra of the samples for bulk refractive index sensing experiments were measured by a Lambda 850 UV-Vis Spectrometer (Perkin Elmer Inc., Massachusetts, USA) while the samples were immersed in ethanol, methanol, isopropanol and dichloromethane. Refractive indices of the solvents were obtained by a Zeiss refractometer (Carl Zeiss AG, Oberkochen, Germany).

For protein sensing, samples were left in a solution of 3 μg/ml antibody fragment and PBS buffer for two hours. The required amount of surface coverage was calculated by a

method adapted from Vikholm-Ludin's work. [23] In order to test nonspecific binding, other sets of samples were immersed in a solution of control antibody fragments for the same duration. They were repeatedly rinsed with PBS buffer in order to remove unattached antibody fragments.

Anti-EGFR-F(ab') fragment-functionalized samples were immersed in PBS buffer for baseline absorption measurements. Then, EGFR antigen was introduced in cuvettes at a final concentration of 200 ng/ml. After letting them bind for 5 minutes, their absorption spectra were measured five times for each sample. For concentration response experiments, the sample was first exposed to PBS buffer and the concentrations= of antibody exponentially increased from 1 ng/ml to 1000 ng/ml. Absorption spectra were measured by a Varian Cary 5000 UV-Vis-NIR spectrometer (Varian Inc., California, USA).

5.3   Results and discussion

5.3.1 Bulk refractive index sensing

Plasmon frequency is a function of the refractive index of the surrounding medium of the gold nanoparticles. An increasing refractive index of a solvent appears as a linear red shift in the absorption spectrum of the sample. Bulk refractive index sensing studies are useful to give a rough idea about the sensing capabilities of the sensor and the signal-to-noise ratio. Figure 5.2 is an example of a bulk refractive index sensing chart for a 15 minute OMCVD deposition time sample. The figure of merit, which is the slope of the trend line, was calculated as ~88 nm/RIU.
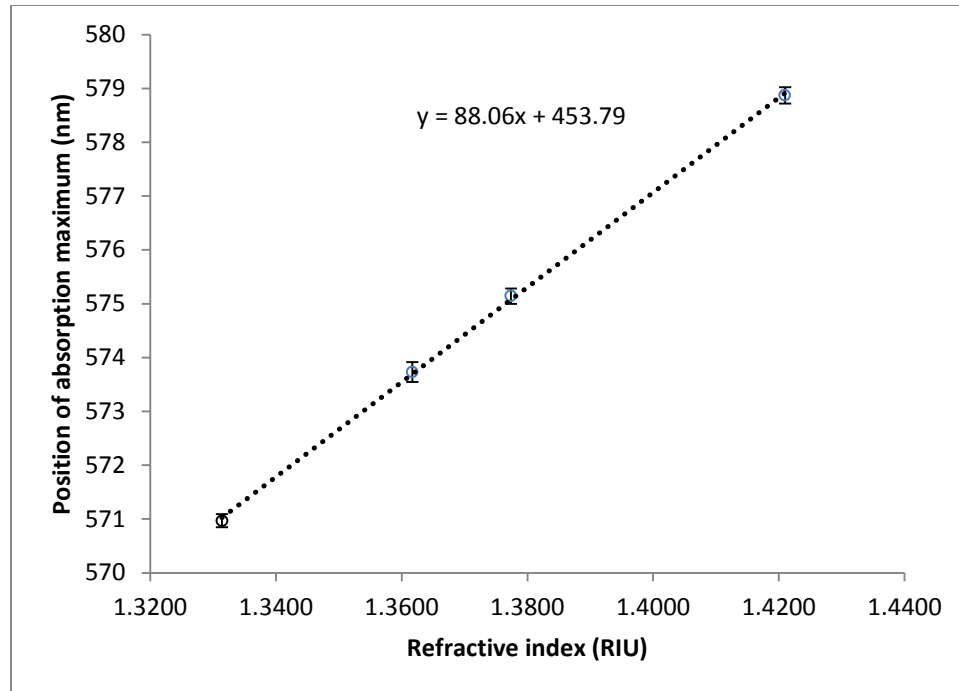
Figure 5.2. Bulk sensitivity curve of 15 minute OMCVD deposition time sample

5.3.2 Protein sensing

In the first test of binding between the anti-EGFR-F(ab') fragment-functionalized surface

and the nonspecific F(ab') control, we found that at an EGFR antigen concentration of

~200 ng/ml, the anti-EGFR-F(ab')-functionalized surface demonstrated an ~2 nm LSPR

red shift compared to straight PBS, while the negative control, functionalized with a

nonspecific F(ab'), had no detectable shift (Figure 5.3). This indicates that the EGFR

antibody bound to the positively labeled surface and did not bind to the negative control

surfaces, as expected. Instead of using layer-by-layer linking chemistry for similar

antibody-antigen coupling as in our earlier study [14], functionalization of the gold

nanoparticles with antibody fragment carried the recognition reaction closer to the

surface and yielded an increased sensor signal, which could increase the sensitivity and limit of detection.
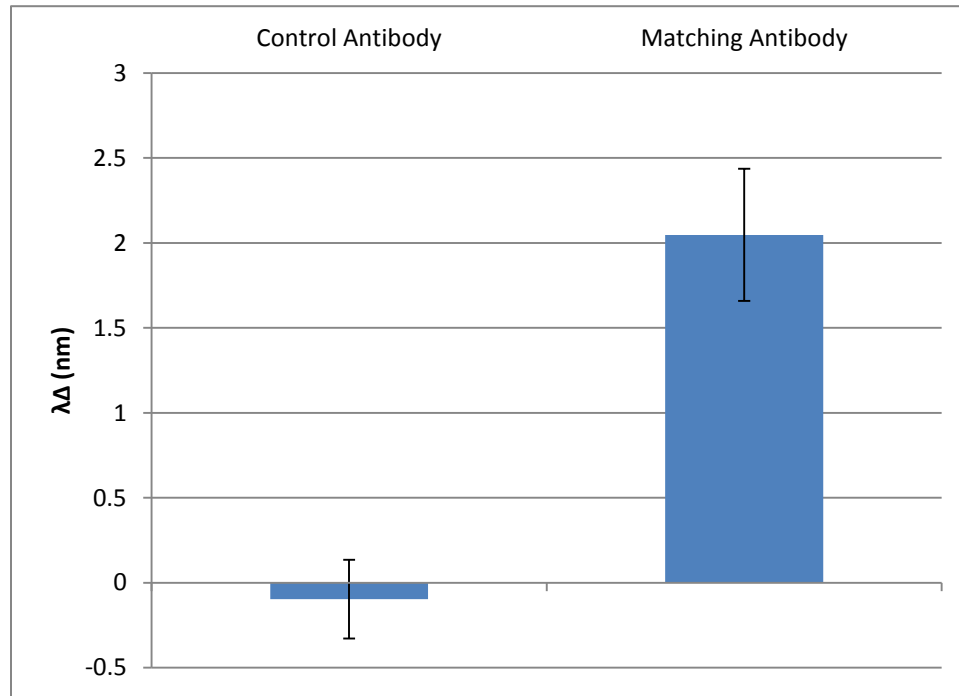
Figure 5.3. Shift in the absorption maximum for 200 ng/ml EGFR antigen

In concentration response studies, although there was an increasing trend, the maximum shift of ~2 nm was not reached at 200 ng/ml of antigen; only a 0.7 nm shift was observed for 1 µg/ml of antigen (Figure 5.4). In addition to this unexpectedly low response, the noise level was much higher than in the single-concentration experiment. Changing concentrations did introduce visible air bubbles to the solution, which could be an indication of nanobubble formation on the sample surface. [24] Degassing the solutions before using them could reduce bubble formation. The low sensor response could also be due to improper functionalization of the gold surface with antibody fragments, which

could also affect the reproducibility between experiments. Longer functionalization times with higher antibody fragment concentrations might be more effective.
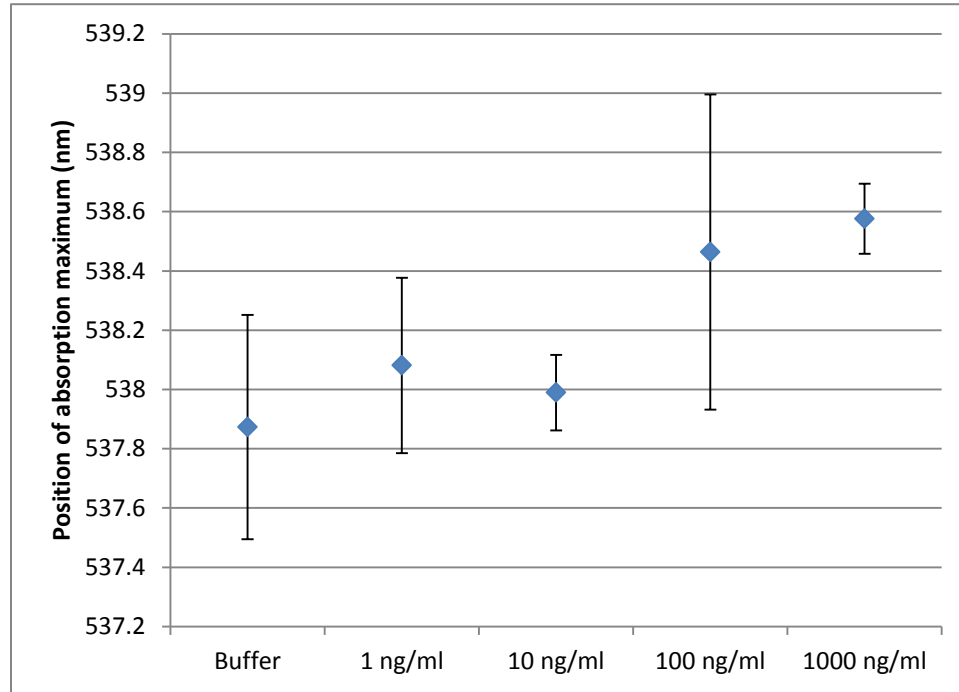
Figure 5.4. EGFR concentration response curve

For more realistic evaluation of sensor performance, experiments can be conducted in serum, which contains a variety of proteins that could bind nonspecifically. On the other hand, in order to prevent nonspecific binding, bovine serum albumin can be employed to protect the nonfunctionalized gold surface from protein binding. [22], [25] Further optimization might be possible using a short-chain OH-terminated thiol as a dilutant to eliminate steric hindrance on the surface [26] and also by employing AuNPs with different sizes and interparticle spacing to obtain a higher sensor signal. [20]

5.4   Conclusion

We used OMCVD-grown gold nanoparticles for EGFR antigen sensing with surface immobilized antibody fragments. At 200 ng/ml of antibody, we obtained ~2 nm LSPR shift, which was approximately four times higher than the similar recognition reaction reported in our previous study [14]. This indicates that having the recognition reaction closer to the gold surface increases the signal and potentially improves the sensitivity and limit of detection. Further experiments should be conducted to investigate the reason for the high error and poor sensitivity of the concentration response and to obtain the usual sigmoidal sensor response.

Acknowledgements

References

[1]   E. E. Bedford, J. Spadavecchia, C.-M. Pradier, and F. X. Gu, "Surface plasmon resonance biosensors incorporating gold nanoparticles.," *Macromol. Biosci.*, vol. 12, no. 6, pp. 724–39, Jun. 2012.

[2]   E. Hutter and J. H. Fendler, "Exploitation of Localized Surface Plasmon Resonance," *Adv. Mater.*, vol. 16, no. 19, pp. 1685–1706, Oct. 2004.

[3]   A. Lopatynskyi, O. Lopatynska, and V. Chegel, "Comparative analysis of response modes for gold nanoparticle biosensor based on localized surface plasmon resonance," *… , Quantum Electron. …*, pp. 114–121, 2011.

[4]   S. Underwood, "Effect of the solution refractive index on the color of gold colloids," *Langmuir*, vol. 10, no. 10, pp. 3427–3430, Oct. 1994.

[5]   S. M. Marinakos, S. Chen, and A. Chilkoti, "Plasmonic detection of a model analyte in serum by a gold nanorod sensor.," *Anal. Chem.*, vol. 79, no. 14, pp. 5278–5283, Jul. 2007.

[6]   K. Drouvalakis, S. Bangsaruntip, W. Hueber, L. G. Kozar, P. J. Utz, and H. Dai, "Peptide-coated nanotube-based biosensor for the detection of disease-specific autoantibodies in human serum.," *Biosens. Bioelectron.*, vol. 23, no. 10, pp. 1413–21, May 2008.

[7]   R. G. Rayavarapu, W. Petersen, C. Ungureanu, J. N. Post, T. G. van Leeuwen, and S. Manohar, "Synthesis and bioconjugation of gold nanoparticles as potential molecular probes for light-based imaging techniques.," *Int. J. Biomed. Imaging*, vol. 2007, p. 29817, Jan. 2007.

[8]   M.-C. Daniel and D. Astruc, "Gold nanoparticles: assembly, supramolecular chemistry, quantum-size-related properties, and applications toward biology, catalysis, and nanotechnology.," *Chem. Rev.*, vol. 104, no. 1, pp. 293–346, Jan. 2004.

[9]   P. M. Tiwari, K. Vig, V. a. Dennis, and S. R. Singh, "Functionalized Gold
        Nanoparticles and Their Biomedical Applications," *Nanomaterials*, vol. 1, no. 1,
        pp. 31–63, Jun. 2011.

[10]   G. J. Nusz, S. M. Marinakos, A. C. Curry, A. Dahlin, F. Höök, A. Wax, and A.
        Chilkoti, "Label-free plasmonic detection of biomolecular binding by a single gold
        nanorod.," *Anal. Chem.*, vol. 80, no. 4, pp. 984–9, Feb. 2008.

[11]   M. Seifert, M. T. Rinke, and H.-J. Galla, "Characterization of streptavidin binding
        to biotinylated, binary self-assembled thiol monolayers--influence of component
        ratio and solvent.," *Langmuir*, vol. 26, no. 9, pp. 6386–93, May 2010.

[12]   J. W. Menezes, J. Ferreira, M. J. L. Santos, L. Cescato, A. G. Brolo, P.
        Photovoltaics, and B. J. W. Menezes, "Large-Area Fabrication of Periodic Arrays
        of Nanoholes in Metal Films and Their Application in Biosensing and Plasmonic-
        Enhanced Photovoltaics," *Adv. Funct. Mater.*, vol. 20, no. 22, pp. 3918–3924,
        Nov. 2010.

[13]   S. H. Choi, J. W. Lee, and S. J. Sim, "Enhanced performance of a surface plasmon
        resonance immunosensor for detecting Ab-GAD antibody based on the modified
        self-assembled monolayers.," *Biosens. Bioelectron.*, vol. 21, no. 2, pp. 378–83,
        Aug. 2005.

[14]   H. Jiang, T. Li, E. Ertorer, J. Yang, J. Sabarinathan, and S. Mittler, "A biosensor
        based on periodic arrays of gold nanodisks under normal transmission," *Sensors
        Actuators A Phys.*, vol. 189, no. 0, pp. 474–480, Jan. 2013.

[15]   D. Schwartz, "Mechanisms and kinetics of self-assembled monolayer formation,"
        Annu. Rev. Phys. Chem., no. 52, pp. 107–137, 2001.

[16]   J. C. O'Brien, V. W. Jones, M. D. Porter, C. L. Mosher, and E. Henderson,
        "Immunosensing platforms using spontaneously adsorbed antibody fragments on
        gold.," *Anal. Chem.*, vol. 72, no. 4, pp. 703–10, Feb. 2000.

[17] J. P. Kim, B. Y. Lee, J. Lee, S. Hong, and S. J. Sim, "Enhancement of sensitivity and specificity by surface modification of carbon nanotubes in diagnosis of prostate cancer based on carbon nanotube field effect transistors.," *Biosens. Bioelectron.*, vol. 24, no. 11, pp. 3372–3378, Jul. 2009.

[18] S. K. Vashist, D. Zheng, K. Al-Rubeaan, J. H. T. Luong, and F.-S. Sheu, "Advances in carbon nanotube based electrochemical sensors for bioanalytical applications.," *Biotechnol. Adv.*, vol. 29, no. 2, pp. 169–88, 2011.

[19] E. Larsson, J. Alegret, M. Käll, and D. Sutherland, "Sensing characteristics of NIR localized surface plasmon resonances in gold nanorings for application as ultrasensitive biosensors," *Nano Lett.*, vol. 7, no. 5, pp. 1256–1263, May 2007.

[20] E. Ertorer, J. C. Avery, L. C. Pavelka, and S. Mittler, "Surface Immobilized Gold Nanoparticles by Organometallic Chemical Vapor Deposition on Amine Terminated Glass Surfaces," *Chem. Vap. Depos.*, 2013.

[21] R. . Nicholson, J. M. . Gee, and M. . Harper, "EGFR and cancer prognosis," *Eur. J. Cancer*, vol. 37, pp. 9–15, Sep. 2001.

[22] B. Y. Kim, C. B. Swearingen, J.-A. a Ho, E. V Romanova, P. W. Bohn, and J. V Sweedler, "Direct immobilization of Fab' in nanocapillaries for manipulating mass-limited samples.," *J. Am. Chem. Soc.*, vol. 129, no. 24, pp. 7620–6, Jun. 2007.

[23] I. Vikholm-Lundin, "Immunosensing based on site-directed immobilization of antibody fragments and polymers that reduce nonspecific binding.," *Langmuir*, vol. 21, no. 14, pp. 6473–7, Jul. 2005.

[24] M. Holmberg, A. Kühle, J. Garnæs, K. Mørch, and A. Boisen, "Nanobubble trouble on gold surfaces," *Langmuir*, vol. 19, no. 13, pp. 10510–10513, 2003.

[25] F. N. Ishikawa, M. Curreli, C. A. Olson, H.-I. Liao, R. Sun, R. W. Roberts, R. J. Cote, M. E. Thompson, and C. Zhou, "Importance of controlling nanotube density

for highly sensitive and reliable biosensors functional in physiological conditions.," *ACS Nano*, vol. 4, no. 11, pp. 6914–22, Nov. 2010.

[26] J. Spinke, M. Liley, F.-J. Schmitt, H.-J. Guder, L. Angermaier, and W. Knoll, "Molecular recognition at self-assembled monolayers: Optimization of surface functionalization," *J. Chem. Phys.*, vol. 99, no. 9, p. 7012, 1993.

Chapter 6

Conclusion and Future Directions

In this thesis, two inexpensive methods to create nanostructures on planar substrates are covered and their feasibility demonstrated with several applications. Laser interference lithography is used to create submicron size particles for both cell adhesion studies and plasmonic sensing applications. Structures are regularly distributed over the substrate surface. On the other hand organometallic chemical vapor deposition is employed for surface immobilized randomly distributed gold nanoparticle on the substrate surface. Their size and interparticle distance are order of ten nanometers. Beyond the demonstrating the sensing capabilities of the OMCVD grown gold nanoparticles, a new strategy of coupling chemistry is demonstrated to increase the performance of plasmonic sensor platforms. Two fabrication methods and their application examples and cost analyses are summarized in following items.

6.1   Overview of fabrication methods

6.1.1   Laser interference lithography

Laser interference lithography (LIL) is a simple and inexpensive method to create nanostructures. In the work presented in Chapter 2, laser interference lithography was used for creating nanostructures on substrate surfaces. Double exposure was used to create two-dimensional arrangements. Biaxial periodic structures were created by

changing the stage angle between the exposures. In addition to creating uniform structures over large areas, creating systematically changing patterns on the same substrate is described.

Having biaxial periodic and systematically changing structures on a substrate is important to allow various experiments with a single substrate, as demonstrated with cell adhesion and spreading studies with osteoblast cells. Osteoblasts responded differently to different patterns on the substrate. When there was no pattern, focal adhesions and general cell morphology were randomly oriented. When there was a groove or dot pattern, adhesion sites were formed on the tip of the substrates. Cell morphology also conformed to the orientation of the groove structures. For the dot pattern, cells were aligned randomly.

In another experiment, we controlled the migration of osteoclast cells with a 1200 nm periodicity groove pattern; the osteoclasts moved along the orientation of the groove.

These results are significant, since they increase our understanding of how cells become activated and respond to different surface morphologies. This knowledge also can be transferred to tissue engineering and implant technology to improve the healing process and increase implant success.

Within the geometrical and laser wavelength limitations of our LIL system, we created 600 nm, 900 nm and 1200 nm periodicities. Additional periodicities, surface functionalities, transition structures, and structure depths should be studied to investigate their effects on cell behavior.

An advance over studies reported in the literature is that having various structures and biaxial periodicities in the same substrate would be beneficial in employing more than one set of resonance conditions in a single experiment. Substrates also can be used in SERS applications. As discussed in detail in Chapter 2, low-cost plasmonic structures were created by LIL, and in Chapter 3 we employed LIL to fabricate gold nanodisks and discussed plasmonic sensing properties, by comparing experimental and numerical simulation results. Although uniformity of LIL-fabricated gold nanodisks was not as good as that resulting from electron beam lithography, this drawback can be neglected for any application which does not require excellent uniformity, such as transmission absorption sensors.

LIL is limited to periodic structures and the periodicity is directly proportional to the laser wavelength. In order to achieve smaller features, lower-wavelength UV or extreme UV lasers and compatible components should be employed, which may increase the cost.

6.1.2 Organometallic chemical vapor deposition for creating gold nanoparticles

Organometallic chemical vapor deposition (OMCVD) is a simple and inexpensive method to fabricate immobilized gold nanoparticles. In contrast to studies described in the literature, amine functionalization is used on the substrate surfaces. In Chapter 3, we describe how we optimized the OMCVD process to fabricate stable and reproducible surface-immobilized gold nanoparticles, and also some characterization and data-analyzing methods.

The effect of systematically increased time of OMCVD on the particle size, shape, interparticle spacing, and plasmonic behavior were studied in Chapter 4. Increasing

deposition time yielded larger and denser particles, as expected. On the other hand, uniformity of shape and size decreased and corners appeared at longer deposition times. As a result, a blue shift and widening of the absorption curve were observed. For closely spaced particles, an optical crosstalk shoulder appeared in the absorption curve.

The well-known biotin-streptavidin affinity was used to demonstrate the sensing ability of OMCVD-grown gold nanoparticles. The results suggested that despite their low cost and simplicity of production, as biosensors, OMCVD-grown gold nanoparticles performed similarly to other planar sensors based on localized surface plasmon resonance (LSPR), with further optimization possibilities.

In Chapter 5, OMCVD-grown gold nanoparticles were used to detect the epidermal growth factor receptor (EGFR). EGFR is a surface marker related to lung cancer and colorectal cancer. Using antibody fragments for sensing is a technique used in some electrochemical sensor applications and a few surface plasmon resonance-based sensing studies. The main advantage of this technique for LSPR-based sensing is carrying the recognition reaction close to the surface to increase the sensitivity. While the control experiments did not give any detectable response, we obtained an LSPR shift about four times higher than that observed in our former study, which used an LSPR-based sensor. This sensor used biotin-streptavidin affinity to immobilize the antibody in order to detect a similar-sized antigen. Removing the bulky chemistry between the gold surface and the target antigen yielded an increased signal. Further optimization can be achieved using several techniques mentioned in the chapter. On the other hand, concentration response studies, despite the increasing trend, did not give a clear response. We suspect that increasing the concentration caused bubble formation, decreasing the performance of the

sensor. However, as a result of improper surface functionalization, loosely attached antibody fragments may not resist liquid flow. More studies should be conducted to investigate and eliminate possible sources of the problem.

Sensing experiments can be carried out on a waveguide surface to exploit the benefit of different polarizations and improve the signal-to-noise ratio.

OMCVD-grown gold nanoparticles can also be used in solar cells, for nanotube or nanowire growth, for SERS studies, or wherever substrate immobilized gold nanoparticles are required at the size regime of ~15 nanometers.

Although the size distribution is narrow, especially for low deposition times, only randomly distributed particles can be obtained with OMCVD. In order to control size and interparticle distance distribution, other techniques should be employed such as diluting the amine groups on the surface with other functionalities. Different temperature and pressure combinations could be used to investigate their effects on size and interparticle distance distribution.

6.2 Efficiency and cost analysis

Although equipment and material costs vary among the institutions, that would be useful to make a rough cost and efficiency analysis. Since the most part of the research in this thesis was conducted in The University of Western Ontario, Canada, the cost discussion will be based on the prices in Canada and Western Nanofabrication Facility in Canadian Dollars. Western Nanofabrication Facility is a self-sustaining non-profit unit of The University of Western Ontario.

Laser interference lithography requires a laser with a highly stable optical power. The coherence length of the laser should be longer than the beam path. The laser we used in our setup (Omnichrome Series 74, Model 4074-P-A03, CVI Melles Griot, NM, USA) costs around C$10000. Focused ion beam system (LEO 1540XB FIB/SEM, Zeiss, Germany) in Western Nanofab costs around C$2.4M and Electron beam lithography system (LEO 1530 SEM Zeiss, Germany) costs around C$1.2M. In terms of equipment costs, LIL has a significant advantage, however, it should be noted that LIL does not have the advantage of fabricating arbitrary patterns at a wide range of size regimes as FIB and EBL have. Only periodic patterns can be fabricated and size regime is mainly determined by the wavelength of the laser as discussed in chapter 2. For the system we used the periodicity is limited by 600 nm to 1200 nm. FIB can reach the feature size of 1nm and depending on the photoresist, EBL can go down to 50nm.

FIB and EBL requires long processing times in compare with LIL. Mainly depending on size of the covered area, their processing time varies between hours and days. For large areas such as 1''x 1'' they are not feasible because of the time required and high operating costs. Coverage are of LIL is mainly limited by the expanded beam size and the mirror size. Exposure time is in order of minutes for S1805 (Shipley, MA, USA) photoresist.

Fabrication cost of a 1'' by 1'' BK7 sample with a pattern made of photoresist is less than C$30 with LIL, including the substrate, chemicals, and Western Nanofabrication Facility user fees. Due to the high operating costs of FIB and EBL sample cost is order of thousand dollars with a low surface coverage. It should be noted that the HeCD laser we used has a lifetime around 6000 hours. After the lifetime, power stability and coherence

reduces to decrease the quality of the samples. This was not considered while calculating the cost.

On the other hand OMCVD requires pretty standard chemistry lab tools and a simple vacuum reactor as illustrated in chapter 4. A batch of ten samples costs around C$50 including the precursor, other chemicals and Western Nanofabrication Facility user fees. Since the precursor is not chemically stable even in the cold storage conditions, its activity is decreases by time, which requires synthesizing the precursor frequently in small batches. In compare with FIB and EBL, OMCVD has cost and large surface coverage advantage. However the particles are randomly distributed over the surface.

Appendix A

Copyright permission for Chapter 2

Dear Erden,

Thank you for seeking permission from SPIE to reprint material from our publications. As author, SPIE shares the copyright with you, so you retain the right to reproduce your paper in part or in whole.

Publisher's permission is hereby granted under the following conditions:

(1) the material to be used has appeared in our publication without credit or acknowledgment to another source; and

(2) you credit the original SPIE publication. Include the authors' names, title of paper, volume title, SPIE volume number, and year of publication in your credit statement.

Sincerely,

Karen Thomas for
Eric Pepper, Director of Publications
SPIE
P.O. Box 10, Bellingham WA 98227-0010 USA
360/676-3290 (Pacific Time) xxx@spie.org

From: Erden Ertorer
Sent: Thursday, March 07, 2013 5:16 AM
To: reprint_permission
Subject: Reprint Permission

To Whom it May Concern,

I am writing to request permission to use following material in my doctoral dissertation.

Title: "Large Area Periodic, Systematically Changing, Multi-Shape Nanostructures by LaserInterferenceLithography and Cell Response to these Topographies"
Journal: Journal of Biomedical Optics

Authors: Erden Ertorer, Fartash Vasefi, Joel Keshwahe, Mohamadreza Najiminaini, Christopher Halfpap, Uwe Langbein, Jeffrey J.L. Carson, Douglas W. Hamilton and Silvia Mittler
Status: Accepted manuscript
Requested parts: Complete paper
Republishing in : PhD Thesis
Manuscript reference number: JBO 12646RR

Sincerely,
--
Erden Ertorer

PhD Candidate
Biomedical Engineering Program
Faculty of Engineering

The University of Western Ontario

Curriculum Vitae

Name: Erden Ertorer

Post-secondary Ankara University
Education and Ankara,Turkey
Degrees: 1996-2002 B.Sc.

        Gazi University
        Ankara, Turkey
        2003-2006 M.Sc.

        The University of Western Ontario
        London, Ontario, Canada
        2008-2013 Ph.D.

Honours and   Ontario Graduate Scholaship
Awards: 2011- 2012
        Ontario Graduate Scholaship in Science and Technology
        2009 - 2010
        Western Graduate Research Scholarship
        2008 - 2012
        CERN Technical Student Scholarship
        2005 - 2006
        TUBITAK International Research Scholarship
        2005 - 2006

Related Work   Research & Teaching Assistant
Experience   The University of Western Ontario
        2008-2012

Publications:

E. Ertorer, F. Vasefi, J. Keshwah, M. Najiminaini, C. Halfpap, U. Langbein, J.J.L. Carson, D.W. Hamilton, S. Mittler, *Journal of Biomedical Optics* **2013**, *18*, 35002.

H. Jiang, T. Li, **E. Ertorer**, J. Yang, J. Sabarinathan, S. Mittler, *Sensors and Actuators A: Physical* **2013**, *189*, 474.

D. Trovo, E. Ertorer, R. Huang, T. Cheng, C. Rangan, S. Mittler, in *Modern Aspects of Electrochemistry*, **2013**, 104.

K. Kordas, **E. Ertorer,** et al., The ATLAS Data Acquisition and Trigger: concept, design and status. Nuclear Physics B - Proceedings Supplements **2007**, 172: 178-182. (Master's work)